Università degli Studi di Firenze
Facoltà di Ingegneria

Dottorato in

Ingegneria Energetica e Tecnologie Industriali Innovative

Assessment of boundary conditions for heat transfer and aeroacoustic analysis

Relatori:

Prof. Bruno Facchini

Prof. Gavin Tabor

Candidato:

Cosimo Bianchini

Anno Accademico 2011

To my old dear Irenosky

When you steal from one author,

it's plagiarism;

if you steal from many,

it's research.

Wilson Mizner

Acknowledgements

A grateful thank to Prof. Bruno Facchini to have been placing faith in me and my research during these long years together.

My sincere gratitude goes to Prof. Gavin Tabor who gave me the opportunity to come out of my shell and temporary hosted me in Exeter.

I would also like to thank PhD. Antonio Andreini for always surprising me with the most wise suggestions, and PhD. Luca Mangani for the time spent together working, discussing, loosing our tempers and bearing each other.

A special regard for the "guests" of the office, the well known Ergon boys: Riccardo (for all the meshes he did for me), Mirko and Lorenzo (the owner);

I feel in debt also to all my present and past colleagues and friends, who shared a piece of this wonderful experience with me: Carlo, Francesco Francis, Alessio B. Torrita, Gianluca Giangi (for being the loudest), Inno, Alberto, Lorenzo i'Toni, Matteo Crazy Horse, Luca, Leonardo, Andrea, Giulio, Alessio P. and the two big teddy bears: Maio and Leo.

Abstract

The newly adopted Low-NOx lean premixed combustion technology, necessary to fulfil the increasingly stringent requirements in terms of pollutant emissions for aero-engines, made the design of effective combustor cooling systems even more challenging. A significant reduction of fresh air available for cooling purposes obliges designers to implement more and more efficient cooling devices. Moreover the large pressure fluctuations generated by the inhomogeneous combustion process require an optimal design of combustor cooling systems also as effective sound absorber, in order to reduce the effect of the instabilities on the chemical reactions and to avoid possible blow outs.

The accurate study of combustor cooling devices was hence approached numerically from both the heat transfer and the aeroacoustic point of view with an open-source CFD code. Effusion and impingement systems were considered for such an investigation. Addressing the analysis to the implementation of adequate boundary conditions to perform computations aligned with the state of the art.

An implicit solid/fluid interface for conjugate heat transfer analysis was developed also to treat non conformal coupling across the boundary. Applications to conventional and shaped multi-hole effusion plates with an highly slant angle of 17° were performed at typical blowing ratios for real aero-engines with a steady-state RANS approach.

Large Eddy Simulation of an axi-symmetric impingement jet at Re=23000 with heat transfer was conducted. The capabilities of two different auto-recycling techniques to generate turbulent inflow conditions for both velocity and temperature were tested comparing numerical data with a detailed database of experiments for mean velocity and fluctuations as well as the heat transfer level.

The acoustic behaviour of multiperforated plates, employed in both impingements and effusions hole arrays, was tested in bi-periodic configuration. Non reflecting inflow and outflow boundaries, known in the literature as Navier-Stokes Characteristic Boundary Conditions, were implemented to develop the necessary acoustic excitation and at the same time guarantee an adequate decrease of boundary generated perturbations.

The three implemented boundary conditions showed a good improvement of the results compared to standard boundary treatments permitting the achievement with an open-source code of results of equivalent accuracy compared to the most advanced research codes.

Contents

List of Figures

List of Tables

Nomenclature

Symbols

a	Spatial mode time coefficient matrix	$[-]$
A	Surface area,	$[m^2]$
	Absorption coefficient,	$[-]$
	Strength of velocity initial perturbation	$[m/s]$
b	Spatial mode inverse time coefficient matrix	$[-]$
BR	Blowing Ratio	$[-]$
c	Speed of sound	$[m/s]$
C	Advective velocity,	$[m/s]$
	Vortex strength,	$[-]$
	Correlation matrix	$[-]$
Co	Courant number	$[-]$
c_c	Cosine expansion coefficient	$[Pa]$
c_p	Specific heat at constant pressure	$[J/(kgK)]$
c_s	Sine expansion coefficient	$[Pa]$
D	Hole diameter,	$[m]$
	Diffusive terms for NSCBC	$[-]$
d_i	Normal propagating terms for NSCBC	$[-]$
E	Specific total energy	$[J/kg]$

f	Frequency	$[Hz]$
L	Characteristic length	$[m]$
h	Thickness,	$[m]$
	Heat transfer coefficient	$[W/(m^2K)]$
H	Height	$[m]$
i,j	Imaginary number	$[-]$
i,j,k	Generic counters	$[-]$
k	Turbulence kinetic energy,	$[m^2/s^2]$
	Thermal conductivity	$[W/(mK)]$
K	Relaxation coefficient for advective BC	$[1/s]$
Ma	Mach number	$[-]$
$\mathcal{M}$	Characteristic Mach number	$[-]$
n	Normal direction	$[-]$
Nu	Nusselt number hL/k	$[-]$
p	Static pressure	$[Pa]$
q_i	Instantaneous solution at snapshot i	$[-]$
R	Reflection coefficient,	$[-]$
	Perfect gas constant	$[J/(kgK)]$
r	Radial coordinate	$[m]$
Re	Reynolds number	$[-]$
s	Specific entropy	$[J/(kgK)]$
S	Scaling factor,	$[-]$
	Surface	$[m^2]$
S_x	Streamwise pitch	$[mm]$
S_y	Tangential pitch	$[mm]$
S	Strain rate	$[1/s]$
St	Strouhal number	$[-]$

t	Time	$[s]$
T	Static temperature,	$[K]$
	Transverse terms for NSCBC,	$[-]$
	Sampling period	$[s]$
T_0	Observation window	$[s]$
u_i	Generic velocity component	$[m/s]$
u	X axis velocity component	$[m/s]$
U	Velocity	$[m/s]$
V	Cell volume	$[m^3]$
v	Y axis velocity component	$[m/s]$
w	Coupling weight	$[-]$
x, y, z	Cartesian coordinates	$[m]$
y^+	Dimensionless wall distance	$[-]$
Z	Acoustic impedance	$[kg/(m^2 s)]$

Greek symbols

α	Hole angle,	$[°]$
	Overlapping area weight	$[-]$
β	Stiffness of velocity initial perturbation,	$[-]$
	LRM relaxation coefficient	$[-]$
Γ	Wave propagation constant	$[1/m]$
γ	Specific heat ratio	$[-]$
Δ	Filter width	$[m]$
δ	Attenuation constant	$[-]$
ε	Turbulence kinetic energy dissipation rate	$[m^2/s^3]$
η	Kolmogorov length scale,	$[m]$
	LRM coefficient	$[-]$

η_{ov}	Overall effectiveness	$[-]$
θ	Tangential coordinate	$[-]$
λ_i	Characteristic velocities	$[m/s]$
σ	Relaxation coefficient for NSCBC,	$[-]$
	Porosity	$[-]$
κ	Wave number	$[1/m]$
	Von Karman constant	$[-]$
μ	Dynamic viscosity	$[kg/(ms)]$
μ_T	Eddy viscosity	$[kg/(ms)]$
μ_{SGS}	Subgrid scale eddy viscosity	$[kg/(ms)]$
ν	Kinematic viscosity	$[m^2/s]$
ν_t	Turbulent kinematic viscosity	$[m^2/s]$
ρ	Density	$[kg/m^3]$
τ	Shear stress	$[N/m^2]$
ϕ	Convective fluxes,	$[kg/s]$
	Orthonormal basis function	$[-]$
Φ	Amplitude of pressure oscillation	$[Pa]$
φ	Phase of pressure oscillation	$[°]$
ψ	Generic transported scalar,	$[-]$
	Stream function	$[1/s]$
$\widetilde{\psi}$	Reference flow property	$[-]$
$\overline{\psi}$	Averaged flow property	$[-]$
ω	Angular frequency	$[rad/s]$

Subscripts

0	Equilibrium or reference state	
b	Bulk	

e	Entrance,
	Edge centroid
f	Generic face
g	Ghost cell
h	Hydraulic
i, j, k	Generic component of a vector (tensor)
j	Jet
n	Generic neighbour
p	Generic cell,
	Relative to pressure
ref	Reference value
t	Tangential directions
T	Relative to temperature
$u1$	Relative to normal velocity
$u2, u3$	Relative to tangential velocity
w	Wall
x	x axis
y	y axis
z	z axis
∞	Far field

Superscripts

$+$	Wall units,
	Wave propagating in the x-positive direction
$-$	Wave propagating in the x-negative direction
$'$	Fluctuating value

Miscellaneous

Δy	First node wall distance
$\mathcal{D}$	Least square distance
$\widetilde{D^i}$	Vector of viscous and conductive terms
$\widetilde{F^i}$	Flux vector of conservative variables along i^{th} direction
F^i	Jacobian matrix of the ith direction
$\mathcal{L}_i$	Amplitude variations of the ith characteristic wave
$\mathscr{R}$	Acoustic resistance
$\widetilde{U}$	Vector of conservative variables
$\mathscr{X}$	Acoustic reactance
$\|(\bullet)\|$	Euclidean norm of a vector
$\|(\bullet)\|$	Modulus of a real or complex number
$(\bullet)^*$	Complex conjugation
$(\bullet)^H$	Hermitian transpose
$(\bullet)^T$	Transpose matrix
$(\bullet)^\dagger$	Pseudoinverse
$\overline{(\bullet)}$	Time averaging
$\tilde{(\bullet)}$	Perturbation

Acronyms

ATL	Anisotropic Two Layer turbulence model
BC	Boundary Condition
CAA	Computational Aero-Acoustic
CFD	Computational Fluid Dynamics
DNS	Direct Numerical Simulation
$ECBC$	Euler Characteristic Boundary Conditions

FEM	Finite Element Method
FVM	Finite Volume Method
GPL	General Public Licence
LES	Large Eddy Simulation
$LODI$	Local One Dimensional Inviscid
LRM	Linear Relaxation Method
MPI	Message Passing Interface
$NSCBC$	Navier-Stokes Characteristic Boundary Conditions
$NSCE$	Navier-Stokes Characteristic Equations
$PISO$	Pressure Implicit with Splitting of Operators
PML	Perfectly Matched Layer
POD	Proper Orthogonal Decomposition
$RANS$	Reynolds Averaged Navier Stokes
SGS	Sub-Grid Scale
$SIMPLE$	Semi-IMplicit Pressure Linked Equations
TL	Isotropic Two Layer turbulence model

Introduction

Motivation

The always stricter constraints concerning pollutant emissions in aeroengines are pushing major manufacturers towards the design of innovative combustion technologies such as lean premixed flame combustors. With more and more air needed to feed the reactive process, cooling devices need to enhance their performance in order to maintain the desired efficiency also at lower coolant flow rates. The development of micro drilling at a slant angle with bias coolant flow, also known as effusion cooling, and aimed at obtaining almost full coverage protection and increasing the heat removal within the holes, has been successfully proposed as one of the most effective cooling techniques for the combustor liner. For the combustor dome instead, where the heat load is higher and the use of film protections may alter the combustion process due to the proximity of the heat shield and the flame itself, arrays of impinging jets are usually employed.

Both these devices utilize perforated plates whose properties as effective acoustic dampers drove designers to consider the beneficial effect of such systems on combustion instabilities damping as a second optimization parameter together with cooling effectiveness. The onset of pressure fluctuations due to thermo-acoustic instabilities in fact strongly limits engine design both in

terms of safety and stability issues.

The accurate analysis of these systems is hence fundamental both to understand the physical principles of their functioning, to identify engineering relevant parameters and to help develop reliable design rules. For these purposes, employing reliable and efficient three dimensional computational techniques may offer several advantages compared to experiments such as cost reduction, investigation of conditions which are difficult to reproduce and complete knowledge of the associated flow and thermal field.

Context and significance of the present research

The use of CFD for such kind of predictions however is not free of faults and standard RANS approach have already shown its limitations in reproducing the complex flow fields developing within gas turbine secondary air system. In past years in fact both commercial and open-source codes were employed for steady-state simulations of realistic and engineering relevant configurations with partial successes [29, 30].

This thesis is intended as a first attempt to overcome the failures of such an approach to explore and complete the capability of open-source CFD codes to perform advanced simulations of the heat transfer and aeroacoustic of modern aero-engines combustor cooling systems. Efforts were first posed on including the effects of metal wall temperature on the heat transfer distribution, secondly on avoiding strong modelling for turbulence effects embracing the principles of Large Eddy Simulation and finally to resolved externally excited unsteady phenomena.

All these kinds of computations, involving multi-domain and/or specific time dependent phenomena, require advanced boundary treatment to suit-

ably confine the computational domain whilst still permitting the onset of the desired flow characteristics. The need to solve for further unknowns such as turbulent fluctuations at the various temporal scales or the solid surface behaviour in fact introduces the necessity of a higher level of information provided on the boundary. Moreover inadequate boundary conditions may lead to errors in flow characteristic reproduction e.g. turbulent transition inhibition or fast turbulence decay. Even though the success of such computations strongly rely on the provision of adequate boundary conditions, a best practice to assign them has not been developed yet in the turbomachinery research community. The present research is thus oriented to study the effects of non-classical boundary conditions on computations relevant for the design of aero-engine combustors.

Objectives and present contributions

Specific technological problems related to combustor liner cooling design were selected for investigation. Among the many possibilities, those one for which standard simulations proved inadequate to predict the relevant engineering quantities were chosen. A critical analysis of the state of the art for the computational techniques applied to those cases showed possible improvements to align the open-source code to the more advanced research codes. In particular effusion cooling heat sink predictions highlighted the need for an efficient fluid/metal energy transmitting interface. Furthermore the study of turbulent internal flows, e.g.impinging jet, revealed a strong dependency on externally provided fluctuations to promote the generation of coherent turbulent structures able to correctly predict the complex flow fields connected with such cooling schemes. Finally the study of the acoustic response

of perforated liners under the excitation of thermally driven pressure waves, fundamental to successfully damp combustion instabilities, is strongly simplified in case acoustically transmitting boundary are available.

The aim of this thesis is therefore to implement, validate and assess the capability of such boundary conditions to correctly predict the investigated flow features.

Computational approach and tools

The framework in which these boundary treatments are developed is, as already stated, the one connected with open-source CFD codes. Among the many codes released nowadays under GPL licence [2, 3, 14, 123], the one offering the widest capabilities and the highest flexibility in expanding the code implementing user-defined modules is without any doubt OpenFOAM® [100], that is certainly also the most used open-source CFD code. Together with the expertise already acquired during a previous research focused on steady-state computations of the heat transfer in gas turbine secondary air systems [27, 93], these were the main reasons for which this code was chosen as a background for this work. This code is actually a collection of libraries implementing implicit and explicit finite volume discretization for differential operators such as ∇ or ∇^2 on polyhedral unstructured meshes and efficient linear algebra solvers. It is fully parallel via the domain decomposition mode and it also releases ready-to-use fluid-dynamic solvers for both RANS and LES turbulence modeling. Originally developed for incompressible simulations, these solvers exploits mainly a pressure-based approach also for compressible cases with pressure-velocity coupling achieved by means of SIMPLE (Semi-IMplicit Pressure Linked Equations) [102] loop for steady-

state and PISO loop (Pressure Implicit with Splitting of Operators) [77] for transient cases. Such general overview of the code, certainly not sufficient to fully describe its capabilities, is given to address the reader towards a better understanding of the specific computational methods selected in this work. Specific widening are proposed through out the thesis about subjects relevant for the present work.

Thesis outline

This thesis is structured as follows:

Chapter 1   present a review of the computational strategies employed for combustor cooling. The most common approaches for computational boundary modelling with the related capabilities and drawbacks are afterwards discussed. The focus is on boundary types in use for heat transfer and aeroacoustic analysis in turbo-machinery applications.

Chapter 2   investigates the fluid/metal thermal coupling across wet surfaces. The conjugate heat transfer algorithm developed is explained, together with details on the generic grid interface treatment. Applications to steady state computations of effusion cooling plates are presented and analysed.

Chapter 3   deals with the generation of turbulence at inflow boundaries and specifically with the implemented recycling technique. The different types of recycling and scaling are analysed. LES computations of an axisymmetric impingement jet with heat transfer is used as a reference test case.

Chapter 4   goes through the derivation and the construction of the Navier-Stokes Characteristic Boundary Conditions (NSCBC). Both the general algorithm and the specific techniques in use are reported. Their capability of modelling acoustically excited boundaries is assessed by means of periodic jet LES aimed at evaluating the aeroacoustic response of a perforated screen with bias flow.

Chapter 5   summarizes the main achievements and draws the conclusions of the assessment. A path for possible future work is also discussed.

At the end of the dissertation some appendices are also included. They present those arguments that are a basis for this thesis but not a specific object of the dissertation. In particular:

Appendix A   describes the mathematical derivation of the Navier-Stokes equations in characteristic form (NSCE).

Appendix B   presents a theoretical estimate of the relaxation coefficient for the Linear Relaxation Method implemented in the NSCBC.

Appendix C   reports the linear algebra necessary to introduce the pseudoinverse matrix as a tool to solve overdetermined systems.

Appendix D   deals with the Proper Orthogonal Decomposition (POD) and its applications to turbulent fluid flow.

Chapter 1

The role of boundary conditions for combustor cooling analysis

Contents

In the following chapter present-day aero-engine combustor development trends are introduced with special focus on design strategies for the cooling systems. A review of the numerical studies presented in literature on the subject is proposed analysing separately impingement and effusion devices. Afterwards the three subjects identified as the main open issues concerning boundary modeling for accurate simulations of combustor cooling devices are first introduced and then discussed one by one. Each problem is over-viewed and the "state of the art" for possible boundary treatments is revised.

1.1 Combustor design trends

The always increasing use of aeroplanes for people and goods transportation has boost engineers towards the design of more and more powerful and fuel efficient engines in order to satisfy economical interests as well as environmental issues. Such objectives can be achieved increasing thrust and thermal efficiency of the core engine by means of higher overall pressure ratio and higher turbine inlet temperature [65]. Both these technological trends favour the production of nitric oxides (NOx) as in common aeroengines the chemical process is ruled by the Zeldovich mechanism [85, 86]. Severe regulations on pollutant emissions have on the other hand been issued by international organizations to certificate aeroengines, and stricter and stricter rules are expected to come.

The most promising approach to cope with this dual optimization procedure is the lean premixed combustion technology, working with low fuel to air

ratios to avoid high temperatures of near stoichiometry conditions [91]. Although still not at a production level, demonstrator engines employing such technology have proved the NOx reduction potential [80]. In lean combustion up to 70% of the total combustor air flow has to be premixed with the fuel before entering the reaction zone within the combustor module. Therefore, cooling flow has to be reduced accordingly to provide sufficient air for mixing [23].

Lean combustion comprises the lean direct injection of fuel, premixing with air and at least a partial pre-vaporisation of the fuel before initiating the combustion process. The optimisation of homogeneous fuel-air mixtures is the key to achieve lower flame temperatures and hence lower thermal NOx formation. However, this homogenisation has a strong adverse effect on combustion lean stability, drastically narrowing the operating and stability range [38]. The arising combustion instabilities are mainly due to the fact that those flames operates near the lean limit of flame blow out, in these conditions, small perturbations of fuel to air ratio creates significant variations of the chemical heat release generating density and pressure fluctuations. Such unsteady pressure fluctuations propagates in waves inside the combustor interacting with the mean flow decreasing substantially the reliability and the operating safety of the engine. Both active and passive control systems, e.g. Helmholtz resonators or quarter wave ducts, have been implemented in heavy-duty gas turbine where weight and space constraints are not an issue. For aeroengines instead it is particularly attractive to exploit acoustic damping properties of multiperforated plates already employed in the combustor cooling devices [74].

Summarizing, in order to sustain lean premixed combustion, combustor cooling technology needs to face both a significant cooling flow reduction

and the maximisation of the combustion generated thermo-acoustic wave absorption.

1.2   Combustor cooling systems

Two different and parallel development paths have been followed in the course of the years for the design of cooling systems for the hot gas path [36]: the enhancement of the heat transfer in the cold side and the protection by means of a film of fresh air on the hot side. Concerning the former aspect, the high thermal loads in the combustion chamber makes the implementation of forced convection systems not suitable without the heat transfer increase due to turbulence promoters such as ribs, dimples and pins. Those features have beneficial effects due to an enlargement of the exchange area and the higher heat transfer coefficient associated with the highly turbulent flows arising on such components. Anyhow the most promising way of enhancing the cold side heat transfer is by means of impingement jets as pointed out in [49, 69, 126]. All these works were focused on studying such technology specifically for combustor cooling. Different configurations combining impingements with ribs and pins were studied, revealing that no substantial increase of heat transfer obtained in the base configuration could be achieved. Such technique is hence a promising candidate for future improvements of heat shield and liner cooling. It is also commonly employed on the back side of the dome where the efforts of the internal fluid dynamics are directed towards an optimization of the combustion process and the implementation of film, slot or effusion protections may result problematic due to the high dependency on swirl [139] and free stream turbulence [119].

For the liner instead those cooling devices are widely employed in regular

arrays with stream and span wise pitches optimized to reduce coolant consumption and maintain desired cooling performance. The main limitation of film protection is in fact its degradation receding from the injection requiring quite closely spaced feeding ducts. Even though slot cooling certainly assure the highest film protection, generally full-coverage effusion cooling is preferred due the lower coolant consumption and the high global cooling performance obtained both by a combination of high adiabatic film protection and high heat sink effect in the holes [57]. The aerothermal behavior of such a device has been widely studied both concerning the flow field and the adiabatic temperature distribution [115, 117]. Efforts have been directed also to the study of the overall effectiveness accounting for conduction in the metal sheet and, even more important, for the forced convection inside the hole [51, 52].

1.3   Literature review of numerical studies

As regards numerical computations, due to the largely different length scales characterizing the main fluid dynamic of the reactive zone and the cooling devices and the consequent high computational cost associated, combustion chambers cooling systems are generally studied as a separate domain with respect to the main flow. Few attempts are reported concerning the solely aerodynamic characterization of the coupled system, for example Andreini et al. [9] proposed a correlation for the effusion holes discharge coefficient of a specific lean premixed combustor based on a database of 2-dimensional CFD computations performed at different flow conditions. In order to cope with such decoupling of the domains, an interesting attempt was performed by Mendez et al. [95] who proposed a simple model, independent of the grid in

the near-wall region, to account for effusion through a multi-perforated plate. Only by externally providing the discharge coefficient law, the porosity and the angle, the model, developed to fit numerical results from a direct simulation of bi-periodic holes with effusion [96], computes suitable wall fluxes from the local flow conditions both at the suction and at the injection side. Even though the obtained results were promising in terms of streamwise velocity profiles the chosen test case was affected by two main limitations: it was composed of a multiperforated flat plate with uniform external flow conditions and the reference experiment as well as the model was not accounting for any heat transfer effect.

Analyses of cooling systems not considering the effects of the main combustor flow can be found in large quantities. Being real systems usually composed by repeatable arrays of a big number of smaller units, such as a single impingement or a film cooling jet, the literature comprehends both studies of the detailed aero-thermal behavior of single isolated components and global simulations of the interaction effects. In the following sections the most interesting numerical works concerning impingement and effusion systems will be analysed separately.

1.3.1 Impingement cooling

The literature of numerical computations focused on impingement cooling is quite wide as far it is relevant for gas turbine cooling (also blade and casing cooling) but also for computer cooling where recent studies report an heat transfer rate as high as $10^7 \ W/m^2$ [125]. Concerning detailed predictions of isolated impingement jet with heat transfer, an early work of Behnia et al. [21], who performed RANS simulations at various H/D and various Re, showed how standard $k - \varepsilon$ largely overestimates the Nusselt number

($> 150\%$) due to an overproduction of turbulence around the stagnation point. The use of realizable turbulence models such as the $v^2 - f$ removes the peak of turbulent kinetic energy around the stagnation point thanks to a limiter in the production term and reduce the gap between prediction and experiments up to around 10%. They also find out that for H/D=2 a second peak of heat transfer coefficient is developing around r/D=2 for Reynolds numbers higher than 50000. In a subsequent paper [22] the same authors investigated, together with an additional configuration with a square pedestal in the stagnation region, the influence of the confinement and of the nozzle exit profiles for H/D ranging from 0.1 to 2. They focused on Re=23000 and, as learned from the previous work, used the $v^2 - f$ turbulence model. They showed how the confinement has a quite large effect for the Nusselt number at small H/D while it is completely negligible at H/D = 2. Even more interesting is the analysis performed on the influence of the feeding pipe length for the H/D = 2 case: they construct three different velocity profiles reproducing fully developed channel flow conditions as well as flatter boundary layer profiles characteristic of short pipes at two different turbulence levels. The choice of the velocity profile is largely affecting the Nusselt number up to r/D=2 both in terms of stagnation point peak ($\pm 50\%$) and in the development of the secondary peak.

Unsteady analysis was performed by Chung et al. [40] by means of a 2-dimensional direct solution of the Navier-Stokes equation for a slot impinging jet with heat transfer at very low Re = 300, 500 and 1000. They showed the time history of the Nusselt number at the stagnation point showing larger fluctuations with increasing coolant mass flow rate. Analysing vortical structures developing in the shear layer, they distinguish two different situations corresponding respectively to a peak and a minimum in the heat transfer

coefficient: the first one when the vortex is deviated from the axial towards a radial movement while impinging on the wall and the second one when the vortex is convected towards the wall and compress the stagnating fluid. They also provide space-time contour plots to demonstrate how the higher temporal fluctuations correspond to larger spatial dispersion of the corresponding structures.

A more complete work is that one of Hallqvist and Fuchs [62, 63, 64] who investigated by means of Large Eddy Simulation round impingement jets with heat transfer at Re = 20000 both with and without swirl at the inflow. They also studied annular impingement jets, waving inlet forcing and the influence of nozzle exit mean velocity profile. They used an incompressible code with heat transfer computed from a passive scalar transport equation. Concerning the inlet boundary condition analysis, despite the fact that they found out a strong effect on the fluid flow, they conclude that a top-hat velocity profile is sufficiently accurate reproduce the thermal field characteristic at the various H/D considered (0.25-4) in case of non swirling jets. They also presented a power spectral density curve for axial velocity component within the annular shear layer discovering that for H/D = 4 the unsteady behavior of the three considered boundary conditions, namely the top-hat, a mollified profile and those one specified from a precursor simulation, is similar while at lower H/D the mollified profile strongly reduce the fluctuating behavior.

More recently Hadziabdic and Hanjalic [61] presented a detailed investigation of the impinging round jet at Re = 20000, providing a complete description of the numerical methodology employed as well as a wide discussion of the flow features highlighted. They found out that the dominant phenomenon driving the flow in the three regions, characterized as the free jet, the stagnation region and the wall jet, see Sec. 3.4.1, is the formation of

the roll-up vortices generated by instabilities in the shear layer. The Strouhal number of this ring-vortex production was evaluated to be 0.64. They observe that these vortices while flowing towards the plate tilt and finally breakdown before impinging on the wall. The periodic jet shrink and expansion leads to jet flapping and the stagnation point move around the geometrical center occasionally branching in two separate stagnation points. Concerning the heat transfer coefficient, they noted how the instantaneous Nusselt number follows the distribution pattern of the friction factor except for the stagnation point. They conclude stating that gridding strategy is crucial for such kind of computation since, irrespective to the sub-grid model in use, a fine grid resolution is required at the wall and in the shear layer. They also stated that even though unstructured tetrahedral grids could rationalize the total number of grid cells, the use of non-hexahedral elements increase uncertainty on the accuracy and fidelity of LES.

The heat removal of the impingement jet is largely affected by the fluid dynamic conditions of the discharge plenum and the effect of neighbor jets may alter significantly the development of the wall jet. The study of packed arrays of impingement jets has been therefore subject of analysis as well. For example Bailey et al.[17] performed a numerical investigation of a flat plate rig reproducing entirely a quarter of a combustor compound cooling system composed of an impingement array with crossflow and turbulators for heat transfer enhancement. They exploited $k - \epsilon$ with wall function and the Two-Layer model; comparing an heat transfer coefficient relative error map (with respect to experimental data) they showed that the latter was sensibly reducing the predictions spread especially in the convection zone. The computational grid for the second case was however three times bigger in size and authors stated that the computational cost of the second approach

may become prohibitive for more complex arrangements.

Another work considering real geometries for combustor liner impingement cooling, i.e. small diameter sparse arrays, is that by Andreini et al. [12]. They consider a 9 rows impingement array discharging in a one-side closed gap, in this way the crossflow is generated only by the air coming from the neighbouring jets. They performed a turbulence model assessment (a Low-Reynolds and a Two-Layer $k - \varepsilon$ together with the $v^2 - f$ model) on a single jet domain showing that the Two-Layer model was the only one able to correctly reproduce the peak Nusselt in the stagnation area. They subsequently extended the domain to include the first 5 holes and used outflow conditions as boundary condition for a separate computation involving other 4 holes. Nusselt number distribution on the plates were finally collected to obtain predictions for the first 9 rows. They revealed a stream wise decrease of centerline peak value starting from the 6th row that was not so strongly measured in the experiment. Area averaged Nusselt number is however in good agreement with experiments for the entire plate.

As regards acoustic predictions no analysis specifically devoted to the evaluation of the acoustic damping connected with impingement arrays exists to the author's knowledge. Even though the acoustic behavior of the cold side of the cooling system might have some effects on the flame as well, research is focusing on the main affecting device: the multiperforated plate facing the reactive zone used for effusion cooling.

1.3.2 Effusion cooling

Computations of effusion cooling systems result to be very challenging compared to more common film cooling configurations for several reasons: the huge number of holes involved that increase the computational cost and aug-

ment the heat removed by convection in the hole, the highly slanted angle that makes the grid generation more complicate and the reduced hole diameter enlarging the difference in relevant scales between the main and the in-hole flow. Moreover the possibility to employ higher blowing ratio without entering the full penetration regime makes flow conditions particularly difficult to solve for the simultaneous presence of high and low Mach zones. That is why highly costly turbulence treatments such as LES or DES, becoming more and more popular for the study of jets in cross flow and film cooling [6], are rarely encountered in the study of effusion systems which are focused on steady-state RANS analysis often exploiting turbulence model assessments performed on film cooling cases (generally at 30°).

Among the various works on RANS turbulence modeling for film cooling it is worth to mention the work by Hassan and Yavuzkurt [68] who tested the standard, RNG, and realizable $k-\varepsilon$ models as well as the standard $k-\omega$ model in an adiabatic configuration surprisingly discovering that the standard $k-\varepsilon$ model was the most successfully reproducing the experimental trends. Hoda and Acharya [70] performed an analysis of the flow field developing in case of square holes with normal injection. Seven two-equation models employing $k-\varepsilon$ and $k-\omega$ closures, broadly categorized as high-Reynolds number formulations, Low-Reynolds number formulations, DNS-based formulation, and non linear formulations were employed to simulate the flow. They found that the Lam and Bremhorst, that is a Low Reynolds $k-\varepsilon$ model generally got the best agreement with experiments but fails to predict the wake of the jet.

More recently Harrison and Bogard [67] performed an analysis of the performance of the standard $k-\omega$ model, a realizable Two-Layer and a Reynold's stress model on a single hole film cooling in adiabatic and heat

transfer configuration. They pointed out a strong dependency on turbulence modeling of the adiabatic effectiveness while the heat transfer was reasonably well predicted by all the three models. Even though they conclude that the choice of the best turbulence model is case dependant, they found that standard $k-\omega$ model was giving the best results in terms of laterally averaged effectiveness and heat transfer.

Further improvements were obtained by Lakheal et al.[82] who proposed a modification of the anisotropic correction for eddy viscosity models originally proposed by Bergeles [25] to be used in conjunction with the Two-Layer model. The same model was exploited by Bacci and Facchini [16] and by Bianchini and Mangani [31] for effusion geometries. The former work extended the analysis of single hole configurations, while the latter, after repeating the obtained results on classical literature test cases, exploited the model for multirow effusion plates showing a less marked dependency on the anisotropic correction compared to film-cooling cases due to the higher blowing rates obtained and the consequent higher relative weight of the convective terms.

Even though modeling issues on the adiabatic behavior of effusion jets are far from being solved, several researcher investigated the fluid motion in case of heat transfer. In particular it is of interest to reproduce correct wall thermal distribution by means of a conjugate solution of the energy equation in the fluid and the solid domain. Andreini et al. [11], performed a comparison of full 3-dimensional CFD conjugate analysis of on a 30° angled multi-perforated plate with lower order prediction methods and experiments. They reduced the domain including only the first 8 rows of holes, however in order to provide adequate thermal conditions lateral surfaces of the metal sheet were maintained at a prescribed temperature obtained from a correla-

tive analysis of the entire system. Jeromin et al. [47] also exploited conjugate heat transfer to analyse the aero-thermal behavior of two 8 holes plates made of materials with different conductive properties. They considered a much more slanted angle (17°) and compared the obtained results with experimental data both in terms of spanwise averaged overall effectiveness and heat transfer at the wall as well as velocity and temperature profiles at several stations inside the channel. The investigated flow conditions reproduced blowing ratios ranging between 0.5 and 1.2. They found out that the averaged heat transfer level is well reproduced by numerics and is pretty insensitive to the blowing ratio, the effectiveness instead is mispredicted, also in terms of trends, especially for the low blowing ratios and the low conductive material.

More complex configurations were investigated by Ceccherini et al. to study the interactions between different cooling techniques, such as slot and effusion cooling. They computed adiabatic effectiveness [39] and heat transfer [10] at the wall exploiting the $k - \omega$ SST turbulence model at high velocity ratios ranging between 3 and 7 for the effusion and 1 for the slot. Even though quite largely overestimating the adiabatic effectiveness, they were able to reproduce the trend of decreasing effectiveness with increasing velocity ratio typical of fully penetrating regimes. Analysing the flow field they pointed out the flow structures responsible for the main flow attraction towards the plate in case of higher velocity jets. Concerning the heat transfer they vice versa reproduced pretty well the experimental values highlighting an increase of heat transfer coefficient with the blowing ratio both in case of active and non active slot cooling. They also performed an analysis on the density ratio effect injecting carbon dioxide as coolant discovering that the main parameter governing the heat transfer is the velocity ratio.

The literature concerning acoustic investigations of perforated liners by

means of CFD is relatively poor, mainly due to the very high computational cost of direct acoustic simulations compared to specific CAA methods. Even though the computational cost of a single bi-periodic hole subject to acoustic excitation can be considered equivalent to that of an aerodynamic or heat transfer analysis, the acoustic behavior is strongly dependent on the entire combustor (if not the entire engine) geometry and providing adequate acoustic characterization of the boundary is often impossible. That is the reason why analyses of reduced domains including few effusion holes are not reported in literature and most of the works deals with acoustic characterization of bi-periodic single hole plates. Eldredge et al. [48] for example performed an incompressible LES to estimate the acoustic impedance of the test conducted by Mendez and Nicoud [96], i.e. high porosity 30° plate at very low bias Mach=0.008 and moderate grazing flow, and compared it to the modified Howe model [71]. They acoustically excite the plate by means of a pulsating inlet velocity at frequencies ranging between 89 and 890 Hz. They reported a moderate agreement at low frequencies but they suggest that the model should be improved for more advanced modeling of the thickness and the tilt angle. Later Mendez and Eldredge [94] extended the same type of analysis to reproduce an experimental test, at low bias Mach and no grazing flow with a 90° plate, conducted by Bellucci et al. [24]. They used this test to propose an homogeneous acoustic model to avoid the very costly procedure of including the hole in the computational domain. They were therefore able to perform a reactive LES simulation of an entire helicopter combustor including both the hot and the cold side coupling the two domains with the acoustic model proposed. Comparing the results obtained with a previous reactive LES not considering the effect of the effusion system, they showed how the multiperforated liner was able to almost perfectly damp the acoustic

peak arising at $St \approx 2.8$.

1.4   The influence of boundary conditions

The certainly far from complete review of the wide literature concerning numerical modeling of combustor cooling devices, highlighted several issues for which the boundary treatment become critical for the success of the computation. Even though few of the presented works were directly addressed towards the evaluation of the effects of the boundary conditions, those one performing a sensitivity analysis showed a dramatic dependency on the boundary treatment. At least three different areas of investigation for which accurate and efficient boundary modeling is required, could be pointed out.

First of all is the thermal modeling of effusion plates: the criticality of the energy conduction in the metal plate was evidenced. In order to correctly reproduce the overall cooling effectiveness of the system, the two problems of film protection and heat transfer enhancement should be resolved simultaneously thus a conjugate interface needs to be implemented.

Second comes the injection conditions for the coolant jets: irrespective to being impingement or effusion jet, mean profile as well as turbulent characteristics play a fundamental role in the development of the jet wake. Hallqvist [62] showed how nominally equivalent inflow velocity profiles strongly affected the heat transfer level. A boundary to generate turbulent inflow conditions, for velocity but also for the other variables, is hence required to enhance the fidelity of LES computations.

Moreover the acoustics computations are by nature more affected by the far field conditions and the reflectivity of the boundary may become problematic forcing to enlarge the computational domain. Even though very accurate

analyses are required for the evaluation of acoustic boundary conditions and thus the desired behavior of the boundary itself is often unknown, at least the ideal limit of totally reflecting and totally transmissive boundaries needs to be available within the CFD code.

1.5 Fluid solid interface

1.5.1 Overview

The solid wall condition in computational fluid mechanics is one of the most straight forward for the velocity: since the wall is impermeable, the streamlines need to be parallel to the prescribed surface. In particular if the fluid is viscous no finite jump of velocity is allowed between adjacent streamlines, thus in this case where one of the streamline is the wall wet surface the noslip condition applies: the velocity of the fluid brushing the wall is equal to the wall velocity. In the quite common case of stationary wall this reduces to $U_w = 0$. Even though such a condition introduces strong gradients in the velocity field forcing the spatial discretization to increase normal resolution, the physical modelling of such a boundary type is not affected by detectable errors. Additional modelling may be introduced by means of a wall function to avoid the fine near wall clustering required by the so called Low-Reynolds approach. However the velocity wall boundary condition is usually not directly manipulated, rather to satisfy the proposed wall function correction terms are introduced in the wall viscosity and in the turbulent equations. The momentum fluid/solid interface is thus almost universally modelled as a no-slip boundary condition, at least in the framework of turbulent flows and rigid wall surfaces.

Concerning the thermal wall boundary condition the situation is different:

energy can be introduced or subtracted from the solid domain, thus a mutual coupling is evidenced. In more detail no energy production or dissipation is experimentally revealed at the solid fluid interface with both energy balance and temperature continuity strictly satisfied on the solid to fluid transition. This mutual interaction does not permit an universal treatment such as the one proposed for velocity. Possible solutions to the thermal wall boundary conditions are revised in the following section.

1.5.2 State of the art

Most of the heat transfer simulations consider the solid domain as a separate domain and a decoupled wall boundary condition is employed. Such decoupled boundary conditions may specify the wall temperature or wall heat flux. For the case where the distribution of one of these two quantities is available on the wall surface under consideration, the simulation does not show big differences with the reference flow field. However it is not common to have adequately resolved distributions available for many engineering relevant flows and strong modeling and simplifications should be applied, e.g. uniform temperature or heat transfer distribution. Values in fact generally come from available correlations and/or experiments and usually refer to spatially and temporally averaged conditions. Moreover such experimental or correlation based values are usually available for the heat transfer coefficient, thus a mixed condition based on a linear combination of specified temperature and heat flux needs to be implemented. In the case of moderate and uniform heat transfer and almost isothermal flows, the hypothesis of heat transfer coefficient independence from thermal conditions performs well and these decoupled conditions usually lead to reliable predictions.

However these constraints are not satisfied by many engineering relevant

flows and thermal coupling between the solid and fluid domain is a key factor in the success of the prediction. This coupling consists of imposing the concurrent continuity of heat flux and temperature across the interface. In order to achieve this, the solid parts should be included in the computational domain where the energy conduction equation needs to be resolved. The higher computational cost is usually paid off by more realistic results in terms of heat transfer rate and flow field. Typical applications in turbomachinery for which this gain is worth the additional cost are the study of densely drilled effusion plates with high L/D ratio [33], of long and thin internal cooling ducts at low coolant mass flow rate [83] and in the case turbulence promoters of high aspect ratios and different conductive properties are employed [89]. Concerning experiments, that are conjugate by definition, there are fewer investigations specifically developed to assess the effect of conduction in the solid domain on the surface distribution of the thermal field. Recent publications suggest however that this effect could be studied with more detail in the near future [41].

From a computational point of view many procedures have been proposed in the literature to achieve conjugate heat transfer conditions. Typical industrial procedures to compute the working temperature distribution on an airfoil for example consists of (see [37]):

- solving two separate fluid dynamic conditions to evaluate both the external and the internal heat transfer coefficient,

- using these results as a boundary condition for a thermal solver for the conduction in the solid.

However, as long as flow and solid temperature calculations are kept uncoupled from each other, one may need several iterations before the continuity

of temperature and heat flux are satisfied within a specified tolerance. The main drawback of such an approach is that feedback from the solid to the fluid domain and vice versa is only assigned once a first solution is obtained. Since most computational solvers, irrespective whether they use FEM or FVM, Navier-Stokes or Fourier solvers, employ iterative solution techniques, such exchange of information between the two sides of the interface may be accomplished before the solution is obtained to fasten the overall convergence rate. Depending on the characteristic convergence properties and the computational cost of the two solvers as well as the ease of the exchanging procedure, it is possible to assess a best practice to optimize the update of the thermal boundary conditions. A novel approach aimed at increasing convergence speed of the entire procedure is proposed in Ch. 2.

1.6 Turbulent inlet

1.6.1 Overview

Generating inlet conditions for LES is considerably more difficult than it is for RANS since all turbulent structures associated with resolved scales need to be specified. For RANS simulations in fact, turbulent boundary conditions do not affect the boundary conditions for the resolved unknown (velocity, temperature etc.) that represent the mean flow properties and can be easily assigned specifying characteristic integral scales such as the turbulent velocity and length. For a direct solver of turbulent flows (LES or DNS) this is not sufficient since the unknowns to solve for represent the instantaneous fluctuating properties and additional information concerning the fluctuating field needs to be provided. Provision of this additional information is not an easy task since the prescribed fluctuations should represent the actual evolution

of the flow field in that section. Furthermore, the more scales are solved, the more information need to be specified. Unfortunately the required spatial and temporal accuracy makes the use of experimental data almost impossible for the assignment of the time evolution of the flow field. It is hence necessary to develop such series of states by means of computational techniques. According to Tabor and Baba Ahmadi [128] the "perfect" boundary should:

- be stochastically varying

- . . . on scales down to the filter scale (spatially and temporally)

- be compatible with the Navier-Stokes equations,

- "look" like turbulence,

- allow the easy specification of turbulent properties (turbulence intensities, length scales etc.),

- be easy to implement and to adjust to new inlet conditions,

- be cost efficient and computationally cheap

They also address the issue of correctly reproducing the different behaviors in the various zones of the inlet reproducing isotropic turbulence in the freestream zone and damping the normal-to-the-wall fluctuations in the near wall region. Moreover the prescribed conditions should be compatible with SGS model in use especially in the near wall layer where hybrid methods and/or the use of wall modeling may affect the behavior of the prescribed field.

All these requirements are difficult to satisfy concurrently and no "perfect" boundary has been proposed so far. Employed methods usually focus on some aspects, and depending on the priorities, stability and cost could be favoured to the detriment of accuracy and vice versa.

1.6.2 State of the art

Several methods have been proposed in the literature to deal with the stated requirements. Typical classifications of these techniques are based on the method used to generate the imposed turbulent fields; two main classes are identified:

- Synthesised turbulence methods

- Recycling methods

Synthesised turbulence methods reconstruct fluctuations by means of theoretical functions or random generation, while recycling methods exploits turbulence numerically obtained from separate computations.

Among the many artificial methods, those based on Fourier series, digital filtering and Proper Orthogonal Decomposition (POD) are the most common. The basic idea of these procedures is to define a set of basis functions to reconstruct the turbulent fluctuations by means of temporal coefficients and finally superpose them on a prescribed mean field. The temporal coefficients are usually generated randomly and then treated to respect desired turbulence properties, while the basis functions may either be specified by theoretical analysis (Fourier series) or by modal analysis of the flow field (POD). These methods are relatively easy to implement independently from the inlet conditions to be specified. The level of accuracy in reproducing the turbulent characteristics may vary on the chosen method and the case of interest but it is generally difficult to generate time and spatially correlated structures really adapting to the desired flow conditions.

The second class of methods exploits turbulent structures obtained by numerical flow simulations. In such a way the obtained fluctuations really look like turbulence since they are obtained by directly solving the filtered

Navier-Stokes equations. Of course the generating simulation needs to be at least as accurate as the main one, to correctly reproduce the desired flow conditions and to reach statistically steady state or reproduce eventual transient behavior. These types of conditions may rely on cyclic domain definition, on concurrent simulations or on internal mapping. Issues related with this choice are connected with the extra computational cost and the ability to adapt to different mean flow conditions as well as the specification of turbulent integral quantities.

In the turbomachinery research community, the application of LES has reached the status of "state of the art" for a certain class of investigations in which RANS modeling was particularly failing. This class includes specific applications involving the heat transfer and aeroacoustics of the gas turbine combustor, such as the study of simplified combustors including reactive aerodynamics [34], flow dynamic of swirl injectors [137], aeroacoustic performance of perforated liner with bias flow [94], and single hole film cooling thermal development onto flat plates [96]. Anyhow a best practice to assign suitable boundary conditions has not been developed yet. Some techniques still take advantage of RANS type boundary conditions [84], others use a turbulence-library database to generate appropriate boundary conditions [103, 108], whilst others superpose an assigned level of fluctuation to steady state conditions often using Gaussian white noise distribution [137] but also implementing more sophisticated approaches [81]. This thesis will contribute by proposing an auto-recycling technique as described in Ch. 3.

1.7 Non reflecting boundary conditions

1.7.1 Overview

Classical boundary conditions with fixed specified value have a reflecting behaviour, which is highly undesirable for unsteady simulations and in LES and DNS especially. This aspect becomes crucial in aeroacoustic simulations for which the reflecting properties of the boundary may affect dramatically the acoustics of the system. Most of the research conducted on non reflecting boundaries is in fact related to aeroacoustic problems.

In subsonic flows, from the theory of characteristics the standard outlet boundary condition for example consists of an imposed pressure together with extrapolation of other variables. However knowing the exact spatial and temporal distribution of the pressure over the outlet surface is usually out of the question and only mean and average values are available. Fixing such values as the prescribed outflow pressure leads to a totally reflecting outlet which may behave significantly differently from an open duct termination as it usually is for internal channels simulations. In order to guarantee the incoming upstream perturbations to be negligible in the internal domain, the outlet boundary should be shifted downstream. The availability of non-reflecting boundary conditions will hence lead to large computational savings.

In order to permit waves to pass undisturbed across the boundary, the value on the boundary itself should adapt in time to follow the internal domain values. However in such a way it is not guaranteed any more that the mean properties will be respected and the flow conditions in the internal domain may be altered. In the literature many techniques have been proposed so far to cope with this combination of non reflectivity and maintenance of prescribed values. Depending on the applications of interest, stress is posed

more on the non reflecting behavior or on stability issues as well as on the capability to maintain desired values.

1.7.2   State of the art

This section presents some of the approaches to implement non reflecting boundaries proposed in literature.

Convective outlet: Created by Orlansky [101] and typically known as a convective outlet, its formulation consists in the solution of the following transport equation on the boundary:

$$\frac{\partial \psi}{\partial t} + C \frac{\partial \psi}{\partial n} = 0 \tag{1.1}$$

In Eq. 1.1 n is the normal to the boundary and C is the characteristic wave propagation speed. In compressible flow C is usually assumed equal to the acoustic speed $\left(C = \sqrt{\frac{\partial p}{\partial \rho}}\right)_s$ while for incompressible flows the characteristic convective velocity is taken. In the latter case the criterion for the appropriate choice of C may be the mass flow rate at the outlet, since this has to balance the mass flow rate at the inlet.

Absorbing layer: This technique consists of an additional zone of grid points around the domain where an artificial damping or dissipation is introduced so that perturbations may be dissipated before reflecting upstream in the computational domain. In the classical approach such as that of Israeli and Orszag [76] the sudden increase in viscosity transforms the absorbing layer in a reflecting boundary. This justifies the recent evolution of the absorbing layer technique: the perfectly matched layer (PML) technique formulated for Euler equations by Hu [72]. In contrast to the absorbing layer

method, the PML technique adopts an increasing numerical viscosity in the absorbing layer, also called the sponge layer, which is zero at the computational domain interface. Thanks to this method the region of sponge layer near the interface is totally non-reflecting because the same equations are solved as for the rest of the computational domain.

Fig.1.1 reports results from a recent application of the PML by Hu et al. [73] to a vortex shedding flow around a cylinder.
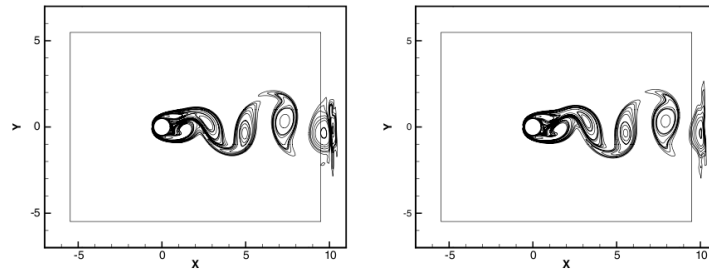
Figure 1.1: Vorticity contour plots over a period of vortex shedding (from Hu et al. [73])

NSCBC: This method, firstly proposed by Poinsot and Lele [107], is based on characteristic analysis to distinguish between incoming and outgoing waves on the boundary. The Navier-Stokes equations in characteristic form are integrated on the boundary to advance in time primitive variables. The boundary normal terms are prescribed for the incoming wave and calculated from the interior points for the outgoing waves. In such a way the outgoing waves pass undisturbed across the boundary. In order to avoid drift from the mean prescribed values, a Linear Relaxation Method [141] has been proposed. It consists of an extra forcing term acting as a spring centered on the desired value: the higher the drift the higher the opposing forcing term.

Due to the very good non reflecting conditions and the capability to incorporate acoustic forcing necessary to excite the perforated plates of the effusion system, this last technique was implemented and described in Ch. 4.

Chapter 2

Conjugate Generic Grid Interfaces

Contents

The main aim of this chapter is to introduce the algorithm implemented to perform conjugate heat transfer analysis on unstructured grids. Firstly the implicit thermal coupling between the solid and fluid domain is examined, then the generalization to non conformal interfaces is discussed. Finally a conventional and shaped effusion plates are analysed subject to conditions typical of real engines at two different thermal conditions. The overall effectiveness of the system is investigated.

2.1   The conjugate procedure

As already discussed in Ch. 1, performing conjugate calculations to include the effect of different thermal conditions at the various positions on the solid boundary achieves a higher level of fidelity in the evaluation of thermal loads on metal components and in the temperature distribution within the fluid flow.

The conjugate boundary condition basically consists of two constraints to be maintained across the solid-fluid interface, i.e. continuity of temperature and heat flux, see Eqs. 2.1 and 2.2

$$T_{w,solid} = T_{w,fluid} \tag{2.1}$$

$$k_{solid} \left(\frac{\partial T_{solid}}{\partial n} \right)_{wall} = -k_{fluid} \left(\frac{\partial T_{fluid}}{\partial n} \right)_{wall} \tag{2.2}$$

Once these conditions are satisfied the conjugate thermal solution is achieved even for the case where the fluid domain was solved separately from the solid one. A possibility is thus to couple the two domains in an

explicit manner using appropriate boundary conditions coming directly from the adjacent domain. This strategy consists of solving the fluid domain with a guessed interface temperature, extracting the resulting heat flux and using it as a boundary condition for the Fourier equation in the solid domain; the derived wall temperature will then be used as a better guess for the fluid calculation. An iterative loop is thus necessary to achieve the simultaneous solution of both Eqs. 2.1 and 2.2. Many successful applications can be found in the literature both exploiting an automatic communication between two different solvers [32], or integrating the two domains into the same solver [50, 90].

If this procedure can be very promising in case of weak coupling or in case of transient simulations where the time integration already introduces extensive iterative loops, for the analysis of steady-state problems such technique may result in too many iterations being necessary to obtain convergence of the boundary condition [7].

In order to achieve the energy balance on the two domains in a faster way, equations for the two sides should be implicitly coupled: a single problem is hence resolved for both the solid and fluid parts. The interface introduces extra diagonal terms corresponding to the adjacent cells to link the solid and the fluid domains whilst preserving the energy balance.

2.2   The coupled conjugate interfaces

The energy equation for the two domains is written in same form and discretized in the same matrix to be solved for a single unknown: the static temperature. The full Navier-Stokes energy equation describing the fluid thermal distribution in fact reduces to the simpler Fourier equation, i.e. con-

duction in solid, in case the convective fluxes ϕ are null as reported in Eq. 2.3. In order to set the convective fluxes to zero it simply was necessary to impose null velocity in each solid cell.

$$\sum_f \frac{\phi_f c_{p,f} T_f}{A_f} + \sum_f k \nabla T = \sum_f \frac{\phi_f}{\rho_f A_f} \cdot p_f - p \cdot \sum_f \frac{\phi_f}{\rho_f A_f} \xrightarrow{\phi=0} \sum_f k \nabla T = 0 \quad (2.3)$$

In this manner it is easier to treat the coupling between the two sides of the interface in an implicit way: just discretizing the energy flux in terms of both solid and fluid adjacent cell, thus respecting at each iteration both the continuity of temperature profiles and the equality of thermal fluxes across the interface. The coefficients of mutual interaction are directly calculated from the conservation of energy across the boundary face weighting temperature at the cell center with conductivity and distance from the wall. Continuity of heat flux reads:

$$\frac{k_f}{\triangle y_f}\left(T_f - T_w\right) = -\frac{k_s}{\triangle y_s}\left(T_s - T_w\right) \Rightarrow T_w = \frac{\frac{k_f T_f}{\triangle y_f} + \frac{k_s T_s}{\triangle y_s}}{\frac{k_f}{\triangle y_f} + \frac{k_s}{\triangle y_s}}. \quad (2.4)$$

Exploiting Eq. 2.4, expressions for the temperature gradient at the solid and fluid side are found, see Eqs. 2.5 and 2.6.

$$(\nabla T)_{ws} = \frac{1}{\triangle y_s}\left(1 - \frac{\frac{k_s}{\triangle y_s}}{\frac{k_s}{\triangle y_s} + \frac{k_f}{\triangle y_f}}\right) \cdot T_s - \frac{1}{\triangle y_s}\left(\frac{\frac{k_f}{\triangle y_f}}{\frac{k_s}{\triangle y_s} + \frac{k_f}{\triangle y_f}}\right) \cdot T_f. \quad (2.5)$$

$$(\nabla T)_{wf} = \frac{1}{\triangle y_f}\left(1 - \frac{\frac{k_f}{\triangle y_f}}{\frac{k_s}{\triangle y_s} + \frac{k_f}{\triangle y_f}}\right) \cdot T_f - \frac{1}{\triangle y_f}\left(\frac{\frac{k_s}{\triangle y_s}}{\frac{k_s}{\triangle y_s} + \frac{k_f}{\triangle y_f}}\right) \cdot T_s. \quad (2.6)$$

This implicit technique allows faster convergence rates compared to standard explicit coupling used in other codes, due to the fact that energy balance is strictly respected at each iteration step. Since energy balance is strictly respected at any intermediate solution the boundary condition is not affecting the convergence rate in the fluid domain.

This special boundary condition can be applied only to meshes with a fine normal-to-wall clustering on the fluid part because the linear approximation of the temperature profile near the interface can be considered valid in the thermal boundary layer only if the first fluid cell node is close enough to the wall. Same requirements as for Low-Reynolds turbulence models were successfully employed. With such an assumption total and static temperatures coincide close to the wall implying that this boundary condition can be extended also to total temperature equation.

Validation was performed on simple purely conductive 1-dimensional tests to be cross-checked against analytical solutions obtaining perfect matching both in terms of temperature profiles and of heat flux. A turbulent convective test on a flat plate was also performed with very good agreement with available correlations and other codes [138]. Further details about the implemented procedure can be found in [28].

2.3   Generic grid interfaces

In order to ease the mesh generation process and to allow fully independent meshing of the different domains a very general connection algorithm has been developed, to be used also to increase mesh quality in highly curved periodic interfaces. Such an algorithm deals with multiple implicit coupling of cells across a non-conformal interface. The mechanism implemented exploits

a ghost cell (g) to store the contributions of all the neighbour cells (n). In practice boundary flux is implemented following Eq. 2.7, where ϕ is the generic unknown but also the convective flux.

$$\phi_f = w_p\phi_p + (1 - w_p)\phi_g \qquad (2.7)$$

Even though the ghost cell algorithm is usually employed for explicit coupling, its contribution in this case is updated at every iteration of the linear system solver therefore achieving semi implicit coupling between the two sides of the interface.

In order to reduce the effect of the other side of the interface to a single value for the ghost cell, the contribution of each twin cell is weighted on the face overlapping area (α_n), see Eq. 2.8.

$$\phi_g = \sum_n \alpha_n\phi_n \qquad (2.8)$$

A pre-processing tool was developed to calculate and store both the addressing of the cells of mutual interaction and the respective weighting factors, as described in the following.

The overlapping area of the faces can be calculated by means of many algorithms proposed in the literature [4], actually the problem in question is relatively simple as boundary faces are convex, non self-intersecting and always clockwise oriented in order to obtain positive area. Thus the only requirement left for such an algorithm is to be fast enough to limit the additional load over and above the matrix solving to a few percent. In order to keep the implementation simple, since speed in calculating was not a fundamental issue as long as the weights were calculated just once, i.e. the mesh is not moving, the algorithm chosen is the one based on the winding number

(a) WN = -2 (b) WN = -1 (c) WN = 0 (d) WN = 1 (e) WN = 2 (f) WN = 3

Figure 2.1: Winding number of closed curves

[66]. The winding number for a closed planar curve is an integer value specified at each point, off of the curve, but in the plane holding that curve: it is the net number of times that an observer, at that point, turns as he observes a bug traversing the curve once, see Fig. 2.1. The winding number can be positive or negative depending on the direction of the curve surrounding the point: positive for clockwise and negative for counter-clockwise. In the simple case of convex polygons the winding number is simply 1 inside and 0 outside.

The surface integral of the product of the winding numbers of two polygons therefore gives the intersection area:

$$A_{fn-fp}^{overlap} = \int WN_n \cdot WN_p \, dA \,, \tag{2.9}$$

since it is null everywhere except inside both the polygons.

Obviously two polygons in space must be coplanar in order to share a finite portion of area, indeed this can be problematic in case of complex boundaries such as bent pipes, fillets or arbitrarily curved surfaces. To prevent such failure of the algorithm the faces are first projected onto a common plane and afterwards the projected overlapping areas are calculated. This does not invalidate the algorithm, bearing in mind that the relative weight of the overlapping areas is actually the fundamental quantity to be calculated,

as it is shown in Eq. 2.10.

$$\alpha_n = \frac{A_{fn-fp}^{overlap}}{A_{fp}} = \frac{\left(A_{fn-fp}^{overlap}\right)_{projected}}{(A_{fp})_{projected}} \tag{2.10}$$

If the overlapping area goes beyond a prescribed tolerance (usually it is preferable to use a very tight one), the address of the cell is stored in the set of neighbor cells.

This coupling is not restricted to solid fluid interfaces or to the energy equation but as it is explained in this section is general and can thus be applied to spatially coincident interfaces and also to periodic boundaries such as rotational or translational cyclic interfaces with simple additions for the movement of the points generating the overlapping polygons.

2.4   Parallelization

In order to achieve efficient performance, the implementation of the proposed algorithm should be consistent with multi-processor calculation. As stated in the previous section, every ϕ_n needs to be known in order to compute ϕ_g. If all ϕ_n reside on the same processor no extra interprocessor communication is needed and the algorithm would work, with no additional load, in parallel. However since the interface is not conformal it is not possible to decompose the interface maintaining the neighbors entirely on the same processor. An algorithm scheduling processor sending and receiving was thus needed to make the interface working in parallel.

Processor information sharing exploits MPI (Message Passing Interface) communication. The send and receive mechanism is built up in order to include only the nodes actually sharing pieces of the interface boundary, thus not overloading any of the processors with collecting and sending tasks.

During the first iteration the master node collects the face processor addressing. Values for ϕ_n are then stored following processor order in such a way that each processor can receive information from any of the other processors sharing neighbors without any constraint on the receiving order.

2.5 Effusion cooling

2.5.1 Technological and physical principles

Effusion cooling (which may be considered an extreme case of full-coverage film-cooling), consisting of an array of closely spaced discrete film-cooling holes, is a very powerful way to achieve modern low-NOx combustor liner cooling system requirements [116]. A significant reduction of the available air for cooling purposes needs to be faced to guarantee adequate air stream in the combustion chamber to maintain lean combustion levels. A thin layer of coolant is thus maintained on the combustor liner to isolate this component from the hot gases by means of a huge number of microholes uniformly distributed over the whole surface. Even if this solution does not guarantee the excellent wall protection achievable with 2-D slots film-cooling, the most interesting aspect is the significant effect of wall cooling due to the heat removed by the passage of coolant inside the holes [57]. In order to maximize such effect the tendency is to increase exchange area by means of reduced drilling diameter and increased hole angle, such parameters reach nowadays the technological limit of 0.8 mm and 17°. Benefits of the low angle configuration not only lie in the augmentation of exchange area but also in a delayed jet detachment improving the film effectiveness [52].

With this preamble, the importance of performing a conjugate analysis to evaluate the combined effect of the film protection and the heat sink in

the cooling ducts, is evident in order to provide a reliable estimate of metal working temperature [33].

The parameter that best represents such a global effect is the overall effectiveness, which can be easily computed from the wall temperature:

$$\eta_{ov} = \frac{T_{main} - T_{wall}}{T_{main} - T_{coolant}} \tag{2.11}$$

2.5.2 Investigated test cases

The numerical simulations to be shown in the following subsections were set up after a dual experimental investigation conducted within the EU Project Intellect D.M. [111]: a low temperature experiment as well as a high temperature one.

Experimental liners to carry out measurements of cooling performances of effusion systems usually comprise simple multiperforated flat plate with a constant pressure drop maintained across its thickness to guarantee the required coolant bias flow. Parallel flow can be superposed on both sides of the plate to guarantee the required blowing ratio.

Two different plates geometries have been investigated in this section. Having the same porosity and the same slanted injection of 17°, they differ in the shape of the holes. One uses conventional circular holes, the other shaped elliptical holes projecting a circular imprint on the plate. To maintain the same porosity both streamwise and spanwise pitch were changed maintaining the staggered array configuration. A sketch of the two geometries with dimensions from the cold rig plate is found in Fig. 2.2.

Flow conditions reproduce typical values for combustor liner effusion cooling, the selected conditions for the numerical investigation are $Re_j = 12500$ and BR = 3.5 and 5. Two separate computations have been performed in order to reproduce the different flow conditions of two experimental campaigns
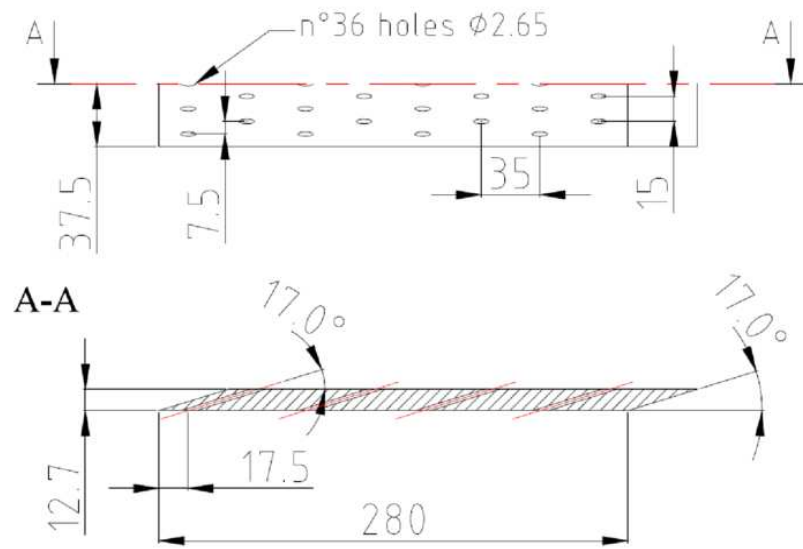
(a) Circular holes
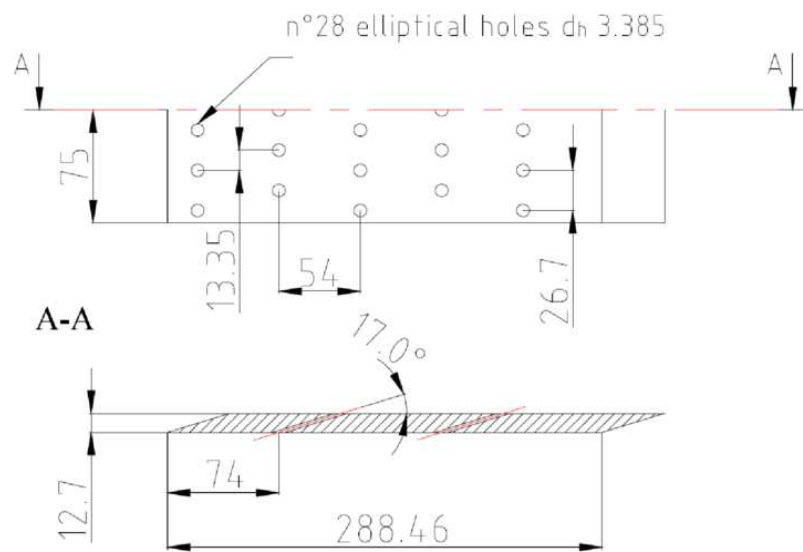
(b) Shaped holes

Figure 2.2: Sketch and dimension of the University of Florence plate.
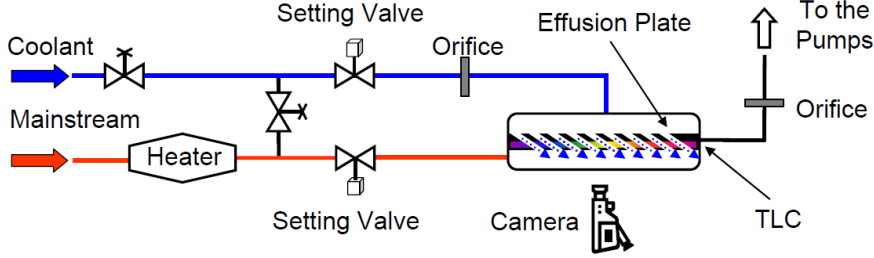
Figure 2.3: Sketch of cold rig at University of Florence

for which experimental values were available. The two set ups differ in the temperature difference between the coolant and the main flow, the scaling of the multiperforated plate, the coolant feeding system and the conductive property of the plate.

The first experiment was conducted on the "cold" rig at the University of Florence, see Fig. 2.3 where temperature distribution on the plate was measured by means of Liquid Crystal Thermography [52]. A detailed spatial resolution of the surface temperature was available permitting the computation of the overall effectiveness here reported in terms of spanwise averaged profiles. The low temperature difference of 10 °C between the coolant and the hot gas made the numerical computations of the effectiveness very challenging, and the experiments very sensitive to the liquid cristal activation band.

The second one was performed on the THAILE (THermal and Aerodynamic features of Experimental Liners) facility at the Laboratoire de Combustion et de Détonique, Poiters, France, [35]; a sketch of the rig set up is reported in Fig. 2.4. This high temperature rig can generate experimental conditions close to those encountered in the vicinity of combustor liners, in
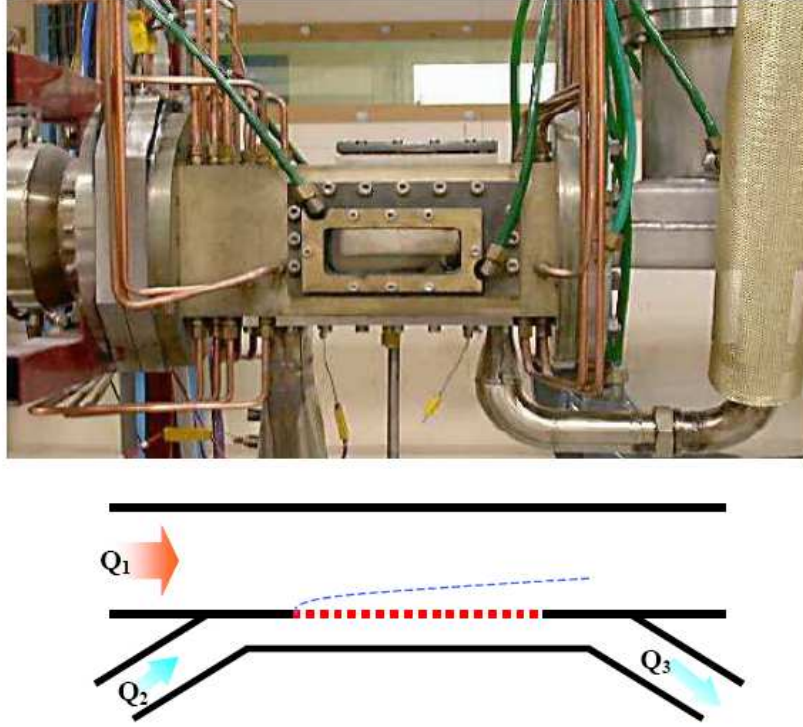
Figure 2.4: Sketch of THAILE hot rig

terms of gas velocity, temperature, pressure, and pressure drop across the liner. The multiperforated zone is instrumented with K-type thermocouples of diameter 0.5 mm, sheathed with stainless steel. These provide the wall temperature on the cold side of the plate.

2.5.3   Computational set up

Both the experimental plates presented in the previous section comprise a huge number of holes (36-28 for the University of Florence Rig, 569-234 for the THAILE Rig). Considering a minimal cost of $400 \cdot 10^3$ cells per hole the simulation of the entire rig would have been prohibitively expensive in terms of computational cost. With the aim of reducing up to an afford-

able level the complexity of the problem, a steady-state assumption was exploited for these computations. The gain for such assumption not only relies in avoiding constraints typical of time resolved solvers but, considering the spanwise repeatability of the plates and of the flow condition, also stands in the reduction of the computational domain. If no temporal variations are allowed in fact, the wake behind the injection holes can be separated into two halves, inserting symmetry conditions. A single pitch was thus discretized as demonstrated in Fig. 2.5 also to stabilize convergence towards steady state solution. Such a procedure was already successfully exploited to perform
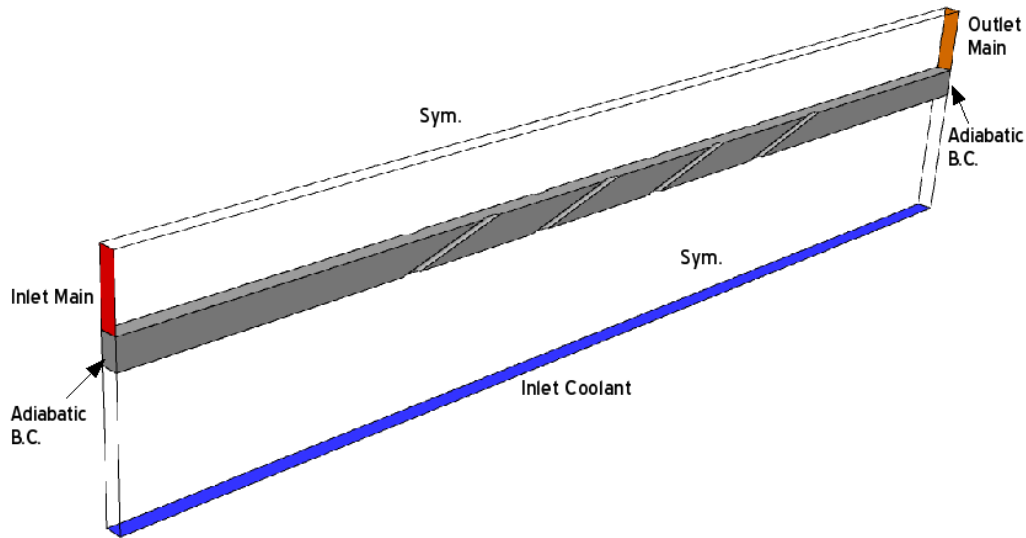
Figure 2.5: Overview of the computational domain

adiabatic computations on similar geometries in [13].

2.5.4   Computational grid

Two different meshes were generated to compute the conjugate heat transfer, one for the solid domain and the second for the fluid domain. The easier set of equations being solved and the absence of strong thermal gradients close

to the interface in the solid domain, permitted efforts to be focused on a good spatial resolution for the fluid domain. A simple tetrahedral mesh was thus chosen for the metal plate to simplify the gridding process especially in the proximity of the sharp and slant corner behind the hole. The only constraint for the solid domain was to maintain a similar element dimension on the interface as the fluid part to avoid unbalanced solid to fluid coupling.

On the fluid side instead the need to solve for wall heat transfer requires a fine discretization of the boundary layer maintaining wall orthogonality as high as possible. According to Acharya [5] and Habte and Yavuzkurt [58] however this is only one of the requirements for an adequate meshing for film cooling, the others being: a fine resolution especially at the inlet and outlet of the ducts, the absence of a grid interface, good quality of the elements and grid independence. A multiblock hexahedral approach was found to provide the best solution for all these requirements. Completely hexa-

(a) Side View (b) Hole Exit
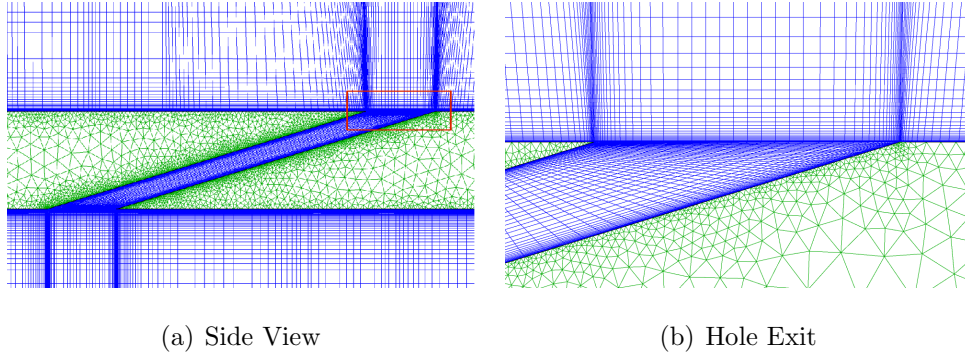
Figure 2.6: Overview and detail of the mesh around hole exit.

hedral multiblock meshes were preferred to purely unstructured tetrahedral meshes because of better performance of such elements in the free stream channels, in the plenums and inside the ducts. However both the need for an adequate reconstruction of the boundary layer on all the walls and the

very low injection angle represent a difficulty to work around with such a multiblock approach. In fact this approach leads to skew related deficiency around the sharp edges at 17°. The need to avoid grid interfaces at the same time excludes hybrid hexahedral-tetrahedral mesh as a feasible approach. The skewed elements were thus concentrated in the two zones near the inlet and the outlet of the ducts where a finer resolution could compensate for such a lack of mesh quality. An overview of the computational grid on the symmetry plane is reported in Fig.2.6.

Regarding the reconstruction of the boundary layer, it is conventionally assumed that to well integrate turbulent quantities up to the wall, y^+ should be kept below 1 and at least 25 elements should be positioned inside the boundary layer. However use of a Two Layer turbulence model, see Sec.2.5.5, allows less strict constraints especially in terms of number of elements in the boundary layer [82]. For both the conventional and the shaped geometry the near wall region is finely gridded obtaining on the walls an average $y^+ \approx 0.5$ also on the hole channels meaning that first node distance was pushed down to $y \approx 1 \mu m$. With the aim of correctly predicting the lateral development of the jet, it is also important to resolve well the space in which the gas and the coolant are coming one towards the other. Even though the two meshes are generated from the same block structure, the different imprints of the hole on the wall and the different pitch to diameter ratios lead to quite different meshes. A detail of the grid point distribution on the interface is shown in Fig. 2.7 for the conventional and the shaped case and for the solid domain. The total computational size of the resulting grids is 3.5 millions cells for the conventional case (3.0 for the computations of Florence test rig) and 3.4 millions in the shaped case.

Even though a real mesh sensitivity analysis was not possible on these
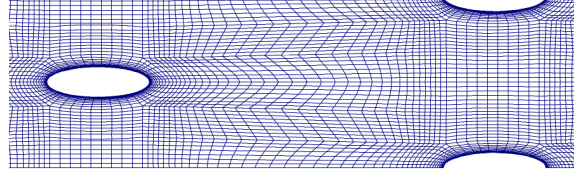
(a) Conventional geometry - fluid interface
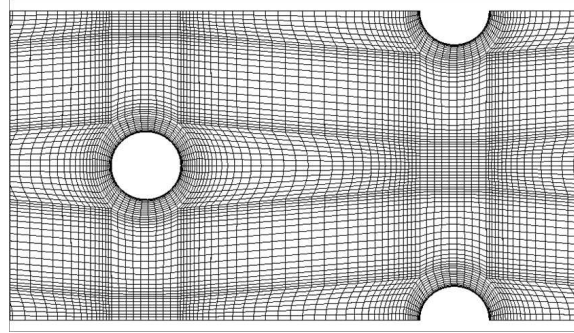
(b) Shaped geometry - fluid interface
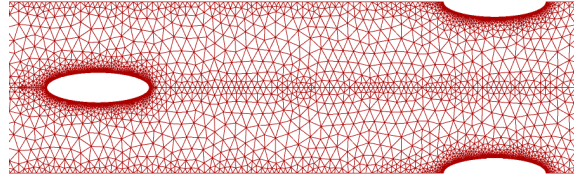
(c) Conventional geometry - solid interface

Figure 2.7: Detail of the mesh on the main channel wall.

setups due to computational limitations, such analysis has been conducted in the past for similar cases in order to obtain optimal meshing parameters used in this computation as well [15, 16].

2.5.5 Numerical methods

As already stated in the previous section, the steady-state assumption was exploited to perform this analysis. The in-house developed pressure corrector solver presented and validated in [93] was used. It exploits a SIMPLE-like

algorithm to cope with pressure velocity coupling extended to account for compressibility effects. Pressure corrector formulation allow an enhancement of convergence due to the use of more stable boundary conditions. Second order spatial discretization was achieved by means of a deferred approach.

AS a consequence of the steady state assumption, turbulence closure is achieved with RANS modeling. The choice of adequate turbulence models certainly represents a key factor for film and effusion cooling predictions. A known limitation of numerical predictions with respect to film cooling flows is the too low lateral diffusion of jets predicted by eddy-viscosity models [16]. For a jet in crossflow in fact the hypothesis of isotropic turbulence ceases to be applicable in the mixing zone. Both the normal to the wall and the streamwise directed fluctuations tend to deviate in the spanwise direction, enlarging the lateral diffusion as regards to the other two main directions. In order to go beyond this, Bergeles et al. [25] proposed to algebraically correct the main Reynolds stress, the product of the stream and span directed fluctuations, with an amplification function expressed in term of non dimensional wall distance. Solving for the same number of equations as the chosen eddy viscosity model, a viscosity tensor can thus be obtained. Even though this correction is not generally applicable to all flows it was proved to perform well in jet in crossflow on flat plate tests [16, 13].

Lakehal et al. [82] suggested the implementation of such a correction into the Two Layer model by Rodi [110]: an hybrid turbulence model between wall-resolved and wall-function models. Turbulent dissipation is not only imposed in the near wall cell but in a buffer layer covering the walls, hence permitting a more precise reconstruction of the boundary layer profiles. Both the isotropic (TL) and anisotropic (ATL) Two Layer models were studied in order to assess the gain obtained with the anisotropic correction over a model

that amongst the isotropic turbulence models is one of the best performing for effusion cooling tests [93].

2.5.6   University of Florence Rig

For this "cold" experiment only the conventional geometry was investigated since no particular influence of the shape was assessed by the experiments [133].

The actual dimensions of the investigated plate already shown in Fig. 2.2, are summarized in Table 2.1. The 36 holes are organized in a staggered

Table 2.1: Geometrical features

	D_h	α	L/D_h	S_x/D_h	S_y/D_h	$Holes$
	mm	deg				
$Conv$	2.650	17	16.39	13.21	5.66	36

array of 9 lines: the single pitch reduction leads to a domain including 8 hole halves.

For this computation the boundary conditions reported in Table 2.2 applies for the fluid domain.

The solid domain for the conjugate test is composed of a highly conductive alloy steel whose physical properties are shown in Table 2.3 and modelled as constant in the computation.

It is necessary to specify that the two sides of the solid plate, those corresponding respectively with the inlet and the outlet of the main flow, were considered adiabatic. Due to the fact that in experiments the metal plate was cut inclined at 17° parallel to the holes and was positioned much closer to the perforated zone of the plate, this assumption may lead to strong

Table 2.2: University of Florence boundary conditions

Inlet gas temperature	322.7	K
Inlet gas mass flow rate	0.00247	kg/s
Inlet gas turbulent kinetic energy - k	1.5	$\mathrm{m}^2/\mathrm{s}^2$
Inlet gas turbulent dissipation - ε	55.11	$\mathrm{m}^2/\mathrm{s}^3$
Inlet coolant temperature	312.6	K
Inlet coolant mass flow rate	0.00144	kg/s
Inlet coolant turbulent kinetic energy - k	$3.73e-5$	$\mathrm{m}^2/\mathrm{s}^2$
Inlet coolant turbulent dissipation - ε	$7.74e-5$	$\mathrm{m}^2/\mathrm{s}^3$
Outlet pressure	45130	Pa

Table 2.3: Solid domain characteristics.

Density	8.01	$\mathrm{kg/m}^3$
Specific heat capacity	473	kJ/(kg K)
Thermal conductivity	16	W/(m K)

disagreement between experiments and CFD predictions.

Results are presented in terms of wall overall effectiveness; first a map of the effectiveness distribution on the wall is discussed for the tested turbulence models, see Fig. 2.8, then the laterally averaged overall effectiveness is compared against experimental values, in Fig. 2.10.
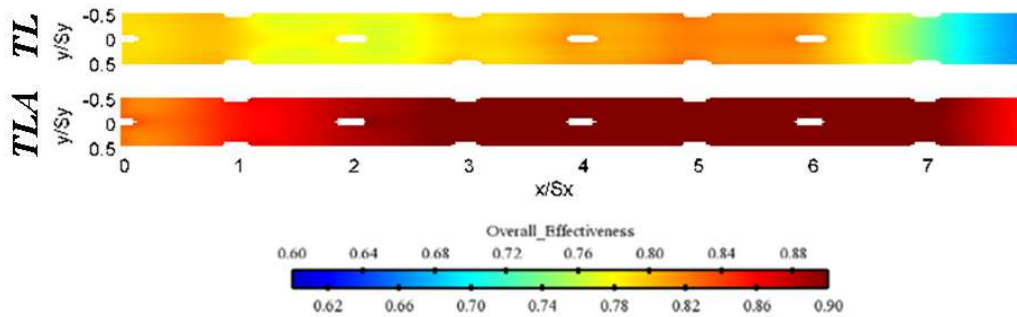
Figure 2.8: Overall Effectiveness Maps

Fig. 2.8 confirms the expected behaviour of the two turbulence models with the anisotropic Two Layer enhancing the lateral spreading of the jet thus augmenting lateral effectiveness. In such conjugate calculations the lateral distribution of temperature is much smoother than in adiabatic cases [8, 52] due to the high thermal conductivity of the metal plate. For the anisotropic calculation especially the isolines of effectiveness are almost oriented in the spanwise direction. Looking at the Two Layer map it is possible to notice the enhancement of metal temperature after the second row of holes corresponding to a lower effectiveness. This is due to the entrainment of hot gas below the cooling jets. The low pressure zone behind the penetrating jets is in fact drawing hot gas towards the wall as reported in the vector plot in Fig. 2.9. This effect is present in all jets but is more strongly noticed after the second row where the depression is already big enough to attract a consistent mass of the hot gas grazing the jets and the temperature of the gas sucked down is still not mitigated by the mixing with the coolant. This effect is present also in the adiabatic calculations, see [8], while is much less pronounced in the anisotropic turbulence model predictions due the lower coherence of the jet.

Fig. 2.10 reports the spanwise averaged profiles in comparison with the experiments. It clearly shows how the numerical predictions are overestimating the experiments for the overall effectiveness of the system. Unexpectedly the overall experimental curve is considerably decaying from the first up to the fifth row of holes. This behaviour can be explained with the effect of the metal plate border cut parallel to the hole ducts and in relative proximity of the first hole. The major portion of metal in contact with the coolant plenum may result in a strong increase of the cooling effectiveness upstream of the drilled part. The jet/cross flow interaction mechanism previously described

(a) Conjugate TL   (b) Conjugate TLA
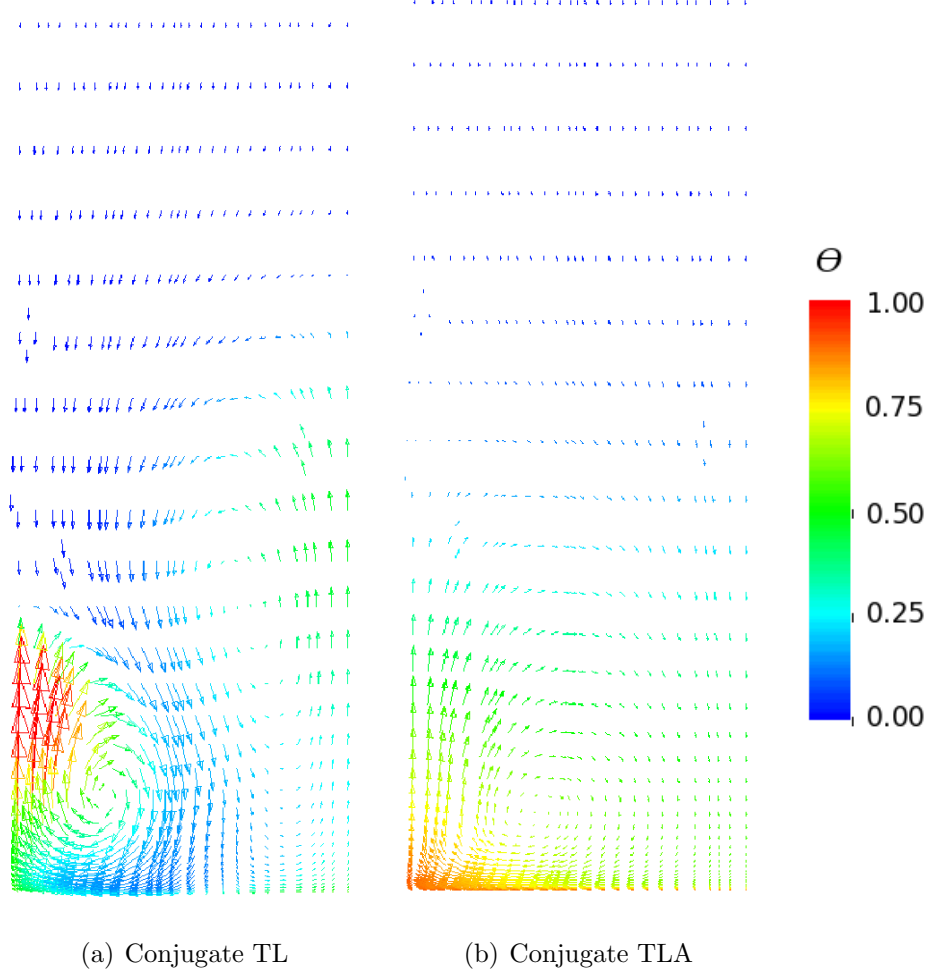
Figure 2.9: Span and normal wise directed velocity vector plot colored with dimensionless temperature 1-D downstream second hole.

might also play a role in decreasing the effectiveness for the second row of holes. This behaviour is only partially predicted by the Two Layer model whose effectiveness remains constant for first two rows approximately.

However even considering a lower overall effectiveness upstream of the first hole, the two numerical curves were expected to bound the experiments as for the adiabatic case. This shift of the curves towards higher values can be explained by a too strong heat sink effect predicted in the hole channels, in
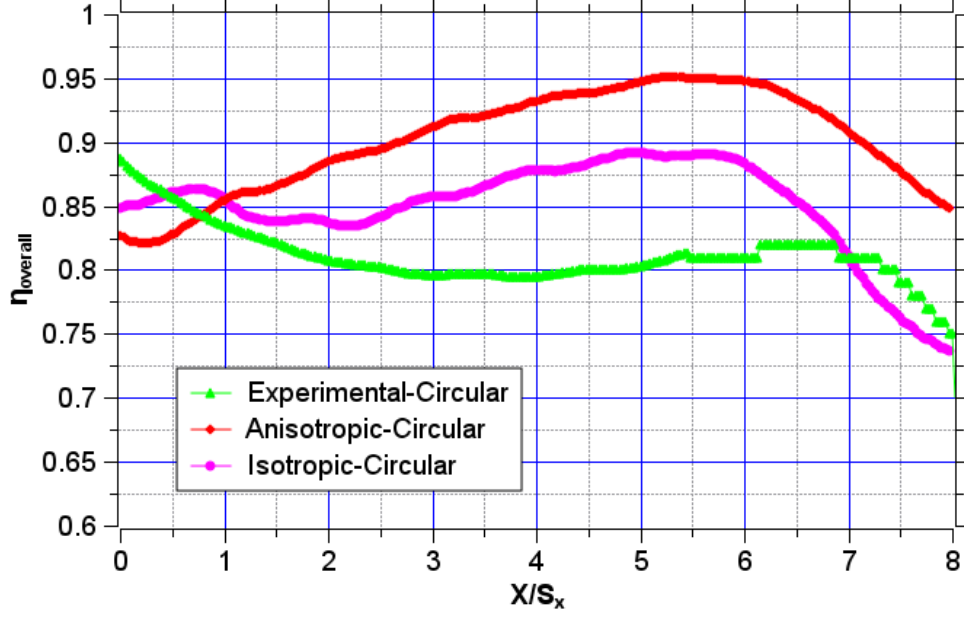
Figure 2.10: Spanwise averaged overall effectiveness.

fact the slope of the curve is constantly higher than in the experiments. This overprediction is related to an over estimation of the temperature decrease due to the strong acceleration in the channel (local Ma nearly 0.3) as shown in Fig. 2.11, such effect was already highlighted also for adiabatic simulations [8]. The main reasons for this failure relies in an approximation of the viscous heating terms and in the misalignment of the velocity vector and the face normals that splits the convective contributions. Obviously such numerical effect is promoted by slant hole angles, high velocity ratios as well as small hole diameters. The case in discussion results to be very critical for all these aspects providing a quite challenging test for numerical simulations.
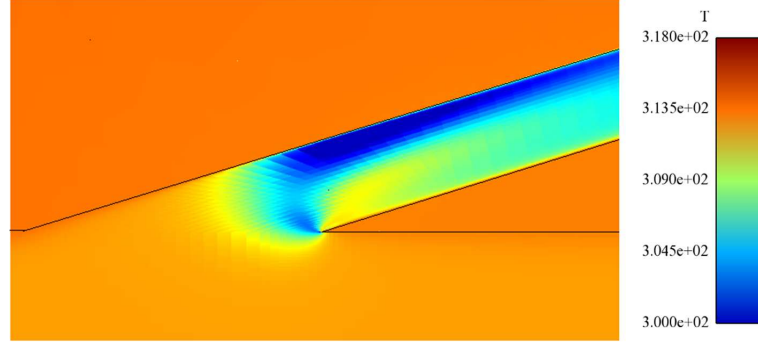
Figure 2.11: Temperature on symmetry plane at hole duct inlet.

2.5.7   THALIE Rig

As reported in the sketch in Fig. 2.12, the proportion of the rig are different from the one already presented in the previous section concerning the thickness of the plate, the dimensions of the channels and also the scaling of the perforated plate as reported in Table 2.4.

Table 2.4: Geometrical features

	D_h	α	L/D_h	S_x/S_y	t	$Holes$	$Rows$
	mm	deg			mm		
$Conv$	0.58	18.5	13.6	2.1	2.5	569	17
$Shaped$	0.76	17.3	11.1	2.0	2.5	234	12

The increased number of rows for this second rig forces us to introduce another simplification or better to neglect the effect of the last rows of holes: only the first 8 rows were included in the domain. Moreover a different feeding system for the coolant is employed guaranteeing an adequate crossflow on the coolant side as well. The computational set up is changed accordingly: the inlet for the cold gas is moved laterally and an outlet section is opened on the other side. In this manner however it is not possible to directly impose
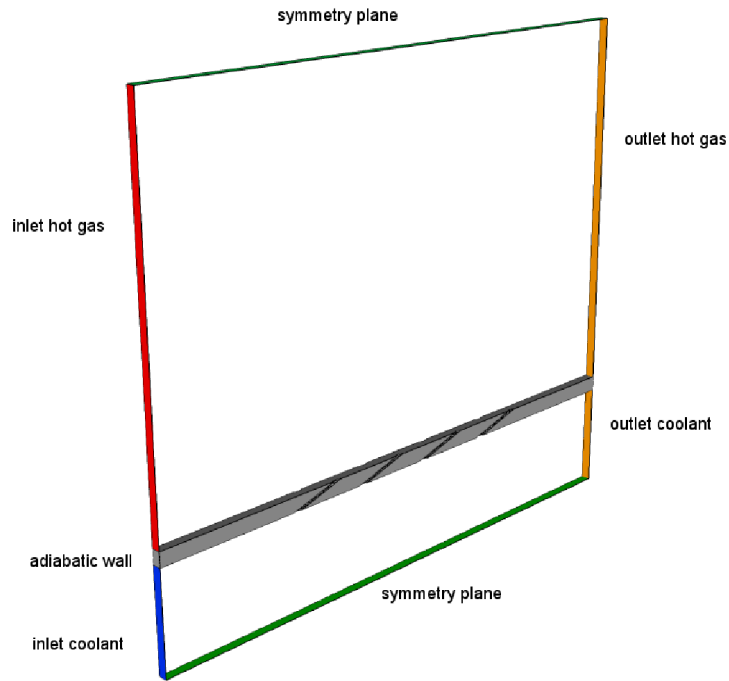
Figure 2.12: Overview of the computational domain for THAILE Rig.

the blowing ratio since the amount of gas leaving the coolant duct towards the hot side cannot be estimated *a priori* because it depends on the coolant outlet pressure. Furthermore the pressure drop in the stream direction may also lead to higher inhomogeneities in the local blowing ratio.

Due to the high temperature employed in the hot side, the plate was covered with low-conductive material functioning as a thermal barrier for the metal part of the plate. The conductivity of the solid part was changed consequently as pointed out in Fig. 2.13: a 5 mm thick layer with constant $k = 1.77 \, \text{W}/(\text{m K})$ and the rest of the plate with conductivity varying linearly with temperature following Eq. 2.12.

$$k = 0.02 \, T + 3.57 \,. \tag{2.12}$$

Boundary conditions applied also differ quite substantially from the cold
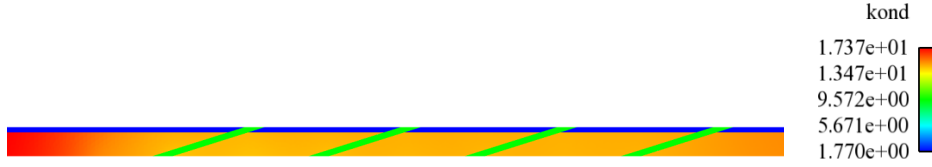
Figure 2.13: Thermal conductivity in the solid domain

case, Table 2.5 reports the data reproducing a BR of 3.6 for the circular holes and 3.3 for the shaped holes.

Table 2.5: THAILE rig boundary conditions

Inlet gas temperature	1000	K
Inlet gas mass flow rate	8.8	gs^{-1}
Inlet gas free turbulence	11.2	–
Inlet gas turbulent length scale	1	mm
Inlet coolant temperature	288	K
Inlet coolant mass flow rate	1.59	gs^{-1}
Inlet coolant free turbulence	0.1	–
Inlet coolant turbulent length scale	0.1	mm
Main outlet pressure	3.0	bar
Coolant outlet pressure	3.092	bar

Given that the thermal measurements are only available as thermocouple temperatures at selected streamwise positions no 2-dimensional maps are available, thus the results are presented in terms of spanwise averaged overall effectiveness in Figs. 2.14(a) and 2.14(b) for the circular and the shaped holes respectively. It can easily be noted how the predictions for the conventional holes strongly underpredict the overall effectiveness with respect to the experiments. On the other hand the predictions for the shaped geometry results to be pretty successful in matching the experimental curve.

The cause of the disagreement is related to the higher sink effect in the conventional geometry compared to the shaped one. Adiabatic investigations
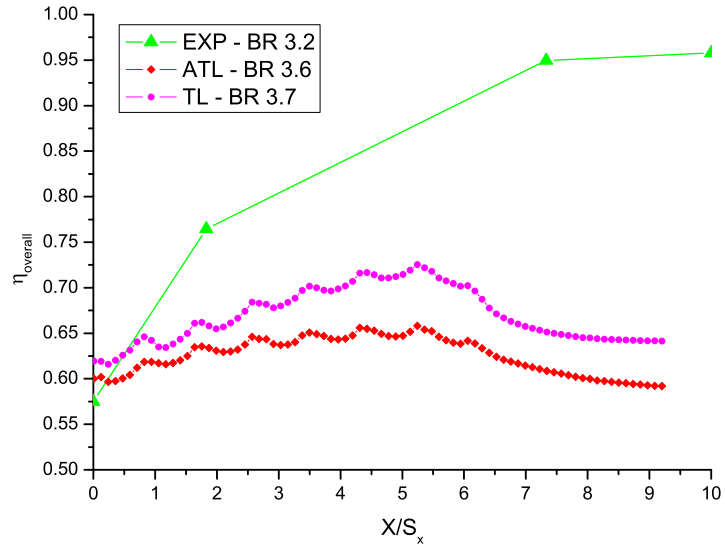
(a) Circular holes
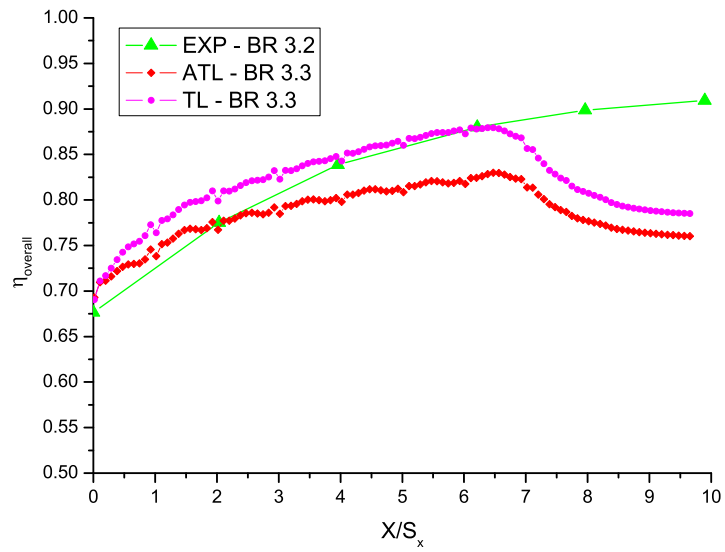
(b) Shaped holes

Figure 2.14: Spanwise averaged overall effectiveness.

[35] demonstrate that a higher adiabatic effectiveness for the shaped holes would actually result in a lower overall effectiveness this being related to the lower heat sink effect. Moreover the global heat sink effect, that would shift

plate effectiveness towards higher values, strongly depends on the number of holes included in the numerical domain. Both the computations included 8 rows of holes but for the former the actual number of rows in the experimental tests is 17 while for the latter it is only 12. The mean plate temperature is thus underpredicted in both computations but it definitely has a stronger impact on the circular hole computation, where the computational domain is shorter than in the second case.

The starting value of η_{ov} is well predicted by all computations, being mainly a function of the conductive equilibrium upstream of the first hole.

The effect of the turbulence model is quite evident: the anisotropic model predicts a lower cooling effectiveness. This is opposite to what was pointed out for the previous case in Sec. 2.5.6. Two contrasting effects are predicted by the anisotropic model: an enhancement of the adiabatic effectiveness as well as an increase of the heat transfer coefficient [8]. In this latter case, where the temperature difference is maximum, the second effect is stronger leading to a higher interface temperature.

2.6   Concluding remarks

The developed interface for conjugate heat transfer calculations proved to be accurate and energy preserving (no heat losses across the interface) for the theoretical cases used for validation purposes. Such a boundary condition was applied also to the study of more realistic test cases, namely the overall effectiveness of multiperforated plates with effusion. Two different geometries corresponding to conventional and elliptically shaped holes manufactured to represent nowadays technological limits in terms of inclination angle (17°) and hole diameter (0.8 mm) were tested.

The results obtained underline how the inclusion of the heat sink effect substantially affect the thermal distribution inside the metal sheet. They also show how predictions are highly dependent on the heat exchange far from the holes as well and thus in order to correctly reproduce experiments the thermal conditions on the plate sides should be set up carefully.

Chapter 3

Mapped inlet conditions

Contents

This chapter deals with the algorithms implemented for the generation of turbulent inlet conditions. In particular a recycling method exploiting internally developed turbulent fields to provide turbulent coherent structures is proposed. The various techniques used to impose control on the generated profiles are also introduced. Application to an axisymmetric impingement

jet with heat transfer is used to assess the capability of such an approach for combustor cooling analysis.

3.1   Auto recycling inlets

In Sec. 1.6 the impact of a correct reproduction of the turbulent flow on the inlet boundary was examined going through several possible approaches among which the auto recycling method was considered as one of the most promising. The main idea for such a boundary condition is to incorporate into the computational domain a fictitious extrusion used to generate turbulence inside the original domain, in practice by incorporating the recycling methods into a single computational domain [129].

The procedure consists in identifying a plane (the theoretical procedure can be applied to generally curved surfaces but the current implementation is restricted to planar inlets) intersecting the domain where flow conditions similar to those at the inlet surface apply, e.g. in Fig. 3.1 the plane positioning as suggested by DeVilliers for noise sources evaluation in an external aerodynamic case [45]. If such a plane does not exist it is often possible to extrude the domain upstream of the inlet section to establish the conditions for applicability. Not only flow conditions must be similar but the cutting plane geometry should precisely correspond to the inlet boundary too. Notice that it is only required that the overall geometries coincide at the borders while the internal mesh discretization may be different in the two sections even though a similar dimensioning is suggested to maintain the same level of accuracy of the generated turbulence.

The mapping plane should be positioned not too close to the inlet, to guarantee sufficient space to generate coherent structures, the recycling pro-
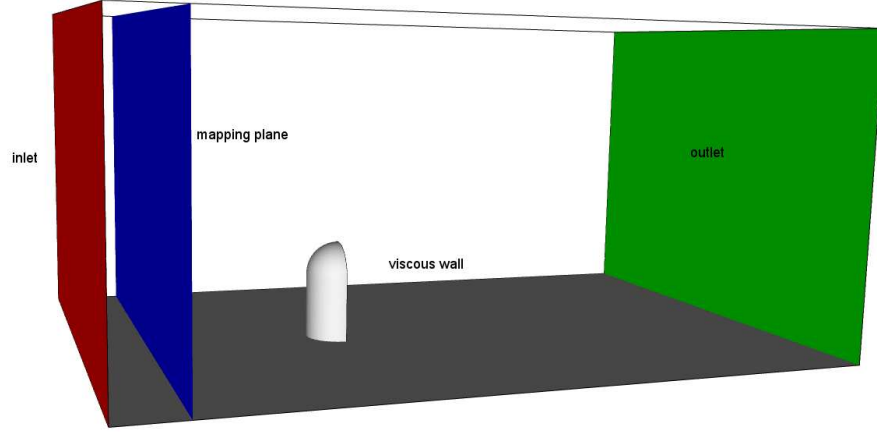
Figure 3.1: Example of mapping plane positioning

cess will generate artificial modes in the solution which may be significant. At the same time augmenting the distance may well extend the computational domain increasing the total computational cost.

Once the plane is identified, an artificial 2-dimensional grid is constructed exploiting the intersection points between the plane and the real 3D grid. A sampling procedure is then implemented to probe the internal values $\psi_{internal}$ of the real mesh on the gridded plane ψ_p at each new iteration. To map the sampled values back on the inlet surface first the gridded plane is moved to overlap the inlet boundary hence a conservative interpolation is defined to reconstruct the profiles on the inflow grid, see Eq. 3.1.

$$\psi_{map} = \sum_p \alpha_p \cdot \psi_p \tag{3.1}$$

Parallelization is achieved reconstructing at the first iteration the global grid on the sampling plane collecting the cutting points from each processor.

Values at the face centroid are then updated iteration by iteration, sent and received by every processor owning at least one inlet face or one cutting plane face.

3.2 Feedback control

The above mentioned direct mapping is totally driven by the flow itself, and thus is prone to diverge from the required flow conditions $\tilde{\psi}$ to be investigated. What is needed by such a boundary condition is in fact to correctly reproduce turbulent behaviour but also to maintain specific averaged inflow conditions, i.e. mass flow rate, mean temperature, turbulence level. To guarantee that the boundary does not introduce any drift from the specified values, a feedback mechanism is introduced to satisfy the physical condition to be imposed. A scaling, S, of the mapped fields is hence applied to correct the mapped values as suggested in Eq. 3.2:

$$\psi_{inlet} = S \cdot \psi_{map} \, , \tag{3.2}$$

with

$$S = \frac{\tilde{\psi}}{\overline{\psi}_{map}}. \tag{3.3}$$

To obtain the scale that precisely matches the desired inflow conditions two different averaging techniques can be specified to calculate $\overline{\psi}_{map}$, the first one fixing the surface averaged value, see Eq. 3.4, and the second one weighting ψ on the convective fluxes ϕ, in Eq.3.5:

$$\overline{\psi}_{map} = \frac{\int_A \psi_{map} dA}{\int_A dA} \tag{3.4}$$

or

$$\overline{\psi}_{map} = \frac{\int_A \psi_{map} \phi \, dA}{\int_A \phi \, dA} \, . \tag{3.5}$$

Exploiting these procedures requires that ψ_{inlet} either respects:

$$\frac{\int_A \psi_{map} dA}{\int_A dA} = \tilde{\psi} \, , \tag{3.6}$$

or

$$\frac{\int_A \psi_{inlet}\phi \ dA}{\int_A \phi \ dA} = \tilde{\psi} \, . \tag{3.7}$$

In practice such a procedure corresponds to imposing the integral inlet fluctuations at zero, this additional constraint, even though artificially damping the fluctuations, it is usually weak enough to allow the triggering of coherent turbulent structures.

In general for a transported scalar it is suggested that one should maintain the mass flow averaged value constant rather than the area averaged value. For the velocity however the use of convective flux weighting imposes a fixed momentum flux while the mass flow rate is free to fluctuate and drift from the specified values. Since the mass flow rate is definitely a more tangible global parameter defining the working Reynolds number, it is preferable to use the area averaged value.

3.3   Mapped fluctuations

The feedback control permits the integral inlet quantities to be fixed to prescribed mean values, however there is no way of adapting the obtained fields to desired profiles. The mean profile resulting from the feedback mechanism described in the previous section may result, especially in case of an inaccurate choice of the plane position, in artificially produced profiles or too long a transient time to reach statistically steady state solution. If indeed the desired mean profile ψ_d is known from available measurements or lower order numerical analysis such as steady-state RANS computations or correlative

analysis, it is possible to apply the already presented mapping technique
to the unsteady fluctuations. These mapped fluctuations superposed to the
assigned mean profile permit instantaneous inlet values to be specified. In
other words Eq. 3.8 is used to create the distribution of mapped fluctuations:

$$\psi'_{map} = \sum_p \alpha_p \cdot \psi'_p = \sum_p \alpha_p \cdot (\psi_p - \overline{\psi_p}) \,, \tag{3.8}$$

then the unsteady turbulent field is reconstructed as in Eq. 3.9:

$$\psi_{inlet} = \psi_d + \psi'_{map} \,. \tag{3.9}$$

As in the previous case, attention should be posed on the initialization
procedure. If the mean field is not stabilized, i.e. $\dfrac{\partial \overline{\psi_p}}{\partial t} \neq 0$, too high fluctu-
ations might be introduced since all transient development of the flow field
would be included in the fluctuating part. Vice versa if the initialization
solution is not sufficiently perturbed no fluctuations would be introduced at
the inlet thus the turbulence inlet level might be strongly mispredicted.

3.4   Impingement jet

Among the many different combustor cooling devices, the free impingement
round jet scheme offers a proper environment for the investigation of the
proposed boundary conditions: it is a well known and extensively studied
phenomenon with both experimental and numerical data available for the
validation process; it is also a quite challenging test case to obtain successful
computations. Since coolant is usually fed by means of almost stagnating
plenum or with long pipes, the effective use of these types of boundary con-
ditions would substantially decrease the complexity of the problem. At the
same time it also offers a problem of reduced complexity, allowing properly

resolved Large Eddy Simulations to be used at a reasonable computational cost. This is a key factor for testing such boundary conditions whose effectiveness is related to the amount of turbulent scales directly resolved.

3.4.1 Technological and physical principles

The use of impingement jets for the cooling of various regions of modern gas turbines is widespread, most especially within the hot stationary components. Since the cooling performance of impingement jets is very high, this method provides an efficient means of component heat load management where sufficient pressure head and geometrical characteristics are available for implementation. Regular arrays of impingement jets are commonly used within turbine airfoils and endwalls to provide relatively uniform and controlled cooling of fairly open internal surface regions [126].

Even though generally employed in regular arrays with confinement generating lateral crossflow, the detailed study of the single impingement jet has also been matter of investigation for many researches both experimentally [18, 92, 99] (a useful review is found in [78]) and numerically [12, 60, 136].

The impinging jet can be defined as a high-velocity coolant mass ejected from a hole or slot that impinges on the heat transfer surface (Fig. 3.2 shows a sketch with common nomenclature). A characteristic feature of this arrangement is an intensive heat transfer rate between the wall and the fluid corresponding to the hole imprint on the plate and a subsequent radial decay. In gas turbines cooling devices impingements are usually employed in a submerged configuration characterized by the same fluid stagnating in the gap in between the impingement and the confinement wall, as opposed to a free impingement scheme where two different fluids are in use.

The typical flow structures developing around the impingement jet are
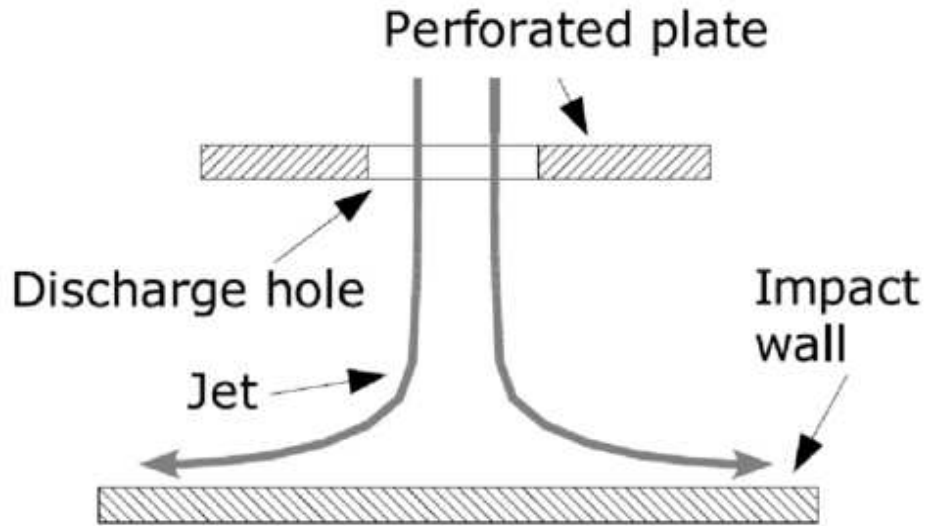
Figure 3.2: Single jet impingement scheme

usually classified in three different zones as depicted in Fig.3.3:

- Free jet zone

- Impingement (or stagnation) zone

- Radial wall jet

In the free jet zone the coolant develops in a similar manner to a submerged non impinging jet: a potential core region ($\xi/D \approx 4 - 5$) is followed by a flow development region ($\xi/D \approx 5 - 8$) and finally flow becomes fully developed ($\xi/D > 8$). In most impingement applications, including the investigated one, the plate is not positioned far enough away to permit either the development or the fully developed region to appear. In the potential core region a shear layer forms corresponding to the nozzle lip. In the proximity of the lip itself the shear layer is so thin compared to the jet diameter
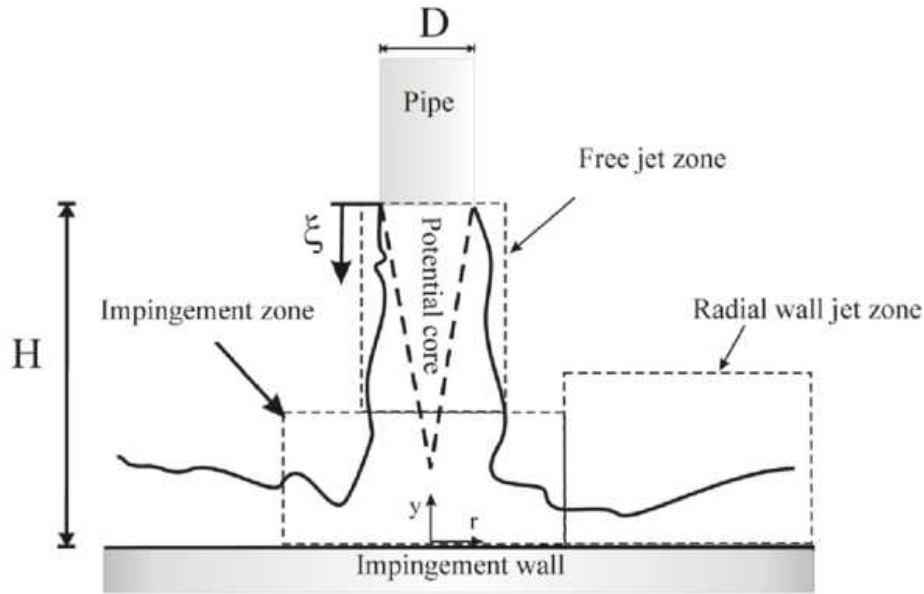
Figure 3.3: Schematic of a jet impingement flow structure (from Uddin [134])

that the Kelvin-Helmholtz instability mechanism typical of plane shear layers develops, generating the so called ring vortices [59, 134].

As the jet approaches the wall, a counter pressure gradient arises slowing and turning the flow towards the radial direction. A relaminarization of the flow occurs near the stagnation point due to negative turbulence production as pointed out by experiments and LES predictions [43, 99]. The increase in velocity along the wall keeps the boundary layer thin, and consequently, the heat transfer rates are high.

The wall jet zone is characterized by the absence of mean pressure gradients. Laminar to turbulent transition occur and even though the flow is parallel to the wall, turbulence levels are higher than in the free jet shear layer. The flow is then free to decelerate as the blowing section is enlarging due to the radial increase.
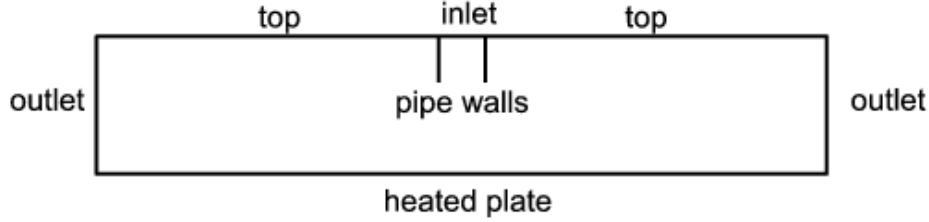
Figure 3.4: Schematic of the jet impingement computational domain

3.4.2   Investigated test case

The investigated test case is the single round jet normally impinging onto a heated flat plate described in [1], the same scheme depicted in Fig. 3.3 applies. Detailed flow field experiments by Cooper [42] as well as heat transfer data by Baughn [19] are available to validate the procedure.

The $Re_j = 23000$ test at $H/D = 2$ was chosen with D = 26.5 mm. The feeding pipe is sufficiently long to provide fully developed flow conditions at the outlet section of the pipe itself and no confinement wall is present to guide the radial flow discharge. Following suggestions proposed by Uddin [134], the plate is considered uniformly heated with a constant heat flux of 1000 W/(m² K) and cooled by a fluid stream at 293 K. The reference outlet pressure is maintained at ambient pressure.

3.4.3   Computational set up and boundary conditions

The computational domain is quite simple for this test case as depicted in Fig. 3.4, nonetheless several choices need to be specified and justified.

First of all the decision to radially extend the domain up to r/D = 8 was driven by the necessity to avoid any outflow boundary effect on the core flow field and the consideration that experimental data was available up to r/D =

5. The advective boundary conditions defined by the hyperbolic convective equation in Eq. 3.10 and already described also in Sec. 1.7.2 is used in order to minimize reflection of flow perturbation, at the outlet.

$$\frac{\partial U}{\partial t} + C_{ref}\frac{\partial U}{\partial n} = 0 \tag{3.10}$$

The C_{ref} value was estimated, as proposed in [61, 134], exploiting a global mass flow balance between inlet and outlet boundary:

$$\int_{outlet} C_{ref} \cdot dA = \int_{inlet} U \cdot dA . \tag{3.11}$$

This condition not only applies to the velocity field but also to the energy equation, where the same reference velocity is employed. The same type of condition is also used for the relative pressure equation in a relaxed form similar to that described in Sec.4.1.4, see Eq.3.12, to avoid significant drifts from the reference value $p_\infty = 101325 Pa$.

$$\frac{\partial p}{\partial t} + C_{ref}\frac{\partial p}{\partial n} = -K(p_{ref} - p_\infty) \tag{3.12}$$

with K estimated from Eq.3.13:

$$K = \frac{U}{L_\infty} . \tag{3.13}$$

It is convenient to express the relaxation coefficient with such an expression because it offers a relationship with flow parameters: U is some kind of flow characteristic velocity, generally equal to C_{ref}, while L_∞ represents the distance from the boundary where pressure might be considered unaffected by internal domain unsteadiness, 1 m in this case.

Since the jet experiment was unconfined, no wall was sited opposite to the heated surface. The domain is bounded by the top surface in Fig. 3.4 located a distance 1D above the level of the exit of the pipe. The treatment of

such a boundary for which no superposed flow can be specified either in the inflow or in the outflow direction may result in problematic behaviours. Non reflective behaviour is required but it is not easy to specify such a condition in the case of unknown convective flux direction. An assessment analysis [61] on three different boundary conditions such as advective, inflow and pressure specified, showed a high dependency of the streamline pattern in the far plate region but no influence inside the jet. In this work a convective boundary was employed with a specified velocity:

$$C_{ref} = 1\% \cdot \frac{\int_{inlet} U \cdot dA}{\int_{inlet} dA} \tag{3.14}$$

No information was available about the thickness of the pipe, such dimension was therefore neglected and the two sides of the pipe were taken as coincident.

As introduced in the previous section, the pipe should be extended enough to guarantee fully developed flow. This would have been a quite costly requirement in terms of computational cost, to eliminate any entrance effects, according to the available correlations in Eqs. 3.15 and 3.16, the domain should have been extruded around 20 diameters.

$$L_e = 4.4 \cdot Re^{\frac{1}{6}} , \tag{3.15}$$

or

$$L_e = 1.6 \cdot Re^{0.25} . \tag{3.16}$$

In order to test the functioning of the implemented boundary condition a significant reduction of the duct length was introduced to overstress the effects of the inlet turbulence generation. The inlet was set only 1D upstream of the pipe exit and following a classical scheme for subsonic flow velocity, temperature and turbulence level were specified as reported in Table 3.1.

Table 3.1: Ercoftac impingement inlet conditions

Inlet velocity	13.15	m/s
Inlet temperature	293	K
Inlet turbulent kinetic energy - k	0.64	m^2/s^2

The pure mapped condition, see Sec. 3.2, was explored together with the mapped fluctuation condition exploiting profiles obtained from a separate computation of pipe flow. The profiles used were obtained by averaging both in time and tangentially the solution of a periodic circular pipe flow under equivalent mass flow conditions. For this auxiliary computation circumfer-
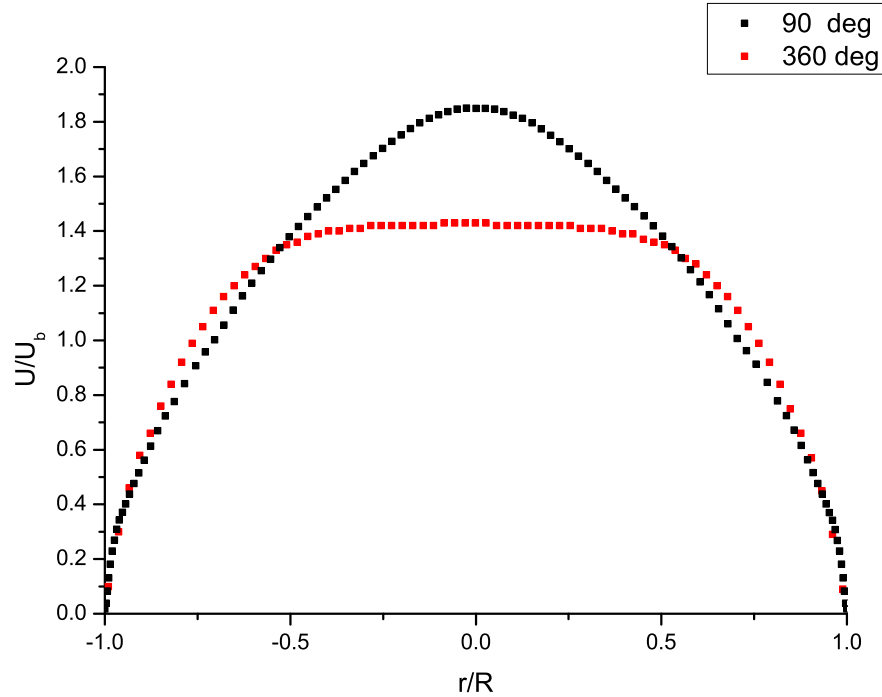
Figure 3.5: Reference inlet velocity profile from periodic pipe flow

ential periodicity of the solution is assumed to reduce the domain to a 90° sector of the pipe. Rotational cyclic boundary conditions are exploited to

couple the two sides of the quarter pipe domain. The obtained radial distribution of normal velocity, shown in Fig. 3.5, is almost as parabolic as a laminar profile.

A subsequent simulation of the same pipe configuration with a full 360° tangential development, showed a much flatter profile indicating that the tangentially cyclic conditions damped the fluctuations so much that an almost laminar profile is obtained.

3.4.4   Computational grid

Due to the relatively simple geometry a multi-block hexaedral meshing strategy was employed. Since no smoothing algorithm was employed quasi cartesian meshes were generated, whilst high orthogonality and low skew is guaranteed also in the proximity of the pipe edge.

Several meshes were employed and tested, including sectors of $90°, 120°$ and $360°$ as well as tangentially periodic meshes with degenerate hexaedra corresponding to the cylinder axis, before reaching the optimal configuration. For the sake of brevity only the optimal configuration will be discussed and described.

An O-grid structure with a fine wall clustering is used for the pipe as demonstrated in Fig. 3.6. The entire $360°$ angle is subdivided into 8 blocks, giving a total number of 84 blocks employed. 5.2 million cells were used to guarantee sufficient near wall clustering. It is out of question to fulfil the suggested requirements for wall resolved LES [105] in the entire domain in case the total number of elements needs to be maintained below $20 \cdot 10^6$. In fact an attempt to respect such constraints requires a 6 million cells mesh on a quarter of the full three dimensional domain [61]. Obviously the focus is on the stagnation and the wall jet zone up to $x/D = 5$ where y^+ is maintained
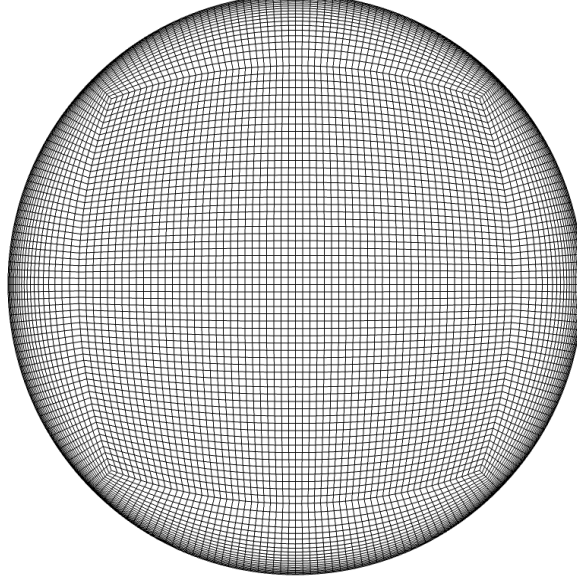
Figure 3.6: Inlet mesh

below 0.8. The stream and spanwise spacing in the impinging region are of equivalent size, in viscous units $x^+_{max} = z^+_{max} < 40$. Concerning the wall jet zone, the radial spacing is maintained confined $r^+_{max} < 200$ a value aligned with the required value of 150. The tangential spacing is conversely strongly increasing with the radius, resulting in a poor resolution compared to the desired $\theta^+ < 40$.

A post processing analysis demonstrated that the internal mesh resolution was sufficient to resolve directly up to the 80% of the total turbulent kinetic energy in most of the jet column and the wall jet. However the resolution strongly decays outside the jet zone due to the mesh coarsening. Fig. 3.7 shows the distribution of the modeled to resolved turbulent kinetic energy on a radial section. The level of modeled kinetic energy imposed at the inlet of the pipe is clearly too high as highlighted by the decay of this ratio inside the pipe itself. Moreover the ratio between the filter width $\Delta = V^{1/3}$ and the
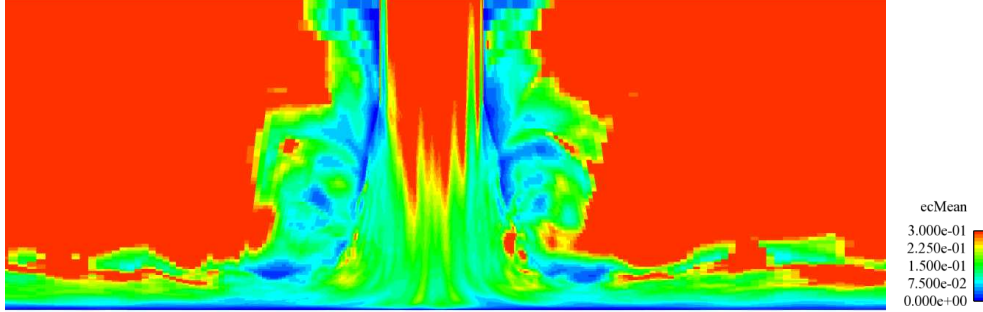
Figure 3.7: Modeled to resolved turbulent kinetic energy ratio

Kolmogorov length scale, estimated from the sub-grid model $\eta = \left(\dfrac{\nu_{SGS}^3}{\varepsilon} \right)^{0.25}$ with $\varepsilon = c_e \dfrac{k^{\frac{3}{2}}}{\Delta}$, showed to be less than 10 in most of the domain as well.

3.4.5 Numerical methods

The calculations were performed using a time resolved incompressible PISO loop solver. Large Eddy Simulation in OpenFOAM® uses the limited linear convective scheme and the implicit backward Euler time integration scheme. Preliminary investigations showed very weak dependency on the inclusion of density variation (thus an incompressible formulation as [59, 134]) and on the use of other second order bounded convective schemes.

Even though for properly resolved LES the sub-grid model is of little influence [53], a one-equation model proposed by Yoshizawa [142] and Menon et al. [97] was chosen. Such model is based on a transport equation for the sub-grid turbulent kinetic energy to better predict non equilibrium zones. The model is briefly reported in Eqs. 3.17 and 3.18.

$$\frac{\partial k}{\partial t} + \frac{\partial (U_i k)}{\partial x_i} - \frac{\partial}{\partial x_i} \left(\left(\nu + \frac{\nu_{SGS}}{\sigma_k} \right) \frac{\partial k}{\partial x_i} \right) = \nu_{SGS} \| S \|^2 - \frac{c_e k^{\frac{3}{2}}}{\Delta} \; ; \quad (3.17)$$

$$\nu_{SGS} = c_k \sqrt{k} \Delta \; . \tag{3.18}$$

The dynamic procedure was used to establish correct values for turbulence constants [54].

The purely incompressible PISO loop does not include any energy balance: a decoupled equation for static temperature was added to describe the heat transfer process with no feedback on the flow field. Sub-grid turbulent heat flux is modeled by means of a turbulent Prandtl number equal to 0.9.

The fluid is air at standard conditions treated as perfect gas with constant thermophysical properties. The duration of the simulation was estimated from the natural frequency of the jet, estimated from the Strouhal number St=0.64 predicted by [60] to be 317 Hz. Eight cycles were considered a sufficient time to develop statistically steady state conditions starting from an already developed solution mapped from a coarser mesh. Subsequent to this, time averaging was applied over a subsequent time period of 16 cycles, for a total averaging time period of 0.076 s.

3.4.6 Results

The results are presented in terms of velocity profiles in the impinging zone, the wall jet development is then checked by reporting mean velocity distributions at three radii up to r/D = 3. Effective axial, radial and cross turbulent fluctuations are also sampled along the radius. The radial distribution of Nusselt number is finally presented to assess the heat transfer. Time and tangential averages are applied to obtain more statistically significant profiles. Data from the two computations are compared with available experiments; discussion on the captured flow structures as well as on computational failures is conducted at the same time.

3.4.6.1   Flow field analysis

An overview of the instantaneous flow field is given on a radial section in Fig3.8 with the aim of describing the main characteristics of the impinging jet as already presented in Sec.3.4.1. The three proposed regions can be

(a) Mapped inlet

(c) Mapped fluctuation inlet
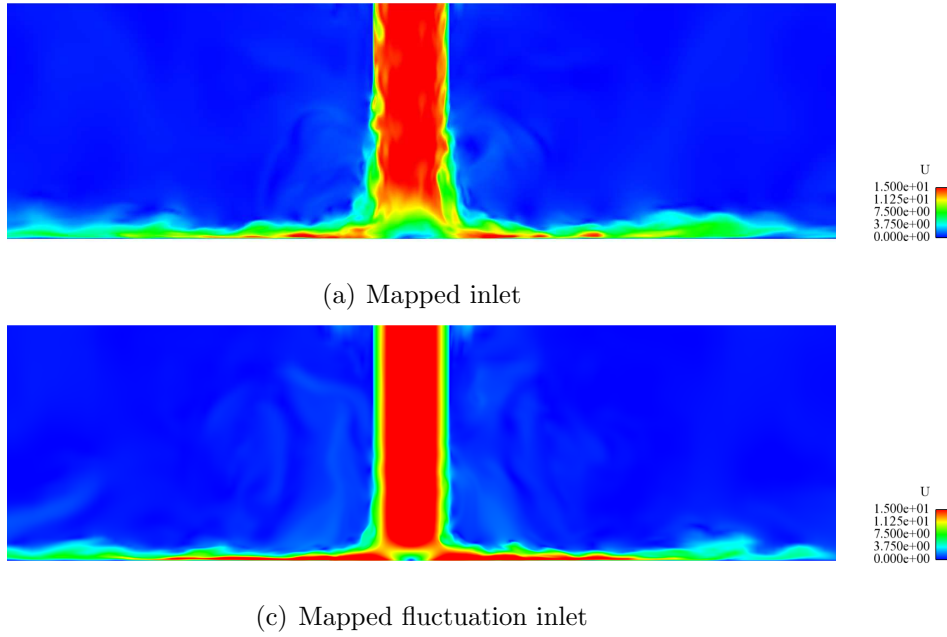
Figure 3.8: Instantaneous velocity magnitude in the symmetry plane.

easily identified in both the computations. The mapped fluctuation shows a more coherent free jet, confining the stagnation zone quite close to the wall. As a consequence also the wall jet is thinner and faster. However in order to provide a more useful insight on the flow field, several profiles were extracted every D/2 for 0⩽r/D⩽3.

In the impinging zone two profiles were extracted: the first one along the pipe axis, the second corresponding to the pipe lip imprint.

The centerline behaviour is plotted in Fig. 3.9(a) up to $y/D = 0.4$, i.e. a fifth of the entire pipe to wall distance to clarify. The experiments mea-

sured an almost linear profile connecting the no slip condition at the wall with values approaching the bulk velocity ($U_{Mean}/U_b = 0.9$) at y/D = 0.38. The mapped condition is able to correctly reproduce this profile, while the mapped fluctuation computation strongly overestimates the core jet velocity (U_{Mean} above 1.6 U_b) due to the too high peak velocity in the reference profile already noted in Sec. 3.1.

At r/D = 0.5, see Fig. 3.9(b), experiments and the mapped simulation shows a flat profile at around $U_{Mean}/U_b = 0.7$. Such a flat profile is related to the uniform distribution obtained at the inlet section, in fact the streamlines closer to the wall are those one from the centerline of the pipe. The higher centerline mass flow predicted by the mapped fluctuation is in fact causing a much higher peak in the boundary layer and a consequent underestimation of the velocity for y/D > 0.2.

Entering the wall jet region, as shown in Fig. 3.10, the situation remains unchanged with the mapped simulation exhibiting a smoother behaviour well aligned with the experimental evidence and the mapped fluctuation predicting a much flatter flow field towards the impinging wall. A certain tendency to develop higher velocity wall jet is noticed in the mapped simulation too, as highlighted by Fig. 3.10(c). The cause of such a lower deceleration in the radial direction and diffusion in the far field velocity is investigated in the too low radial and tangential mesh resolution, in the effect of the outlet boundary condition and in a possible effect of the initial transient flow development due to an insufficient averaging time. The time needed to achieve a statistically significant average is in fact dependent upon the flow through time and the path line integral time, thus it is higher at the highest radii. The time simulated represents more than 10 passes inside the pipe, but only around 4 recycles up to r/D =1.5; at r/D=3 this value becomes around 1.
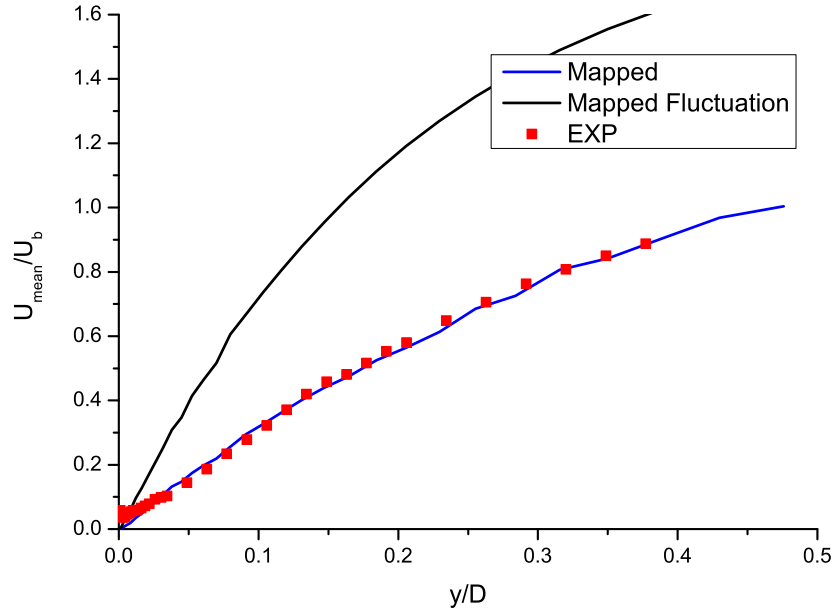
(a) $R/D = 0$
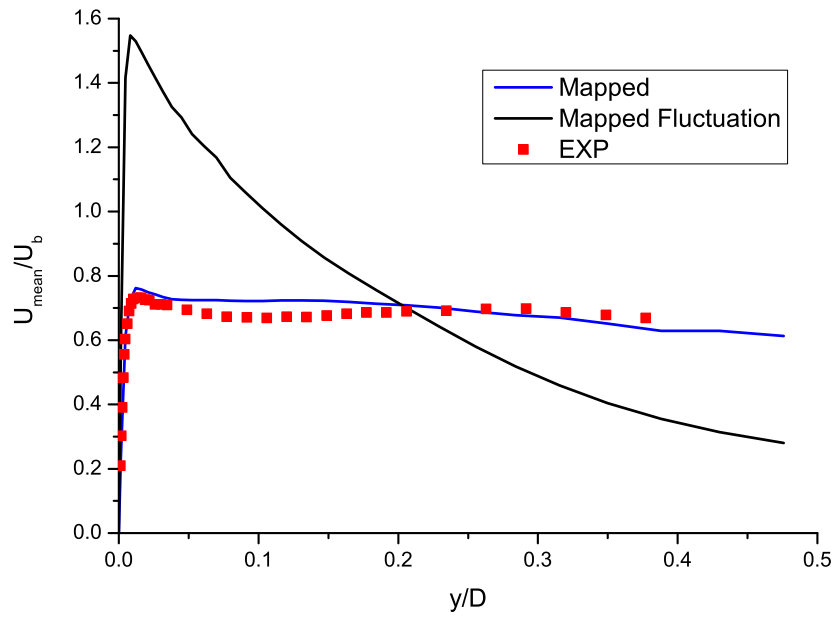
(b) $R/D = 0.5$

Figure 3.9: Mean velocity magnitude normal profiles - Stagnation zone.

(a) $r/D = 1$ (b) $r/D = 2$

(c) $r/D = 3$
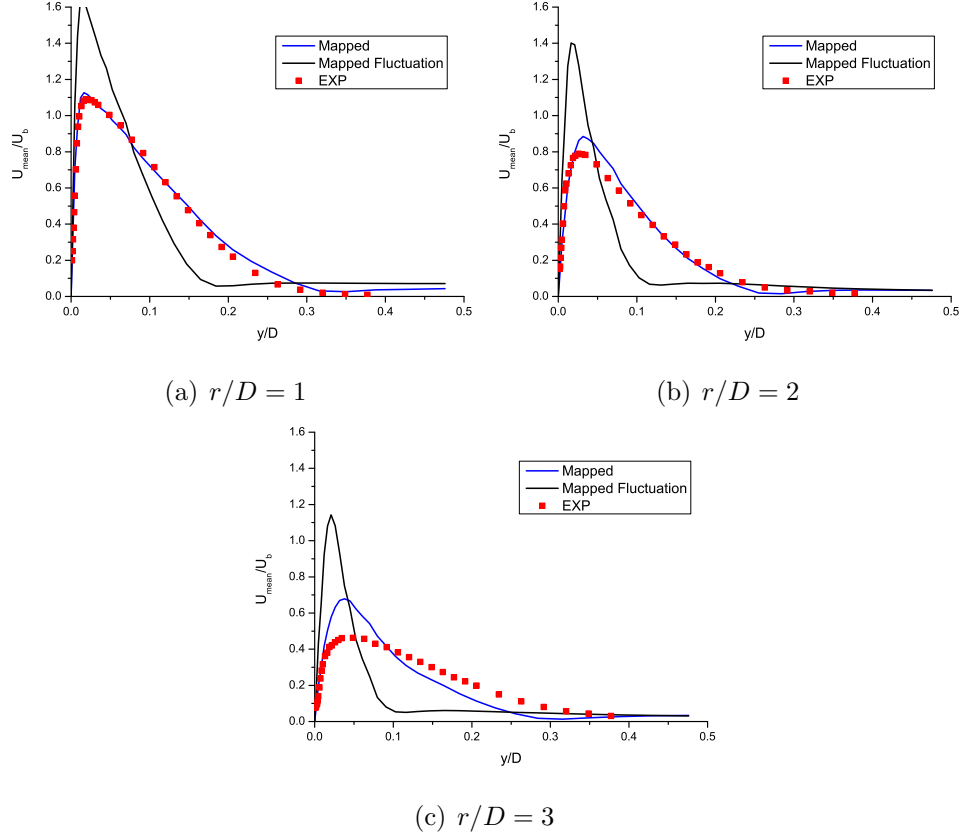
Figure 3.10: Mean velocity magnitude normal profiles - Wall jet zone.

The time averaged flow was not the only subject of the analysis, unsteady effects were also monitored computing the effective mean value of velocity fluctuation in the axial $\overline{U'^2_z}$ and radial directions $\overline{U'^2_r}$; also cross fluctuations $\overline{U'_r U'_z}$ were available from the experiments. Due to the poor predictions for mean velocity obtained with the mapped fluctuation boundary condition, only mapped computation data are presented.

Fig. 3.11 reports the radial fluctuations at increasing radii. Both the predicted and measured results show a first peak very close to the wall followed by a second more intense peak at y/D = 0.1. This second peak increases in intensity up to r/D = 2, where it starts to smooth out and to incorporate

the first peak as well. As for the mean velocity, the computations are not able to reproduce the rapid decrease of this maximum starting between r/D =2 and r/D =2.5, however a good qualitative and quantitative agreement is found up to r/D = 2.

Concerning the axial fluctuations, i.e. those directed normally to the wall, these proved to be much smaller than the radial ones at least in the wall jet zone according to both measurements and LES. Except for the section corresponding to the pipe lip, the profile is a smooth curve with one maximum located corresponding to the second peak found for the radial fluctuations. Agreement is found between computations and experiments on the generated shape of the profile for r/D up to 2. For r/D = 2.5 and 3 the numerical results strongly overestimate the experimental results at lower y/D values.

Inside the stagnation region the near wall fluctuations are quite well captured both in radial and axial direction, see Figs. 3.11(a) and 3.12(a), however as soon as y/D become higher than 0.2 the axial fluctuations are overpredicted while the radial are in underestimation.

The growth of cross fluctuation in Fig. 3.13 shows how numerical predictions do not exhibit a strong dependency on the radial position, with a negative minimum around -0.006 at 0.1<y/D<0.2 for r/D = 1,2.5,3. The measurements instead register a significant increase in the absolute fluctuation value progressively moving towards the predictions and obtaining a good agreement at r/D = 3.

3.4.6.2   Heat transfer analysis

The heat transfer predictions are reported in terms of mean Nusselt number radial distribution in Fig. 3.14. The Nusselt number is computed by sampling the wall temperature and exploiting the inlet static temperature as a

(a) $r/D = 0.5$

(b) $r/D = 1$

(c) $r/D = 1.5$

(d) $r/D = 2$

(e) $r/D = 2.5$

(f) $r/D = 3$
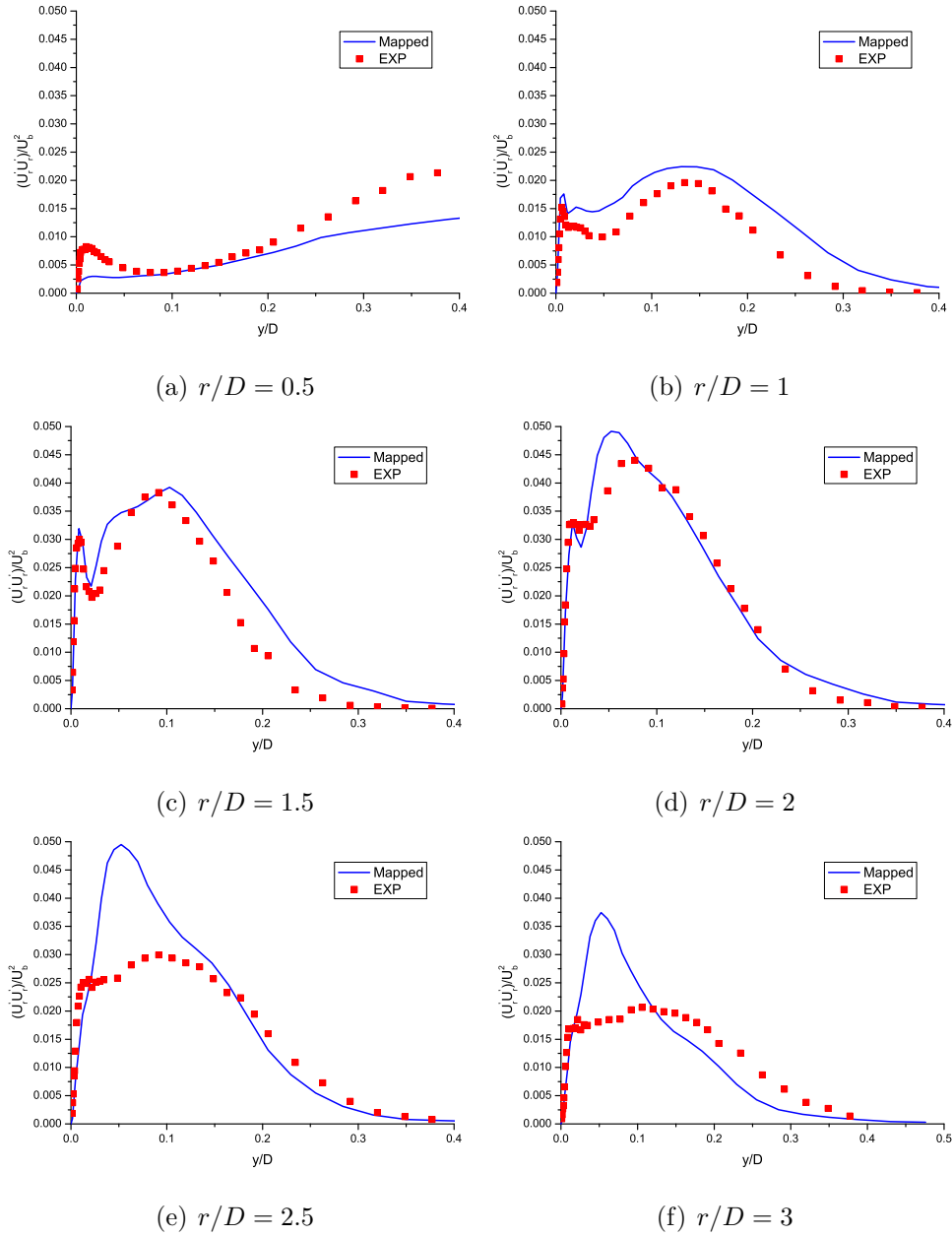
Figure 3.11: Radial effective fluctuation.

reference.

Unlike the flow field which description has found a certain grade of agreement among the researchers, heat transfer, especially in the stagnation and
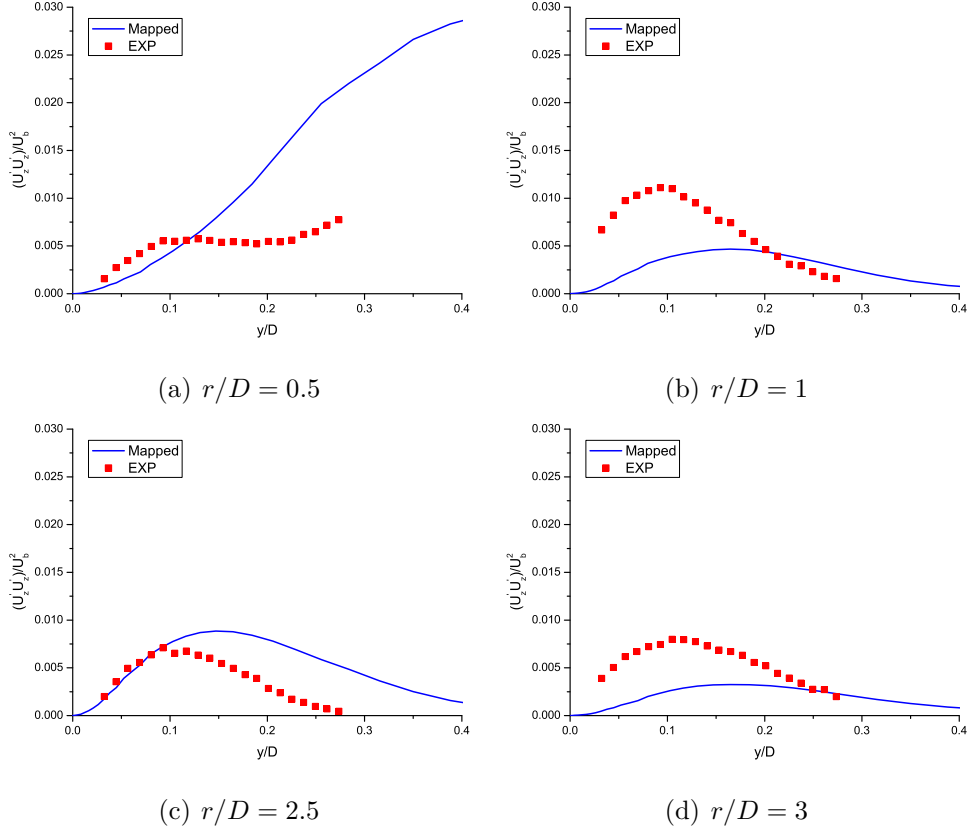
Figure 3.12: Axial effective fluctuation.

jet deflection regions has been and is still surrounded by some controversy [61]. In particular the presence of a stagnation point dip in the heat transfer level [134] and the prediction of the secondary peak at r/D $\approx$ 2 [62] are the most discussed features.

The current numerical work shows a single peak of mean Nusselt number corresponding to the stagnation region, thus no dip and no secondary peak is revealed in the proposed profile.

Both the computations show an equivalent almost asymptotic behaviour for r/D $>$ 4 reaching an outer Nusselt number around 40. The biggest influence of the boundary condition is once again seen around the stagnation

(a) $r/D = 0.5$

(b) $r/D = 1$

(c) $r/D = 2.5$

(d) $r/D = 3$
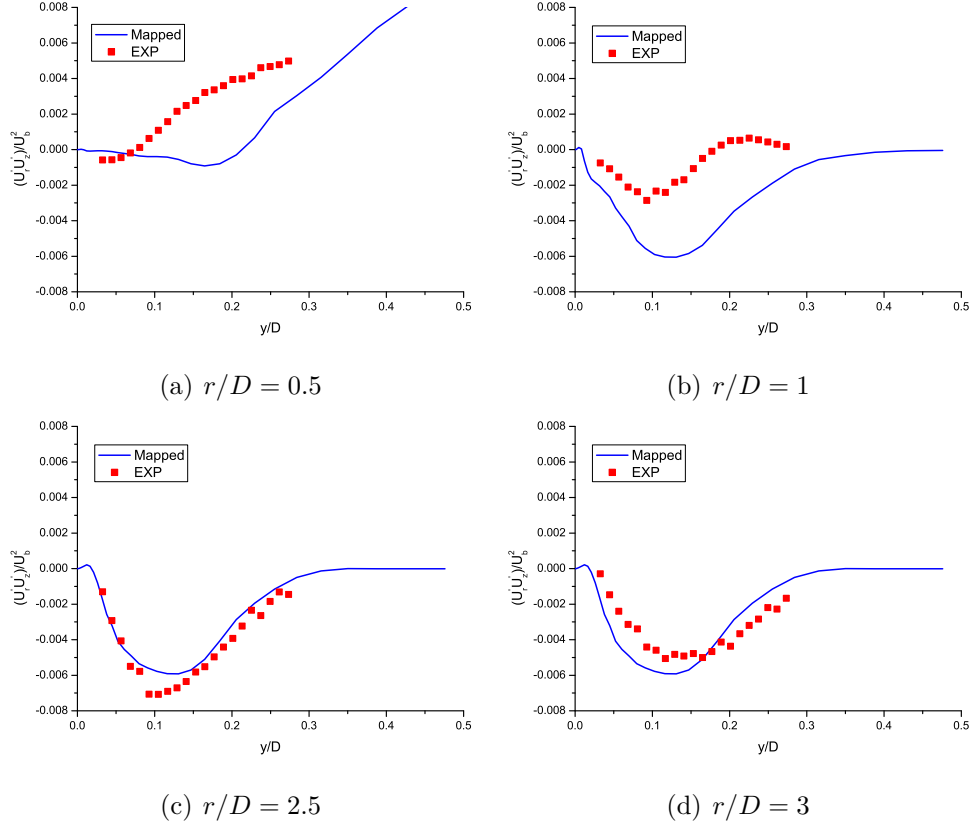
Figure 3.13: Cross effective fluctuations.

point where the impinging effect in the mapped fluctuation is certainly over-predicted due to the too high momentum contained in the centerline stream-lines. On the contrary the flatter profile of the mapped simulation reproduces quite well both the peak value and the onset of the decrease of heat transfer after the pipe lip.

The development of the secondary peak is probably related to the large-scale eddies formed by the broken ring vortices which impinge periodically on the target plate [61]. Even though it is not easy to discover why such an effect is not revealed by the computations, from the fluctuation profiles presented in Fig. 3.12 it is possible to assess that axial fluctuations are indeed
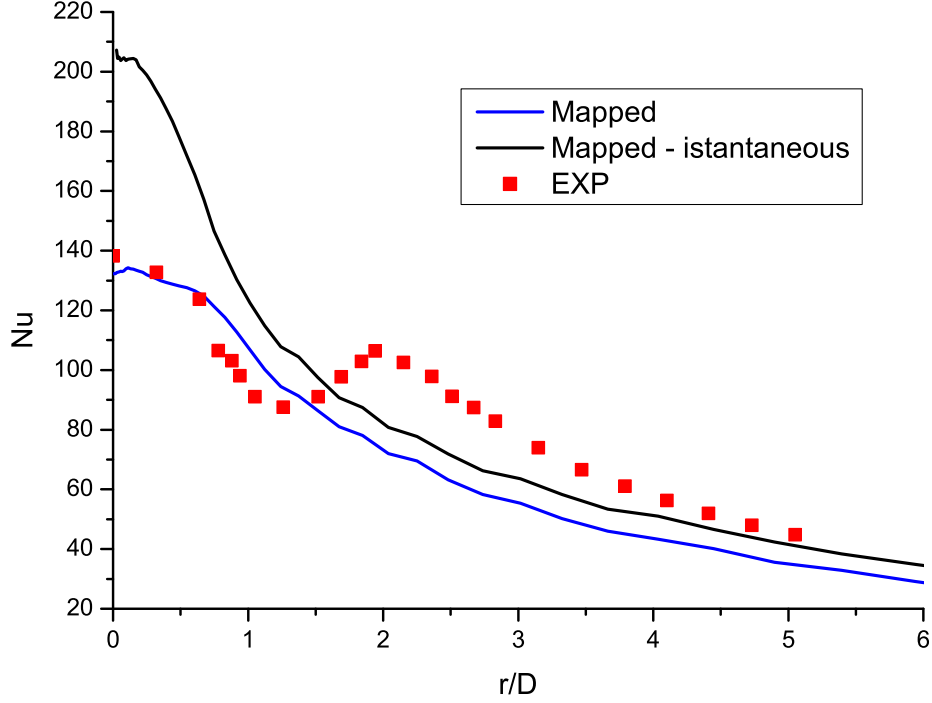
Figure 3.14: Nusselt number radial distribution.

underpredicted for r/D<2.5. The influence of the axial fluctuations on the heat transfer enhancement may also be relevant in the case of small fluctuations since normal to the plate fluctuations promote the mixing between cold air from the upper layers and the heated near wall films. Disappearance of the secondary peak is also found in [135] in the case of an excited jet. It is possible that the tested boundary conditions may have introduced a pulsating behaviour capable of suppressing the development of such a secondary peak. Other works reporting no or partial secondary peak development are [93], in which a RANS analysis showed a strong dependency on the turbulence model for the prediction of such an effect, and [62] where a similar LES computation was performed for Re=20000.

3.5   Concluding remarks

The two auto-recycling turbulent inlet conditions proposed showed quite a different behavior for the axi-symmetric impinging jet tested due to the non matching inlet mean flow conditions achieved. The mapped condition showed a reasonably good agreement with the available experimental data while for the mapped fluctuations the parabolic inlet profile is responsible for the much thinner wall jet and the consequent misprediction of both mean velocity and fluctuations profiles. Concerning the mapped BC mean velocity profiles and radial fluctuations are in very good agreement up to r/D=2 where the influence of the inlet boundary is higher, for larger values of r coarsening of the computational grid results in larger discrepancies with the measurements. Partial success in the prediction of the heat transfer level was obtained with stagnation point and asymptotic level well reproduced but no secondary peak revealed. Further analysis with consistent mean values are needed to verify the capability of the mapped fluctuations BC to reproduce coherent turbulent unsteady behavior.

Chapter 4

Navier-Stokes Characteristic boundary conditions

Contents

This chapter describes in detail the Navier-Stokes Characteristic boundary conditions (NSCBC) and the Linear Relaxation Method (LRM) employed for incoming characteristic waves. The implemented algorithm and the test cases used to validate such implementation are analysed and discussed. Their performance as effective acoustically forcing boundary were evaluated on a literature test case used also as a validation for the postporcessing technique. Finally analysis is extended to a similar test case with geometrical and flow conditions typical for real cooling devices.

4.1   Characteristic boundary conditions

NSCBC is a method based on the "characteristic lines" which inherits most concepts from Euler Characteristic boundary conditions (ECBC) methods by Thompson [130, 131] with an additional adaptation for the diffusive terms due to viscous and conductivity effects. The basic idea Thompson developed was that any hyperbolic system could be associated with a corresponding system of propagating waves, namely incoming and outgoing waves. At the boundaries, outgoing waves are completely determined by the solution in-

side the domain and do not provide any degrees of freedom while incoming waves cannot be fully determined unless some complementary information is given, the so called boundary conditions. Following the terminology adopted by Poinsot [107], two classes of boundary conditions may be distinguished, physical and numerical:

Physical boundary conditions : specify the known physical behaviour of one or more of the dependent variables. This kind of boundary condition does not depend on the adopted numerical method. The number of physical boundary conditions should match theoretical results for well-posedness of the formulated problem [124]. See Table 4.1 where the number of necessary conditions for a non-reacting flow are summarized. Both in Eulerian and Navier-Stokes cases these are obtained through the characteristic theory; firstly a number of conditions are derived from the number of characteristic waves entering the domain and secondly, only for the Navier-Stokes case, a number of viscous conditions derived from the presence of second derivatives in the governing equations is added.

Type of boundary	Euler	Navier-Stokes
Supersonic inflow	5	5
Subsonic inflow	4	5
Supersonic outflow	0	4
Subsonic outflow	1	4

Table 4.1: Number of physical boundary conditions required for well-posedness of a non-reacting flow

Numerical boundary conditions : are needed by the numerical method

used. The number of necessary numerical boundary conditions needed is equal to the number of independent primitive variables less the number of physical boundary conditions imposed. Numerical boundary conditions have no physical base, in fact the flow outside the domain imposes the condition and a numerical condition may be far from the physical behaviour of the boundary. The most common numerical boundary condition is extrapolation of order zero which imposes a zero gradient condition on the extrapolated variable. There exist extrapolations of higher order but are difficult to generalize on unstructured grids.

The concept behind ECBC and NSCBC is to impose boundary conditions in terms of characteristic waves, those related to entering waves calculated with information added from the user while those related to the leaving waves are totally extrapolated from the interior of the domain.

4.1.1 Characteristic Navier-Stokes equations on a boundary

The set of Navier-Stokes equations can be recast in characteristic form as reported in App. A, following the analysis of Lodato et al. [88]. Such a system of equations is valid also on a boundary surface. Considering a boundary with normal x_1, and tangential versors x_t (t=1,2); the terms in the x_1 direction can be recast separately to split the normal to the boundary propagation terms (d_i) from those in the other directions:

$$\frac{\partial \rho}{\partial t} + d_1 + \frac{\partial \rho u_t}{\partial x_t} = 0 \tag{4.1}$$

$$\frac{\partial \rho u_1}{\partial t} + u_1 d_1 + \rho d_2 + \frac{\partial \rho u_1 u_t}{\partial x_t} = \frac{\partial \tau_{1j}}{\partial x_j} \tag{4.2}$$

$$\frac{\partial \rho u_2}{\partial t} + u_2 d_1 + \rho d_3 + \frac{\partial \rho u_2 u_t}{\partial x_t} + \frac{\partial p}{\partial x_2} = \frac{\partial \tau_{2j}}{\partial x_j} \tag{4.3}$$

$$\frac{\partial \rho u_3}{\partial t} + u_3 d_1 + \rho d_4 + \frac{\partial \rho u_3 u_t}{\partial x_t} + \frac{\partial p}{\partial x_3} = \frac{\partial \tau_{3j}}{\partial x_j} \tag{4.4}$$

$$\frac{\partial \rho E}{\partial t} + \frac{1}{2}\left(u_k u_k\right) d_1 + \frac{d_2}{(\gamma - 1)} + \rho u_1 d_2 + \rho u_2 d_3 + \rho u_3 d_4 + \frac{\partial \rho u_t h}{\partial x_t} = $$
$$\frac{\partial}{\partial x_t}\left(\lambda \frac{\partial T}{\partial x_t}\right) + \frac{\partial u_i \tau_{ij}}{\partial x_i} \tag{4.5}$$

An expression for vector d can be derived from characteristic analysis as a combination of $\mathcal{L}_i$ representing the amplitude variations of the ith characteristic wave, as described in detail in App. A:

$$d = \begin{pmatrix} d_1 \\ d_2 \\ d_3 \\ d_4 \\ d_5 \end{pmatrix} = \begin{pmatrix} \frac{\partial \rho u_1}{\partial x_1} \\ u_1 \frac{\partial u_1}{\partial x_1} + \frac{1}{\rho}\frac{\partial p}{\partial x_1} \\ u_1 \frac{\partial u_2}{\partial x_1} \\ u_1 \frac{\partial u_3}{\partial x_1} \\ \rho c^2 \frac{\partial u_1}{\partial x_1} + u_1 \frac{\partial p}{\partial x_1} \end{pmatrix} = \begin{pmatrix} \frac{1}{c^2}\left[\mathcal{L}_2 + \frac{1}{2}\left(\mathcal{L}_5 + \mathcal{L}_1\right)\right] \\ \frac{1}{2\rho c}\left(\mathcal{L}_5 - \mathcal{L}_1\right) \\ \mathcal{L}_3 \\ \mathcal{L}_4 \\ \frac{1}{2}\left(\mathcal{L}_5 + \mathcal{L}_1\right) \end{pmatrix} \tag{4.6}$$

Each $\mathcal{L}_i$ is thus associated with a wave and its respective velocity λ_i:

$$\lambda_1 = u_1 - c \quad ; \quad \lambda_2, \lambda_3, \lambda_4 = u_1 \quad ; \quad \lambda_5 = u_1 + c \tag{4.7}$$

Characteristic waves are represented in Fig. 4.1 for a schematic flow domain, where x_1 is oriented positively with the respect to the direction of the flow both at inlet and outlet. λ_1 and λ_5 are respectively the velocities of co-flow and counter-flow directed acoustic waves; λ_2 is the velocity for entropy advection; λ_3 and λ_4 are vorticity wave velocities.

In order to adopt characteristic boundary conditions it is necessary to know all wave amplitude variations on the boundary. Outgoing waves can be calculated by definition since these are dependent only on the internal flow
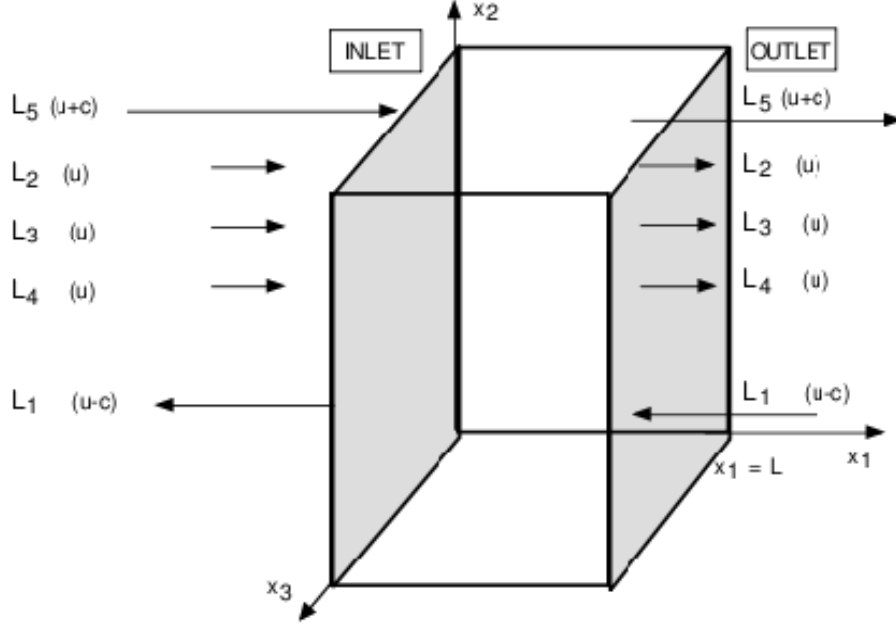
Figure 4.1: Entering and leaving characteristic waves from boundaries with x_1 normal (from Selle et al. [118])

field, incoming waves in contrast cannot. The latter contain information from the space external to the domain and it would be a physical error to compute their amplitudes using points inside the domain. These waves must be specified by the boundary conditions. Except simple cases where an analytic solution is available and incoming wave amplitude variations $\mathcal{L}_i$ are thus known a priori, in most cases their values are unknown. In the next section a method for estimating incoming wave amplitude variations is given.

4.1.2   The Local One Dimensional Inviscid (LODI) relations

Incoming wave amplitude variations can be specified by making the assumption that the flow in the boundary region is one dimensional and inviscid

[130, 131]. If this is the case the relations of LODI (Local One Dimensional Inviscid problem) [107] strictly applies. LODI relations can however be obtained also from Navier-Stokes in characteristic form (see Eqs. 4.1:4.5) neglecting transverse and diffusive terms. They should not be considered physical conditions but viewed as compatibility relations between the choices made for physical boundary conditions and the amplitudes of waves crossing the boundary [107]. Here LODI are reported, as obtained in App. A, for the vector of primitive variables $U = |\rho \ u_1 \ u_2 \ u_3 \ p|^T$:

$$\frac{\partial \rho}{\partial t} + d_1 = 0 \tag{4.8}$$

$$\frac{\partial u_i}{\partial t} + d_{i+1} = 0, \ i = 1, 2, 3 \tag{4.9}$$

$$\frac{\partial p}{\partial t} + d_5 = 0 \tag{4.10}$$

Most physical boundary conditions have their LODI counterpart; for instance imposing a constant outlet pressure corresponds to $d_5 = 0$ giving $\mathcal{L}_1 = -\mathcal{L}_5$.

In the next section the strategy for NSCBC is presented. Recently many authors have noted that LODI relations may be an oversimplified way to calculate wave amplitude variations, especially for flows with strong gradients on the boundary. Thus they have relaxed the LODI hypothesis and calculate wave amplitude variations using transverse terms too [88, 141].

4.1.3 Navier-Stokes Characteristic Boundary Conditions

The procedure for constructing Navier-Stokes Characteristic boundary conditions may be divided into three steps:

1. Impose the physical boundary conditions on the known variables (e.g. for a fixed pressure outlet fix the pressure on outlet boundary)

2. Calculate wave amplitude variations through known behaviour of primitive variables of step 1 and the remaing variables with the LODI relations 4.8:4.10.

3. Integrate in time equations 4.1:4.5 with the calculated d_i and impose the "viscous conditions" on the conductive and viscous terms

Tables 4.2 and 4.3 summarize the viscous conditions for inflow and outflow boundary as reported by Poinsot and Venyante [106]. SI-1 is the only inflow condition where the number of imposed variables in the case of Navier-Stokes equations equals that of the Eulerian case. In fact, when velocity components and temperature are supplied, the only remaining variable is density which can be calculated through the continuity equation not involving diffusive terms. This condition is used in this thesis when fixed velocity and temperature are desired. In general, as suggested by Strickwerda [124], well posedness of problems with Navier-Stokes equations requires five pieces of information for inlet boundaries. For example the SI-2 condition fixes velocity components and density, but an additional viscous condition on the normal stress component must be provided, i.e. zero-gradient for the normal stress component. Both SI-3 and SI-4 are non-reflecting inlet boundary conditions; the non-reflection of acoustic waves is assured through two different approaches: SI-3 attempts to enforce a relation between primitive variables while SI-4 fixes wave amplitude variations through the boundaries.

Outflow boundaries reported in Table 4.3 present viscous condition similar to those proposed by Dutt [46]: the tangential viscous stresses (τ_{12} and τ_{13}) and the normal heat flux ($-k\frac{\partial T}{\partial x_1}$) should not vary across the boundary

itself. This condition will also be implemented in this work, instead of fixing viscous fluxes following the suggestion from Sutherland et al. [127]: fixing zero viscous fluxes normal to the boundary brings instability, in fact this condition introduces strong spatial derivatives into diffusive fluxes, which when differentiated, would produce very large terms in the governing equations.

	Euler		Navier-Stokes		
	ECBC Conditions	Total Nbr	ECBC Conditions	Viscous Conditions	Total Nbr
SI-1	u_i, T imposed		u_i, T imposed	No	
	4	4	4	0	4
SI-2	u_i, ρ imposed		u_i, ρ imposed	$\frac{\partial \tau_{11}}{\partial x_1} = 0$	
	4	4	4	1	5
SI-3	$u_1 - 2\frac{c}{\gamma-1}, u_2$ u_3, s imposed		$u_1 - 2\frac{c}{\gamma-1}, u_2$ u_3, s imposed	$\frac{\partial \tau_{11}}{\partial x_1} = 0$	
	4	4	4	1	5
SI-4	No reflected wave		No reflected wave	$\frac{\partial \tau_{11}}{\partial x_1} = 0$	
	4	4	4	1	5

Table 4.2: NSCBC for subsonic inflow

4.1.4 Linear relaxation method

In this section the description of the implementations for inlet and outlet boundaries is given. The Linear Relaxation Method (LRM) for partially

		Euler		Navier-Stokes		
		ECBC Condition	Total Nbr	ECBC Conditions	Viscous Conditions	Total Nbr
B2	Perfeclty non-reflecting outlet	No Reflection		No Reflection	$\frac{\partial \tau_{12}}{\partial x_1} = 0$ $\frac{\partial \tau_{13}}{\partial x_1} = 0$ $\frac{\partial q_1}{\partial x_1} = 0$	
		1	1	1	3	4
B3	Partially non-reflecting outlet	P at infinity imposed		P at infinity imposed	$\frac{\partial \tau_{12}}{\partial x_1} = 0$ $\frac{\partial \tau_{13}}{\partial x_1} = 0$ $\frac{\partial q_1}{\partial x_1} = 0$	
		1	1	1	3	4
B4	subsonic reflecting outlet	P outlet imposed		P outlet imposed	$\frac{\partial \tau_{12}}{\partial x_1} = 0$ $\frac{\partial \tau_{13}}{\partial x_1} = 0$ $\frac{\partial q_1}{\partial x_1} = 0$	
		1	1	1	3	4

Table 4.3: NSCBC for subsonic outflow

reflecting boundaries is introduced.

4.1.4.1   Subsonic inflow

In the case of subsonic inlet boundaries four characteristic waves are entering the domain (see Fig. 4.1) while the acoustic wave $\mathcal{L}_1$ is leaving the domain. Considering prescribed steady inflow conditions and thus referring to SI-1 case four physical boundary conditions and one numerical boundary condition are required, no viscous condition need to be imposed. To advance the solution in time all wave amplitude variations must be determined: only $\mathcal{L}_1$ can be computed from interior points while the others need to use LODI

relations as follows:

1. Compute $\mathcal{L}_1$ using relation A.14

2. With u_1 fixed, Eq. 4.9 gives $\mathcal{L}_5 = \mathcal{L}_1$. For the other wave amplitude variations, the same equation assign $\mathcal{L}_3 = \mathcal{L}_4 = 0$; finally entropy wave time amplitude variation may be computed from LODI relation for temperature:

$$\frac{\partial T}{\partial t} + \frac{T}{\gamma p}\left[\mathcal{L}_2 + \frac{1}{2}(\gamma - 1)(\mathcal{L}_1 + \mathcal{L}_5)\right] = 0 \tag{4.11}$$

hence $\mathcal{L}_2 = \frac{1}{2}(\gamma - 1)(\mathcal{L}_1 + \mathcal{L}_5) = (\gamma - 1)\mathcal{L}_1$. $\mathcal{L}_2 = \mathcal{L}_4 = 0$

3. Use the continuity equation in characteristic form 4.1 to advance in time the density; d_1 term can be calculated by definition (see vector d in relation 4.6).

However this procedure models totally reflecting inlet conditions: inlet sections with fixed velocities and temperature lead to full reflection of incident acoustic waves. An infinite acoustic impedance inlet may not be appropriate in compressible flow calculations, a partially reflecting inlet, as a finite impedance surface is, could be a good modeling technique for acoustic computations. A technique to achieve this property is to relax the wave amplitude variation of incoming waves:

$$\begin{aligned}
\mathcal{L}_2 &= \sigma_T \left(T - T^T\right) \\
\mathcal{L}_3 &= \sigma_{u_2} \left(u_2 - u_2^T\right) \\
\mathcal{L}_4 &= \sigma_{u_3} \left(u_3 - u_3^T\right) \\
\mathcal{L}_5 &= \sigma_{u_1} \left(u_1 - u_1^T\right)
\end{aligned} \tag{4.12}$$

This kind of procedure is commonly known as the Linear Relaxation Method (LRM) [141]. Appropriate values of the relaxation coefficients σ

provide a partially reflecting behaviour for the boundary. If the relaxed variable drifts from its target value its corresponding wave amplitude variation acts as a linear spring force to push it back toward its target value. Thus the σ_i parameters should be chosen to match the correct inlet impedance. No exact method exists to determine σ_i for an acoustically defined inlet section; in this thesis a procedure proposed by Yoo et al. [140] and based on the simplified model equations is followed. The basis of this procedure is reported in App. B.

4.1.4.2   Subsonic outflow

The treatment of outlet boundaries is quite delicate in compressible flow computations and in aeroacoustic analysis particularly. A perfectly non-reflecting outlet ($\mathcal{L}_1 = 0$) does not provide a constant mean pressure in the flow field, due to the fact that no information about the state pressure at infinity is fed back into the domain. The problem may not be well posed in fact, as is seen by referring to Fig. 4.2, the flow in the computational domain is not able to determine the mean pressure, because reflected acoustic waves generated from drifts of outlet pressure values from p_∞ do not cross the domain.

Many solutions to this problem have been proposed, but only a few results are applicable to generalized flows. The LRM technique already seen for partially reflecting inlet (see Sec. 4.1.4.1) is one of these.

The formulation for a partially reflecting outlet, first proposed by Rudy and Strickwerda [113], is:

$$\mathcal{L}_1 = K\left(p - p_\infty\right) \quad , \quad K = \sigma_p\left(1 - \mathcal{M}^2\right)\frac{c}{L} \tag{4.13}$$

where p_∞ is the target pressure for outlet, $\mathcal{M}$ is the characteristic Mach number of the flow and L is a characteristic domain length (in the case of a
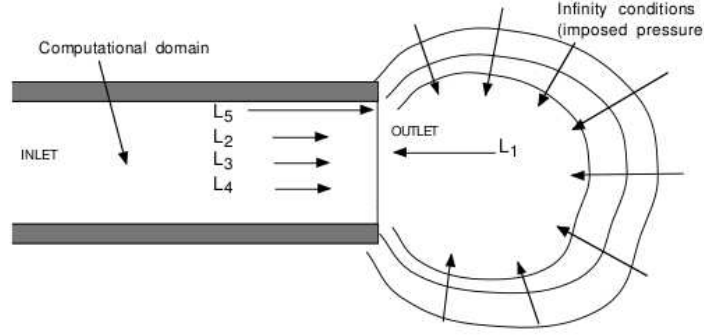
Figure 4.2: Role of infinity condition for fix mean pressure in the domain

duct the duct's length). K has the dimension of a frequency and determines the reflectivity of the boundary. For large values of this constant the outlet pressure relaxes quickly toward the pressure at infinity. Theoretically for an infinite value of K the fixed pressure outlet condition is recovered. In Eq. 4.13 is reported the procedure for determining K proposed by Rudy and Strickwerda [113]. These authors suggested an optimum value of $\sigma_p = 0.27$ based on theoretical analysis and computational experiments. Other numerical studies from Poinsot and Lele [107] found a different optimum $\sigma_p = 0.58$. More recently Selle et al. [118] gave some more convincing guidelines in the evaluation of this relaxation coefficient. Their analysis, reproduced later in App. B, is based on the acoustic response of a 1D duct modeled with NSCBC at the outlet. The main results are that $\sigma_{p\ max} = \pi$ permits to evacuate all duct modes from the outlet. The minimum for σ_p is not fixed by acoustics, many other factors determine this low limit such as Reynolds number and geometry. Considering the natural frequencies of an acoustically closed duct (fixed inlet velocity and fixed outlet pressure):

$$f_n = \frac{(2n+1)c}{4L} \tag{4.14}$$

their main results are reported in Fig. 4.3.
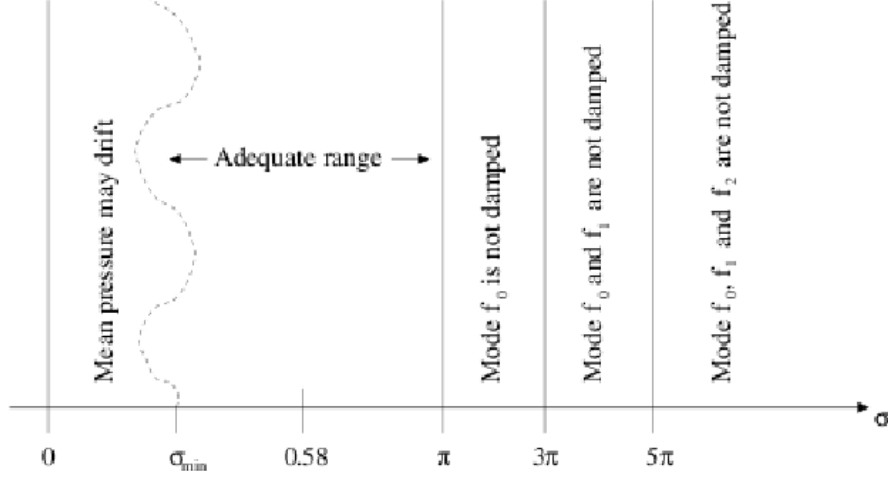
Figure 4.3: Summary of influence of σ_p on acoustics and mean flow quantities for a 1D flow (from Selle [118])

For a more complex case such as a 3D computation Selle et al. [118] suggest to evaluate the maximum σ_p such that the outlet boundary is able to sufficiently damp the first acoustic mode of the system. The same analysis conducted so far can be found with more details in [56].

4.2 Implementation details

In this section a brief description of the NSCBC implementation in a generic pressure based compressible solver is presented.

4.2.1 NSCBC algorithm

The implementation used in this work differs from the previously reported algorithm, see Sec.4.1.3, adopted by Poinsot only for the third step. In fact

it has been chosen to advance in time directly the set of primitive variables mentioned in Sec. 4.1.2, for which the LODI relations 4.8:4.10 have been determined.

The Navier-Stokes equations in characteristic form for the vector of primitive variables $U = |\rho\ u_1\ u_2\ u_3\ p|^T$ are obtained in App. A:

$$\frac{\partial \rho}{\partial t} + d_1 + \frac{\partial \rho u_t}{\partial x_t} = 0 \tag{4.15}$$

$$\frac{\partial u_1}{\partial t} + d_2 + \frac{\partial u_1}{\partial x_t} u_t = \frac{1}{\rho} \frac{\partial \tau_{1j}}{\partial x_j} \tag{4.16}$$

$$\frac{\partial u_2}{\partial t} + d_3 + \frac{\partial u_2}{\partial x_t} u_t + \frac{1}{\rho} \frac{\partial p}{\partial x_2} = \frac{1}{\rho} \frac{\partial \tau_{2j}}{\partial x_j} \tag{4.17}$$

$$\frac{\partial u_3}{\partial t} + d_4 + \frac{\partial u_3}{\partial x_t} u_t + \frac{1}{\rho} \frac{\partial p}{\partial x_3} = \frac{1}{\rho} \frac{\partial \tau_{3j}}{\partial x_j} \tag{4.18}$$

$$\frac{\partial p}{\partial t} + d_5 + \gamma p \frac{\partial u_t}{\partial x_t} + \frac{\partial p}{\partial x_t} u_t = (\gamma - 1) \tau_{ij} \frac{\partial u_i}{\partial x_j} + (\gamma - 1) \frac{\partial}{\partial x_j} \left(k \frac{\partial T}{\partial x_j} \right) \tag{4.19}$$

Besides the d vector, responsible for the normal to the boundary contribution and already reported in Eq.B.3, for convenience two more vectors are defined: T for transversal terms and D for diffusive terms. They are obtained in App.A and here reported:

$$T = \begin{pmatrix} T_1 \\ T_2 \\ T_3 \\ T_4 \\ T_5 \end{pmatrix} = \begin{pmatrix} \frac{\partial \rho u_t}{\partial x_t} \\ \frac{\partial u_1}{\partial x_t} u_t \\ \frac{\partial u_2}{\partial x_t} u_t + \frac{1}{\rho} \frac{\partial p}{\partial x_2} \\ \frac{\partial u_3}{\partial x_t} u_t + \frac{1}{\rho} \frac{\partial p}{\partial x_3} \\ \gamma p \frac{\partial u_t}{\partial x_t} + \frac{\partial p}{\partial x_t} u_t \end{pmatrix} \quad , \quad t = 2,3 \tag{4.20}$$

$$D = \begin{pmatrix} D_1 \\ D_2 \\ D_3 \\ D_4 \\ D_5 \end{pmatrix} = \begin{pmatrix} 0 \\ \frac{1}{\rho}\frac{\partial \tau_{1j}}{\partial x_j} \\ \frac{1}{\rho}\frac{\partial \tau_{2j}}{\partial x_j} \\ \frac{1}{\rho}\frac{\partial \tau_{3j}}{\partial x_j} \\ (\gamma - 1)\,\tau_{ij}\frac{\partial u_i}{\partial x_j} + (\gamma - 1)\frac{\partial}{\partial x_j}\left(k\frac{\partial T}{\partial x_j}\right) \end{pmatrix} \tag{4.21}$$

Following such decomposition the set of equations 4.15:4.19 can be recast in vectorial form in a more compact way:

$$\frac{\partial U}{\partial t} + d + T = D \tag{4.22}$$

With limitation to subsonic flows, only two kinds of boundary have been identified and specified: inlet and outlet. This division is required in order to define which characteristic wave amplitude variations can be extrapolated (calculated from the interior points) and which one have to be calculated with additional information in the form of physical boundary conditions. Thus keeping as a reference Fig.4.1 and using the LRM technique for both inlet and outlet we calculate $\mathcal{L}_i$ in the two different cases as reported in table 4.4

	$\mathcal{L}_1$	$\mathcal{L}_2$	$\mathcal{L}_3$	$\mathcal{L}_4$	$\mathcal{L}_5$
Inlet	Extr	LRM	LRM	LRM	LRM
Outlet	LRM	Extr	Extr	Extr	Extr

Table 4.4: Linearly relaxed inlet and outlet NSCBC summary - Extr: Extrapolated, LRM: Linear Relaxation Method

4.2.2 Time integration

Time discretization schemes adopted in this work are explicit Euler, backward and Crank-Nicholson. What is obtained after calculation of the vectors d, T and D is a derivative of the primitive variables ρ, u_1, u_2, u_3, and p. The integration procedure differs between the available discretization schemes to be coherent with the adopted time discretization scheme in the internal domain. A specific function was developed taking as arguments variable derivative, old time step value and the value from two previous iterations. Then the procedure to integrate the variable is as follow:

$$\text{Euler timescheme:} \quad \psi^{i+1} = \psi^i + \frac{d\psi}{dt}\Delta T \tag{4.23}$$

$$\text{Backward timescheme:} \quad \psi^{i+1} = \frac{4\psi^i - \psi^{i-1} + 2\frac{d\psi}{dt}\Delta T}{3} \tag{4.24}$$

$$\text{Crank-Nicholson timescheme:} \quad \psi^{i+1} = 2\psi^i - \psi^{i-1} + 2\frac{d\psi}{dt}\Delta T \tag{4.25}$$

4.2.3 Viscous terms

In this section the imposition of viscous conditions is discussed. Attention will be focused on conditions SI-1 and SI-4 for inlet and BI-3 for outlet, which are the ones used in this thesis. Condition SI-1 is the most straightforward, as a matter of fact no condition is imposed, hence all components of the stress tensor τ_{ij} are included. Condition SI-4 for a non-reflecting inlet introduces the zero normal derivative assumption of the component τ_{11}. This condition has been included in the implementation as correction in the calculus of terms D_2 for momentum equation and D_5 for energy equation. The first transforms:

$$D_2 = \frac{1}{\rho}\left(\frac{\partial \tau_{1j}}{\partial x_j}\right) \quad , \quad j = 1:3 \rightarrow \frac{1}{\rho}\left(\frac{\partial \tau_{1t}}{\partial x_t}\right) \quad , \quad t = 2,3 \tag{4.26}$$

The second term does not change but the viscous term τ_{11} in the stress tensor is substituted with the internal field value, see the following section for more detail. The same approach has been used for the implementation of viscous conditions for outlet BI-3;the equations for the tangential component of the velocities are modified in the following way:

$$D_3 = \frac{1}{\rho}\left(\frac{\partial \tau_{2j}}{\partial x_j}\right) \quad , \quad j = 1:3 \rightarrow \frac{1}{\rho}\left(\frac{\partial \tau_{2t}}{\partial x_t}\right) \quad , \quad t = 2,3 \qquad (4.27)$$

$$D_4 = \frac{1}{\rho}\left(\frac{\partial \tau_{3j}}{\partial x_j}\right) \quad , \quad j = 1:3 \rightarrow \frac{1}{\rho}\left(\frac{\partial \tau_{3t}}{\partial x_t}\right) \quad , \quad t = 2,3 \qquad (4.28)$$

The energy equation for primitive variable T is unchanged for the viscous term, but again τ_{21} and τ_{31} terms are calculated as internal field values, while the convection term is modified:

$$D_5 = (\gamma - 1)\frac{\partial}{\partial x_j}\left(k\frac{\partial T}{\partial x_j}\right) \quad , \quad j = 1:3 \rightarrow (\gamma - 1)\frac{\partial}{\partial x_t}\left(k\frac{\partial T}{\partial x_t}\right) \quad , \quad t = 2,3$$
$$(4.29)$$

4.2.4   Discretization of derivatives

The calculus of characteristic wave amplitude variation requires particular attention. Near the boundaries, accuracy in the conservation equation decreases. Using the Finite Difference Method (FDM) centered differences have to be replaced by one-sided differencing because grid points are available only in the interior of the domain [106]. Implementation in FVM preserves this weakness in the calculation of normal derivatives on the boundary. Characteristic and transverse terms require a procedure for calculating the following kind of derivatives: $\left(\frac{\partial \psi}{\partial x_1}\right)_b$ and $\left(\frac{\partial \psi}{\partial x_t}\right)_b$ $,t = 2,3$. First order derivatives evaluated on the boundary are discretized in the following way, with nomen-

clature described in Fig.4.4:

$$\left(\frac{\partial \psi}{\partial x_1}\right)_b = \frac{\psi_P - \psi_S}{|x_P - x_S| \cdot n} \tag{4.30}$$

Tangential derivatives on the boundaries have been discretized using 2D Gauss theorem for calculating the divergence on the boundary:

$$\left(\frac{\partial \psi}{\partial x_t}\right)_b = \frac{1}{S} \int_S \frac{\partial \psi}{\partial x_t} dS = \frac{1}{S} \int_{\delta S} \psi \delta l \approx \frac{1}{S} \sum_e \psi_e l_e \tag{4.31}$$

with the l_e vector normal to the edge of the face boundary and of magnitude equal to its length. A finite area library implementing such discretization was thus exploited to evaluate tangential gradients.
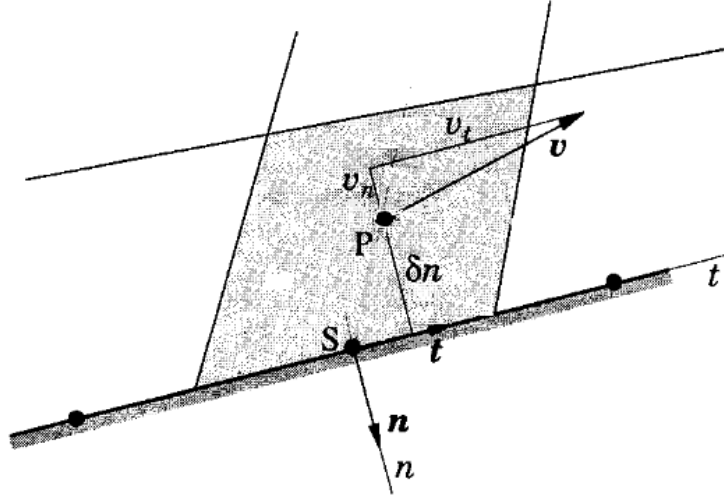

Figure 4.4: Nomenclature for discretization procedure of normal to boundary derivatives

Implementation of the viscous terms D required an approximation for second order derivatives and the imposition of viscous conditions. Substitution of terms evaluated on the boundary with terms in the internal domain,

the above mentioned internal field values, helped with the evaluation of those terms. For the first issue the problem reduced to one of how to calculate the following derivatives: $\left(\frac{\partial^2 \psi}{\partial^2 x_1}\right)_b$, $\left(\frac{\partial^2 \psi}{\partial x_t \partial x_1}\right)_b$ and $\left(\frac{\partial^2 \psi}{\partial x_t \partial x_t}\right)_b$.

The first derivative has been resolved by considering the difference quotient of first order derivatives:

$$\frac{\partial^2 \psi}{\partial^2 x_i} \approx \frac{\frac{\partial \psi}{\partial x_1}{}_S - \frac{\partial \psi}{\partial x_1}{}_P}{|x_P - x_S| \cdot n} \tag{4.32}$$

In Eq.4.32, $\left(\frac{\partial \psi}{\partial x_1}\right)_S$ is calculated as described before, while $\left(\frac{\partial \psi}{\partial x_1}\right)_P$ is the already mentioned internal field value, evaluated by means of the 3D Gauss theorem on the next-to-the-boundary cell:

$$\frac{\partial \psi}{\partial x_i} = \frac{1}{V} \int_V \frac{\partial \psi}{\partial x_i} dV = \frac{1}{V} \int_{\delta V} \psi \cdot dS \approx \frac{1}{V} \sum_f \psi_f S_f \tag{4.33}$$

The same approach for calculating $\left(\frac{\partial^2 \psi}{\partial^2 x_1}\right)_b$ is adopted for $\left(\frac{\partial^2 \psi}{\partial x_t \partial x_1}\right)_b$. The only difference is in the evaluation of the tangential derivative on the boundary which, as said before, is second order accurate. Finally $\left(\frac{\partial^2 \psi}{\partial x_t \partial x_t}\right)_b$, involving no normal derivatives, is entirely evaluated with finite area discretization procedures.

4.3   Validation

The aim of this section is to demonstrate the potentialities of NSCBC for unsteady flows, with particular emphasis on the permeability to acoustic incident waves, a key feature for accurate acoustic simulations. Simulated test cases will be presented in order of increasing physical complexity.

4.3.1 Shock-tube

The problem examined in this section is the classical 1D shock-tube, already proposed as a direct validation problem for non-reflecting boundaries (see [130, 131]). At time t=0 the system consists of two separated regions of quiescent fluid, a high pressure region (p=100000 Pa, T=278.746 K) on the left side and a low pressure region (p=10000 Pa, T=348.432 K) on the right side. As time progress rarefaction waves move to the left, progressively expanding the high pressure portion of the domain and a shock wave crosses the right portion of the domain instantaneously compressing and accelerating the crossed fluid. The completely non-reflecting outflow is tested at the right boundary ($\sigma_p = 0 \rightarrow \mathcal{L}_1 = 0$). Correct behaviour of the boundary should follow the analytical solution, which consists of a one-step transformation of all fluid-dynamics and thermodynamic variables moving at the speed of sound.

In Fig. 4.5 pressure distribution along the domain is reported for different snapshots, showing the movement of the high-to-low pressure interface towards the right side. A zoom on the low pressure region just before and after the shock wave passed through is shown in Fig. 4.6. No reflections are visible on either sides of the domain, especially the low pressure one which is subjected to shock wave crossing: the boundaries are therefore demonstrated to behave well.

4.3.2 1D flow with partially reflecting outlet

In this section two tests are performed on 1D domains similar to that of the shock tube. In the first case the forced response of a LRM outlet subject to an harmonic propagating wave coming from a pulsating velocity inlet is
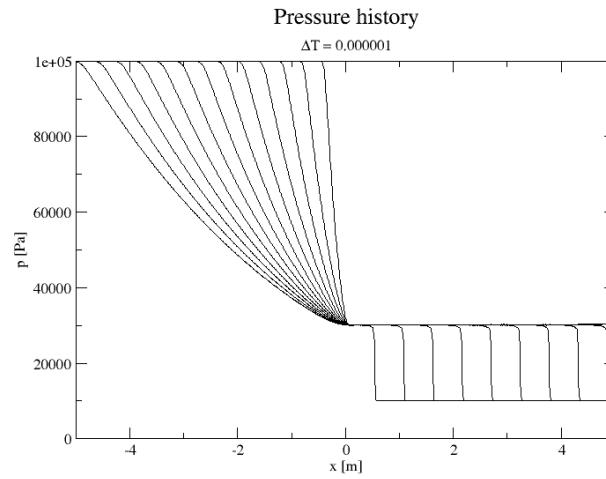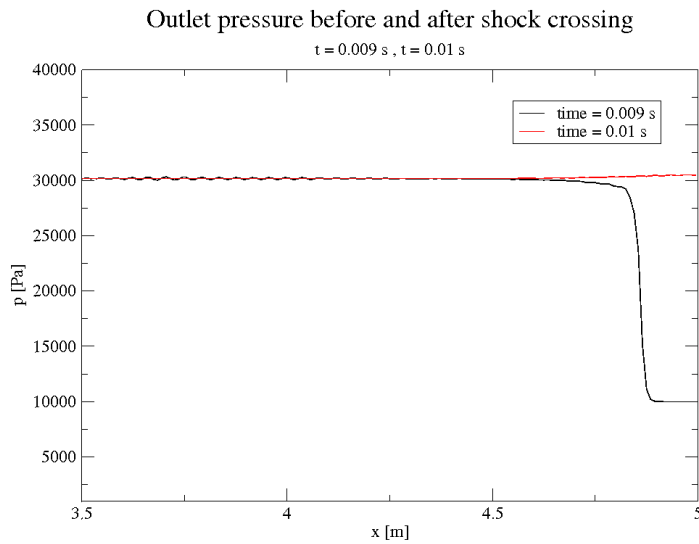
Figure 4.5: Pressure history along the tube $\Delta t = 10^{-6}s$

Figure 4.6: Pressure on the outlet section before and after shock wave crossing

studied. In the second case the natural response of a system subjected to a hard inflow and a non-reflecting outlet boundary is analysed by means of a transient simulation from an initial acoustic perturbation. For hard boundary is intended a fully reflecting boundary with prescribed velocity and temperature. Conclusions will be drawn from these analyses for tuning strategies of the LRM outlet in more complex computations.

4.3.2.1 Forced response of a LRM outlet boundary

In the simple case of semi-infinite tube of constant cross section an analytical solution can be obtained for the problem of an acoustic propagating wave and LRM outlet. Assuming a harmonic wave propagating to the right, $\mathcal{L}_5$ can be expressed in complex notation:

$$\mathcal{L}_5 = 2\rho c U_0 i\omega e^{-i\omega t} \tag{4.34}$$

As anticipated, the non-reflecting boundary is modelled with LRM to avoid drift in the mean pressure thus the formulation in Eq. 4.13 is valid. Eqs. 4.13 and 4.34, together with LODI relations for first normal to boundary velocity component and pressure, reported in Eq. 4.9 and 4.10, lead to the system of equations:

$$
\begin{cases}
\frac{\partial u_1}{\partial t} + \frac{1}{2\rho c} \left(2\rho c U_0 i\omega e^{-i\omega t} - K \left(p - p_\infty \right) \right) = 0 \\
\frac{\partial p}{\partial t} + \frac{1}{2} \left(2\rho c U_0 i\omega e^{-i\omega t} + K \left(p - p_\infty \right) \right) = 0
\end{cases} \tag{4.35}
$$

The second equation of the set 4.35 involves just the variable p and can be solved giving:

$$p(t) = \underbrace{A_0 e^{-\frac{Kt}{2}}}_{transient\ solution} + \underbrace{p_\infty - \frac{\rho c U_0 i\omega}{\frac{K}{2} - i\omega} e^{-i\omega t}}_{steady\ solution} \tag{4.36}$$

Since $K > 0$ the transient term vanishes as $t \to \infty$ and hence it will be omitted in the subsequent analysis. Substituting Eq. 4.36 into 4.13 provides

an expression for the left propagating wave $\mathcal{L}_1$:

$$\mathcal{L}_1(t) = \underbrace{KA_0 e^{-\frac{Kt}{2}}}_{transient\ solution} - \underbrace{\frac{\rho c U_0 i\omega}{\frac{K}{2} - i\omega} e^{-i\omega t}}_{steady\ solution} \tag{4.37}$$

Hence the reflection coefficient can easily be obtained as the ratio of steady harmonic terms in the expressions for $\mathcal{L}_1$ and $\mathcal{L}_5$:

$$R(\omega) = \frac{\mathcal{L}_1}{\mathcal{L}_5} = -\frac{1}{1 - i\frac{2\omega}{K}} \tag{4.38}$$

Eq. 4.38 is a simple frequency response function with one pole; magnitude and phase can be easily obtained:

$$
\begin{aligned}
|R|(\omega) &= \frac{1}{\sqrt{1 + \left(\frac{2\omega}{K}\right)^2}} \\
\varphi_R(\omega) &= -\pi - \arctan\left(\frac{2\omega}{K}\right)
\end{aligned} \tag{4.39}
$$

the asymptotic behaviour of this is reported in Table 4.5 and a Bode representation of $R(\omega)$ in Fig. 4.7.

Pulsation	$|R|$	Φ_R
$\omega = 0$	1	$-\pi$
$\omega = \infty$	0	$-\frac{3}{2}\pi$

Table 4.5: Asymptotic behaviour of LRM boundary under forced response

The control parameter in this case is $2\omega/K$: as $2\omega/K \to 0$ LRM behaves as a totally non-reflecting outlet while as $2\omega/K \to \infty$ $p \to p_\infty$ and the outlet has a reflecting behaviour. An important frequency always defined in dynamic analysis is the cut-off frequency f_c, the frequency for which the response of the system drop by 3dB ($R = 1/\sqrt{2}$):

$$f_c = \frac{\omega_c}{2\pi} = \frac{K}{4\pi} \tag{4.40}$$
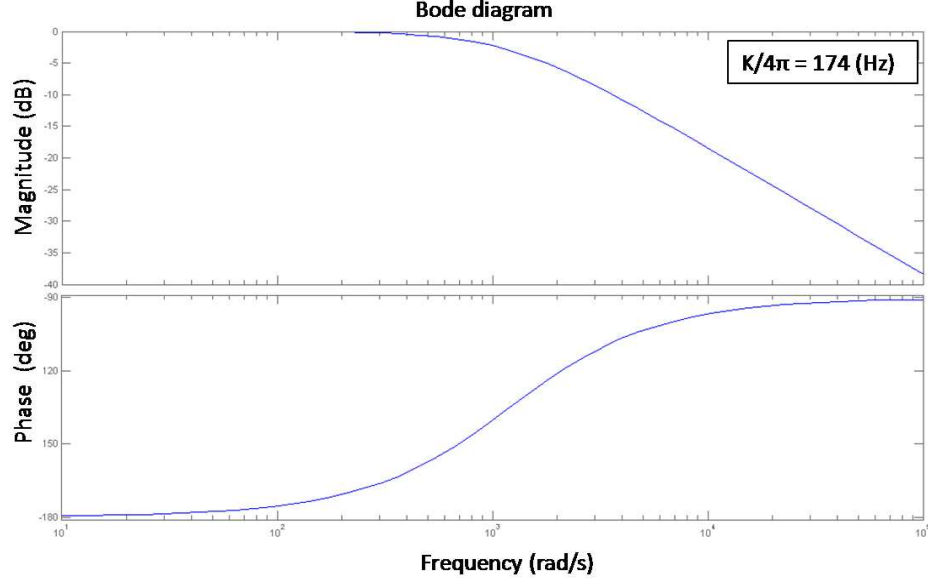
Figure 4.7: Bode diagram of reflection coefficient R

After the reflection coefficient has been obtained analytically for this simple case, the implemented NSCBC algorithm is used to reproduce numerically these theoretical results. The computational setup is similar to that already adopted by Selle et al. [118] for the same analysis.

The semi-infinite duct condition cannot be reproduced directly hence the domain length is assumed finite and a non-reflecting inlet is used at the left boundary. Relaxation coefficients for assuring non-reflectivity of inlet are calculated using the procedure of Yoo et al. [140]. As the flow is one dimensional only two incoming waves exist: $\mathcal{L}_5$ and $\mathcal{L}_2$; the respective relaxation coefficients for LRM are reported in Table 4.6.

Obtained results are plotted not as a function of frequency but as a function of pressure relaxation coefficient σ_p. Two procedures have been adopted for evaluating wave amplitude variations:

σ_{u1}	$0.278 \cdot \rho c^2 \frac{1-Ma^2}{2L}$	$47000 \, [kg/(s^2 \cdot m^2)]$
σ_T	$-0.278 \cdot \frac{\rho R}{cL}$	$0.58 \, [kg \cdot s/(m^3 \cdot K)]$

Table 4.6: Relaxation coefficients adopted for modeling a non-reflecting inlet (from Yoo et al. [140])

- Values for both entering and leaving acoustic waves are extrapolated from the internal domain; results reported in Fig. 4.8.

- Values actually used in the integration of NSCBC procedure, hence extrapolated value for the leaving acoustic wave $\mathcal{L}_1$ and LRM value for the incoming acoustic wave $\mathcal{L}_5$; results reported in Fig. 4.9.
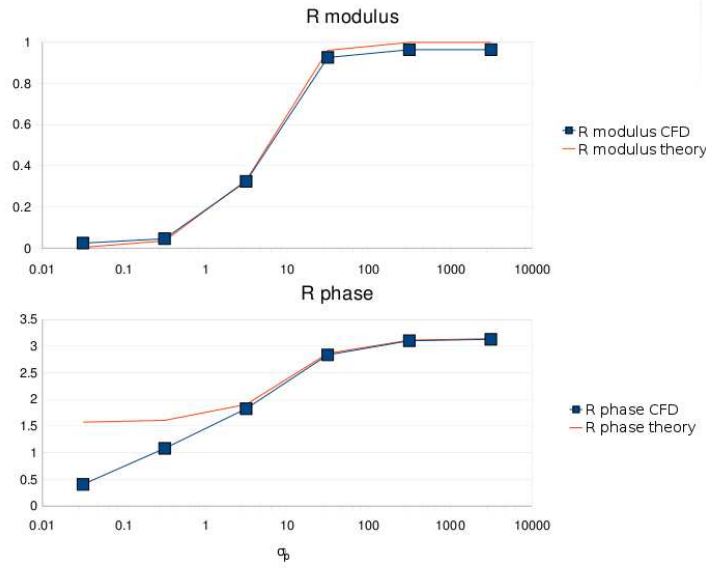
Figure 4.8: Reflection coefficient obtained with $\mathcal{L}_1$ and $\mathcal{L}_5$ extrapolated

Agreement in the latter case, with wave amplitude variations as imposed in the computations, are really good, both for modulus and phase of reflection coefficient predictions. The predictions for the extrapolated wave amplitude
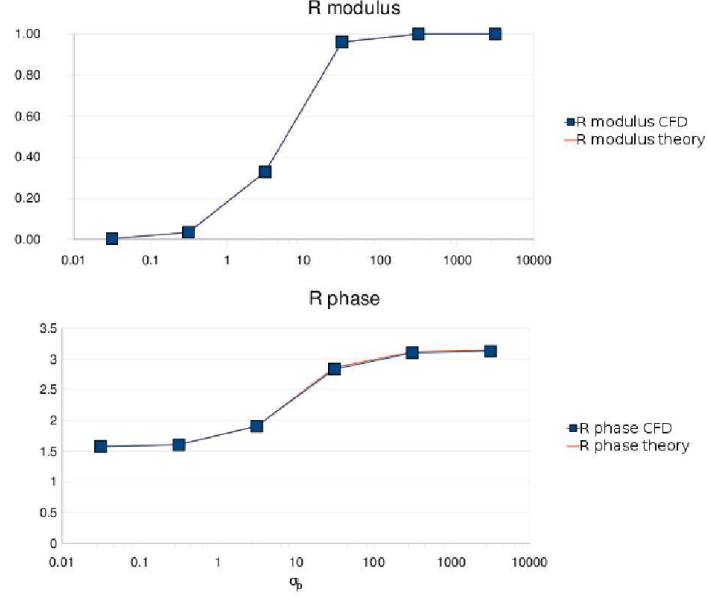
Figure 4.9: Reflection coefficient obtained with $\mathcal{L}_1$ extrapolated and $\mathcal{L}_5$ from LRM

variations case do not fully agree with the theoretical results for the phase, especially for low values of the relaxation coefficient ($\sigma < \pi$). As it will be demonstrated in the next part of this test case analysis, this range is not useful anyway for the purpose of modelling non-reflecting outlets.

4.3.2.2 Natural response of a LRM outlet

In this second test case an analysis of the transient response of a system similar to that in the previous section is considered to evaluate the capability of the outlet section to evacuate acoustically closed duct modes.

This configuration corresponds to an imposed inlet temperature and velocity (hard inflow conditions) and a fixed outlet pressure. Acoustic waves present inside this kind of domain are not able to exit from neither the inlet nor the outlet boundary, thus any initial perturbation oscillates ideally without damping in the case of Eulerian flow. The eigenfrequencies of this system

can be easily found solving the acoustic equations with the above mentioned boundary conditions for inlet and outlet:

$$\nabla^2(p') - \frac{1}{c_0^2}\frac{\partial^2 p'}{\partial^2 t} = 0 \tag{4.41}$$

or the equivalent Helmholtz equation in the frequency domain:

$$\nabla^2(p'_\omega) + k^2 p'_\omega = 0 \quad , \quad k = \omega/c_0 \tag{4.42}$$

The only difference compared to the previous test lies in the inlet modelling, now considered as a reflecting inlet boundary. The initial flow field is not uniform and acquires importance in this case. An initial impulsive acoustic perturbation is imposed, as suggested by Baum et al.[20], in the following form:

$$u = u_0 + A \cdot exp\left[-\left(\beta\frac{x}{L}\right)^2\right] \tag{4.43}$$

$$p = p_0 \pm \rho_0 u_0 \left(u - u_0\right) \tag{4.44}$$

$$\rho = \rho_0 \pm \frac{\rho_0 \left(u - u_0\right)}{c_0} \tag{4.45}$$

A and β determine the strength and the stiffness of the superimposed acoustic wave. The choice of sign in the equations for p and ρ determines the direction in which the acoustic wave will propagate. In this case a rightgoing perturbation is superimposed and A and β are given values 50 and 5000 respectively.

Such quite stiff acoustic perturbation is imposed in order to excite as much acoustic modes of the duct as possible. The acoustic pressure signal at the inlet section and its spectra with acoustically closed duct eigenfrequencies are reported for three different values of the relaxation coefficient σ_p, namely π, 10π and 100π.

$\sigma_p = \pi.$ From Eq. 4.40, this case corresponds to a cut-off frequency equal to that of the first duct mode: the quarter wave mode. Thus it is expected that this mode will be adequately evacuated from the LRM outlet. The pressure signal and its spectrum are reported in Fig.4.10 and 4.11.
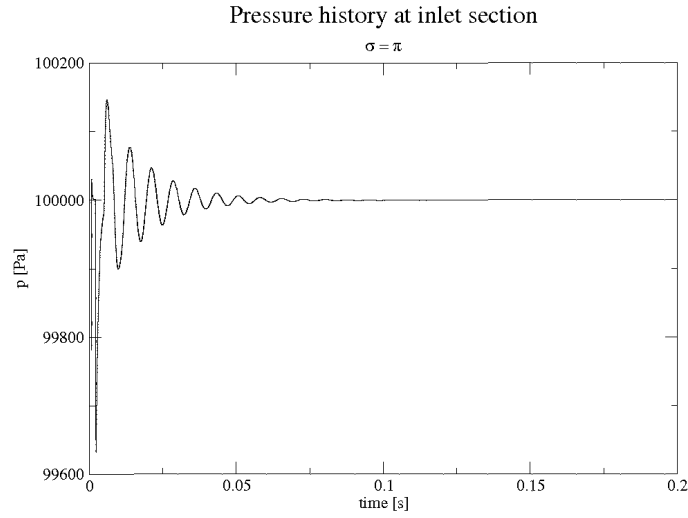
Figure 4.10: Pressure history at inlet section for the case $\sigma_p = \pi$

The initial perturbation disappears before t=0.1 s, corresponding to about 35 cycles of wave oscillations in the duct. The acoustic behaviour of the system is quite different from that of the acoustically closed duct. In fact, as shown in Fig.4.11, the natural frequencies of the system are shifted towards lower values, and the peaks drastically decrease for natural frequencies lower than that of the first mode.

$\sigma_p = 10\pi.$ The pressure signal in this case is very different from the previous case, as the spectra amplitude reported in Fig.4.13 shows. Natural frequencies of the system are closer to those of the acoustically closed duct. Moreover at t=0.2 s the first mode of the duct is still strongly present inside

Pressure spectra for inlet section
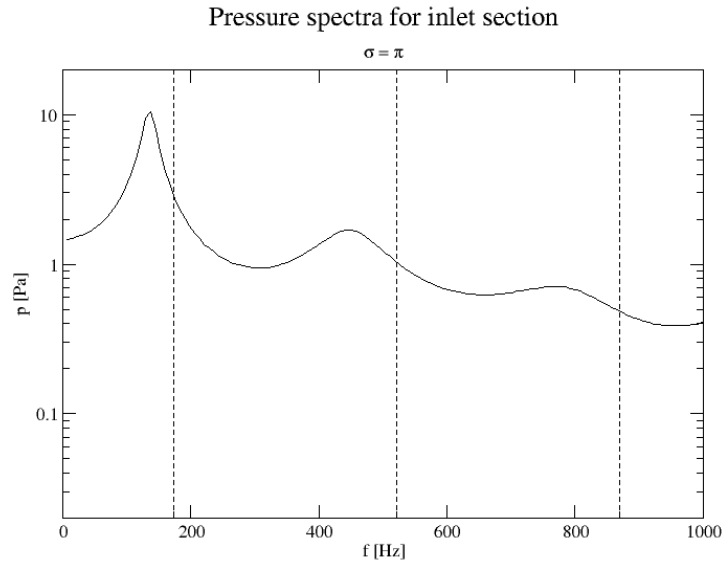
Figure 4.11: Pressure amplitude spectra at the inlet section for the case $\sigma_p = \pi$

Pressure history at inlet section
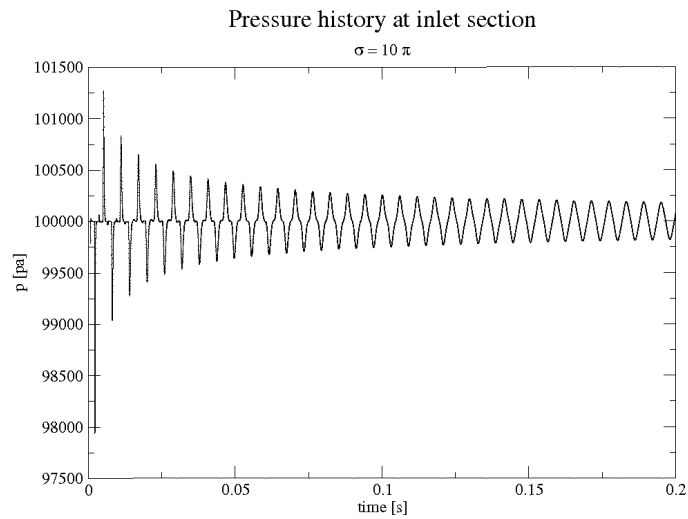
Figure 4.12: Pressure history at inlet section for the case $\sigma_p = 10\pi$
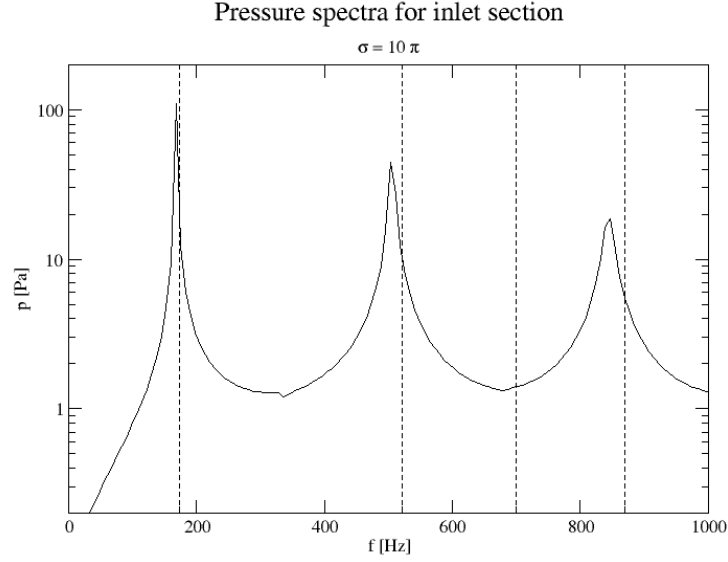
Figure 4.13: Pressure amplitude spectra at the inlet section for the case $\sigma_p = 10\pi$

the domain, see Fig.4.12.

$\sigma_p = 100\pi$. This last case is reported demonstrating the strong reflectivity of such a high relaxation coefficient for LRM outlet. In fact, as the pressure history in Fig.4.14 shows, impulsive initial perturbation preserves its form up to t=0.1 s. The pressure spectrum at the inlet, see Fig.4.15, shows that the natural frequencies coincide with acoustically closed duct and even the three quarter wave mode preserves a high energy content. Antiresonances similar to those of lowly damped mechanical systems is encountered between each natural frequency.
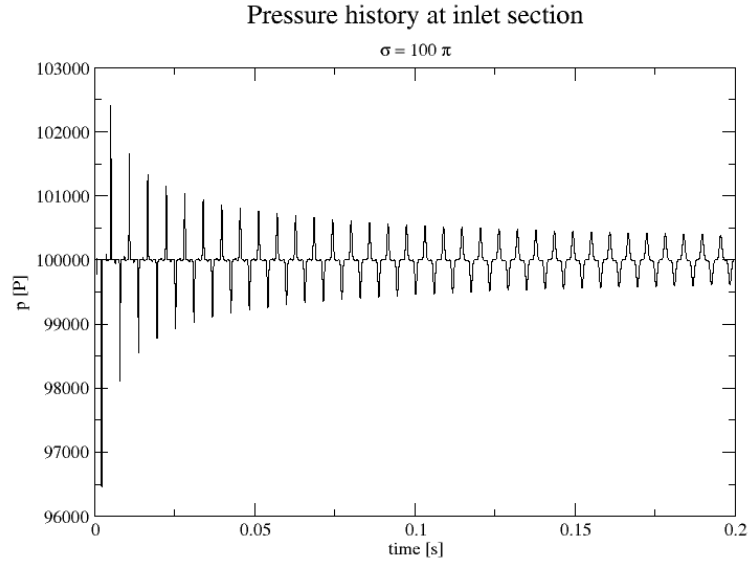
Figure 4.14: Pressure history at the inlet section for the case $\sigma_p = 100\pi$
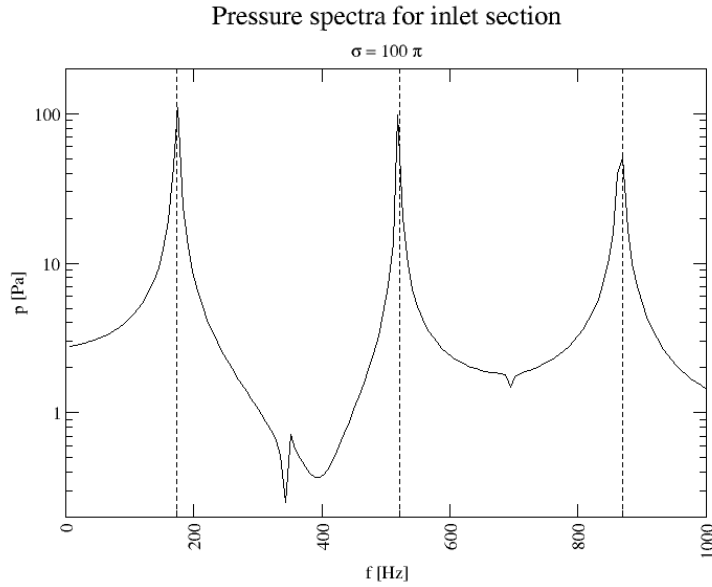
Figure 4.15: Pressure amplitude spectra at the inlet section for the case $\sigma_p = 100\pi$

### 4.3.2.3 Summary of the findings

The test case of 1D flow with LRM outlet has allowed us to evaluate the effective reflection coefficient of non-reflective outlet implemented with the NSCBC technique. Moreover an optimum value for the relaxation coefficient σ_p has been found: $\sigma_p = \pi$ was demonstrated to represent a good choice for modelling non-reflective outlets. As Selle et al. [118] suggested lower values may cause drifts in the mean pressure and higher values may generate an unacceptable reflectivity of the outlet. Particular attention will be focused on the characteristic length L, which will be chosen as a representative length of the acoustical properties of the domain.

4.3.3 Convected vortex

This test case presents a 2D vortex superimposed on a uniform free stream flow with viscous fluid involved. The setup is the same as adopted by Yoo et al. [141], and already tested by Poinsot and Lele [107] for smaller vortex strength.

The initial vortex is prescribed as:

$$\begin{pmatrix} u \\ v \end{pmatrix} = \begin{pmatrix} u_\infty \\ 0 \end{pmatrix} + \begin{pmatrix} \frac{\partial \psi}{\partial y} \\ -\frac{\partial \psi}{\partial x} \end{pmatrix} \tag{4.46}$$

where ψ is the stream function for an incompressible inviscid vortex:

$$\psi = C \cdot exp \left(-\frac{(x - x_0)^2 + (y - y_0)^2}{2 r_c^2} \right) \tag{4.47}$$

x_0, y_0 are the coordinates of the vortex center, C is the vortex strength and R_c is the vortex radius. The initial pressure field, calculated from potential analysis, is given by:

$$p = p_\infty - \rho_\infty \left(\frac{C}{r_c} \right)^2 exp \left(-\frac{(x - x_0)^2 + (y - y_0)^2}{r R_c^2} \right) \tag{4.48}$$

.

The boundary conditions adopted are reported in Table 4.7, together with the relaxation coefficients for the LRM treatment for both inlet and outlet. Viscous conditions SI-4 and B3 (see Tables 4.2 and 4.3) are applied respectively for inlet and outlet.

Inlet	non-reflecting inlet ($\sigma_{u1} = 980000, \sigma_{u2} = 192000, \sigma_T = -135$)
Outlet	non-reflecting outlet ($\sigma_p = \pi$)
Sides	cyclic

Table 4.7: Boundary conditions for the convected vortex problem

The results are reported in terms of isocontour of horizontal velocity and normal vorticity component in Fig. 4.16 and 4.17 respectively.

The NSCBC show a good non reflecting behaviour: the velocity field is not altered passing through the outlet boundary. The horizontal velocity component is accelerated near the boundary, showing the known tendency of sucking-out the vortex. Yoo et al. [140] attributed this effect of LRM boundary to the approximations made in the LODI hypothesis. Assuming the flow one-dimensional near the boundary becomes a weak assumption in the case of strong gradients, as in this case. A locally altered vorticity field in the interaction with the outlet in Fig. 4.17 is an effect of the unnatural acceleration effect on the outlet. Yoo et al. [140] proposed a new method for calculating characteristic wave amplitude variations on the outlet which relaxes the hypothesis of local one-dimensional flow. Simulations conducted by them show a better agreement with expected results from a perfectly non-reflecting boundary. This level of non reflectivity was however considered satisfactory for the applications of interests, thus this latter proposal by Yoo et al. was not taken into account. More details on the validation test cases
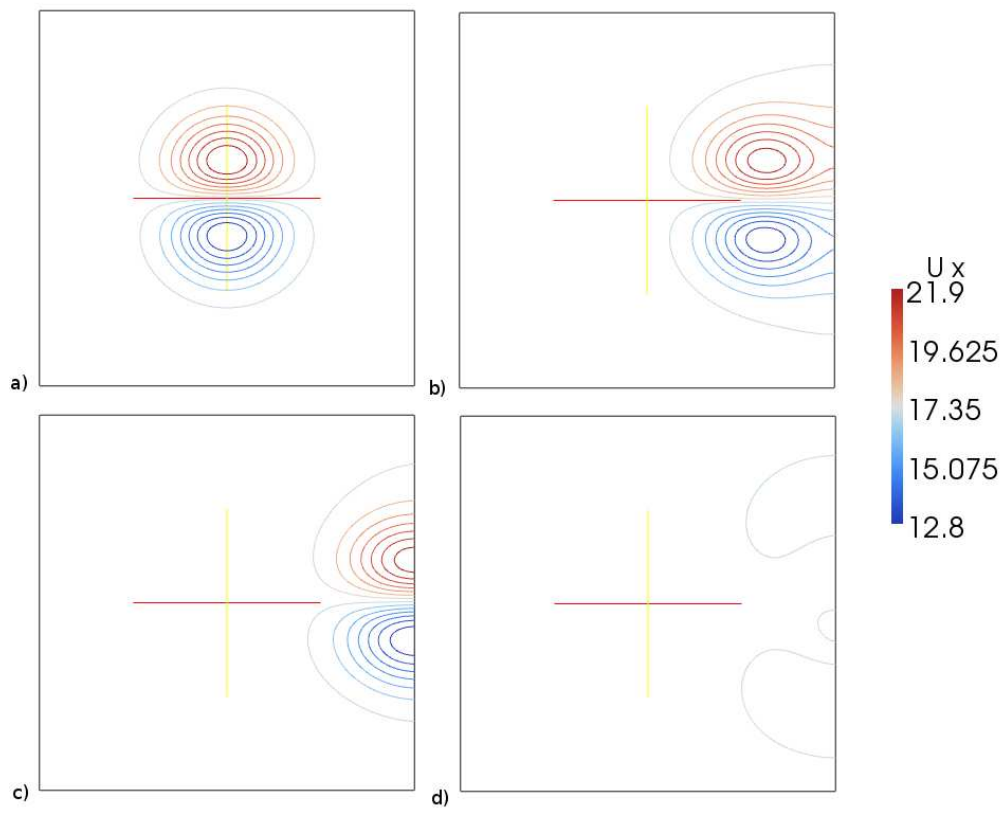
Figure 4.16: Horizontal velocity component isocontours at different time-steps: $a = 0\mu s$, $b = 36\mu s$, $c = 56\mu s$, $d = 72\mu s$
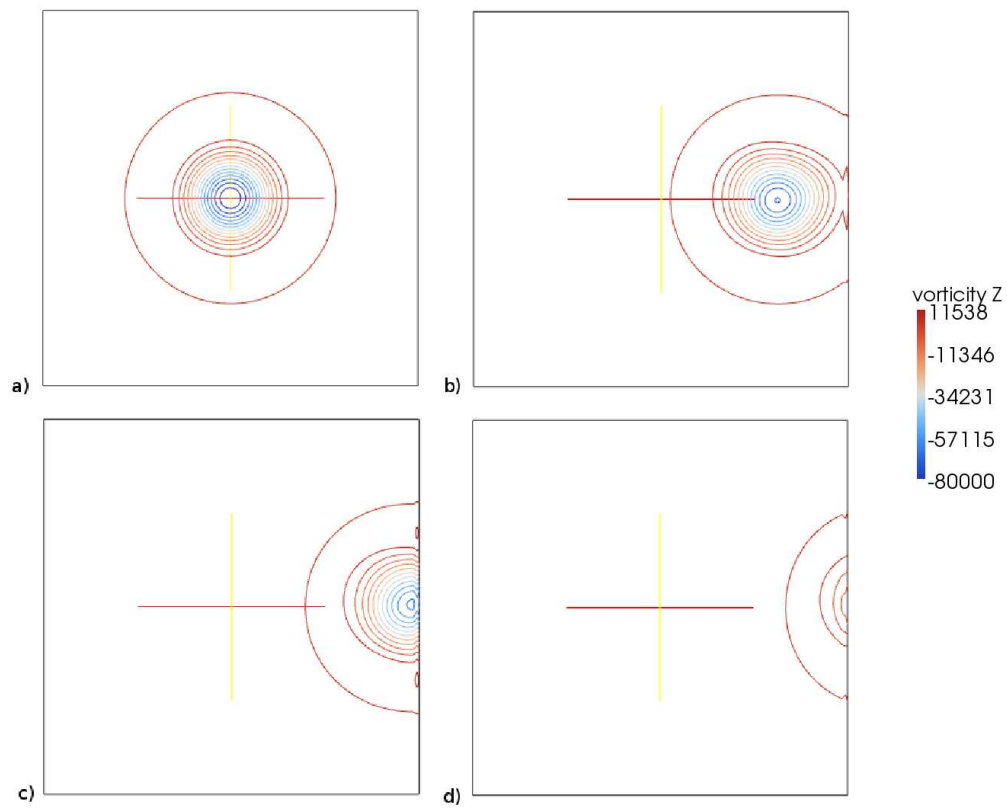
Figure 4.17: Normal vorticity component isocontours at different time-steps: $a = 0\mu s,\ b = 36\mu s,\ c = 56\mu s,\ d = 72\mu s$

are reported in [56].

4.4 Acoustic impedance of perforated plates

4.4.1 Technological application and physical principles

Multi-perforated liners are commonly used in gas turbine combustion systems to reduce wall temperature within limits established by the mechanical characteristics of materials. The correct evaluation of acoustic damping connected with such devices allows the design of gas turbine combustor cooling systems to reduce the propagation of pressure fluctuations due to thermo-acoustic instabilities. Such passive dampers become particularly attractive for aero-engines because they permit the improvement of the acoustic damping properties of the combustor system without any increase in weight. Furthermore with the expected future regulations concerning NOx emissions for civil aero-engines, lean burn combustors will sooner or later be implemented by manufacturers, increasing the criticality of acoustic damping to avoid possible blow outs.

4.4.2 Acoustic impedance and reflection coefficient

The acoustic behaviour of a passive termination can be described through its impedance Z, the ratio in the frequency domain between acoustic pressure and acoustic velocity normal to the plate:

$$Z(\mathbf{x}, \omega) = \frac{P(\mathbf{x}, \omega)}{\mathbf{U}(\mathbf{x}, \omega) \cdot \mathbf{n}_S} = \mathscr{R}(\mathbf{x}, \omega) + j \mathscr{X}(\mathbf{x}, \omega) \tag{4.49}$$

where $\mathbf{x}$ is a generic point on the surface and $\mathbf{n}_S$ is the unit normal vector pointing into the surface; $P(\mathbf{x}, \omega)$ and $\mathbf{U}(\mathbf{x}, \omega)$ are the Fourier transforms of acoustic pressure and acoustic velocity, respectively. The impedance defined

(a) Reference scheme

(b) Progressive and regressive waves
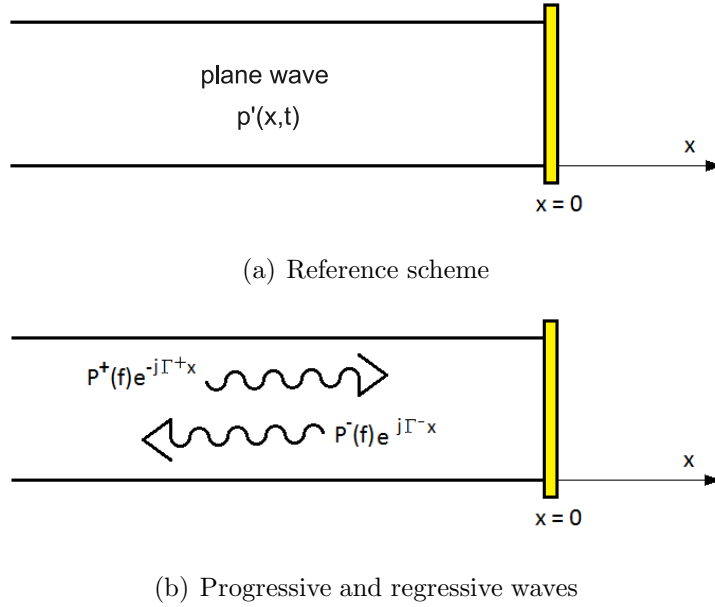
Figure 4.18: Acoustic field in a duct

in this way is a complex number: the real part is called *resistance* whilst the imaginary part is called *reactance*.

Let us consider a duct with a screen (for example a perforated plate) placed at $x = 0$ (Fig. 4.4.2). According to Eq. 4.49 the impedance is a function of the position on the screen surface. However at low frequencies and at a sufficient distance from the plate a plane wave approximation is applicable[1] [109] and so the acoustic propagation can be treated with a 1-dimensional model and the acoustic behaviour of the screen can be simply represented by single impedance global values.

The plane wave approximation allows us to decompose the acoustic pressure field into the sum of a progressive wave and a regressive running one as depicted in Fig. 4.4.2. In the frequency domain the sound field can be

---

[1]The direction of propagation of the plane wave is parallel to the duct axis.
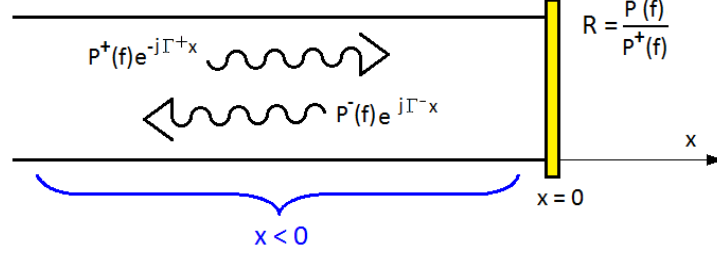
Figure 4.19: Reflection coefficient

expressed as [79]:

$$P(x, f) = P^+(f)e^{-j\Gamma^+ x} + P^-(f)e^{j\Gamma^- x} \qquad (4.50)$$

where $P(x, f)$ is the frequency spectrum at the generic location x whereas $P^-(f)$ and $P^+(f)$ are the spectra of the regressive and progressive running waves. The superscript $+$ denotes the wave that moves towards the screen whilst the symbol $-$ is assigned to the wave that travels in the opposite direction. Γ^+ and Γ^- are the wave propagation constants (see Sec. 4.4.3 for details).

The *reflection coefficient* of the screen is defined as the ratio in the frequency domain between the reflected wave and the incident wave at $x = 0$ (the position of the screen):

$$R(f) = \frac{P^-(f)}{P^+(f)} \qquad (4.51)$$

The reflection coefficient is related to the screen impedance by the relation [109]:

$$R(f) = \frac{Z(f) - \rho_0 c_0}{Z(f) + \rho_0 c_0} \qquad (4.52)$$

where c_0 is the speed of sound and ρ_0 is the density of the reference medium. Thus, once $R(f)$ is known, $Z(f)$ can be easily found. Like the impedance, the
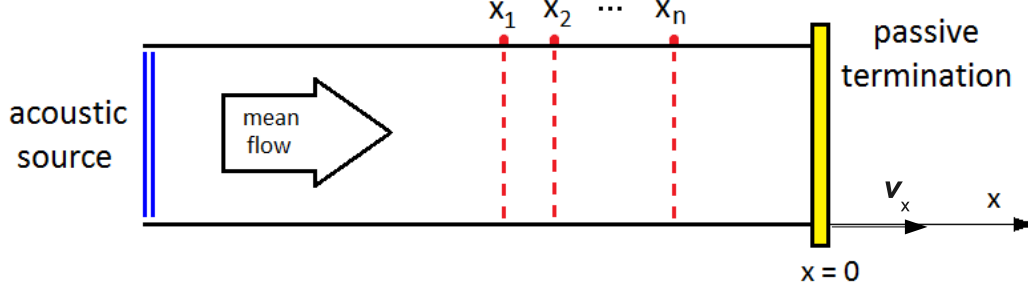
Figure 4.20: Multiple microphone method, reference scheme

reflection coefficient is a complex number. Its magnitude is often represented in terms of the *absorption coefficient* given by:

$$A(f) = 1 - |R(f)|^2 \tag{4.53}$$

4.4.3   Multiple microphone method

The multi-microphone method [79] is presented here as a measuring technique to determine the reflection coefficient of a passive termination based on a plane wave approximation. The reference scheme is depicted in Fig. 4.20: the passive termination is located at one end of a duct and the pressure field is measured at n different locations along the duct. The reflection coefficient is computed starting from the pressure samples recorded at these locations. The general case of an acoustic field in the presence of a mean flow is considered.

Following Eq. 4.50, the frequency domain representation of the acoustic field at a generic sensor position x_i can be written as:

$$P(x_i, f) = P_i(f) = P^+(f)e^{-j\Gamma^+ x_i} + P^-(f)e^{j\Gamma^- x_i} \tag{4.54}$$

By applying Eq. 4.54 to all the n sensors, a linear system can be obtained. The system can be arranged in a matrix form:

$$\mathbf{MP} = \mathbf{b} \tag{4.55}$$

where:

$$\mathbf{M} = \begin{bmatrix} \exp(-j\Gamma^+x_1) & \exp(j\Gamma^-x_1) \\ \exp(-j\Gamma^+x_2) & \exp(j\Gamma^-x_2) \\ \vdots & \vdots \\ \exp(-j\Gamma^+x_n) & \exp(j\Gamma^-x_n) \end{bmatrix}$$

$$\mathbf{P} = \left\{ \begin{array}{c} P^+(f) \\ P^-(f) \end{array} \right\}, \qquad \mathbf{b} = \left\{ \begin{array}{c} P_1(f) \\ P_2(f) \\ \vdots \\ P_n(f) \end{array} \right\}$$

(4.56)

The unknowns are represented by the vector $\mathbf{P}$ which contains the Fourier transforms of the left and right running waves. In contrast, the vector $\mathbf{b}$ is computed using the pressure data recorded at the sensor locations as detailed in Sec. 4.4.4. In the multi-microphone method the number of sensors is usually greater than two and so the linear system in Eq. 4.55 is overdetermined. A least-squares solution can be found by means of the pseudoinverse matrix (see App. C). Therefore $\mathbf{P}$ is given by:

$$\mathbf{P} = \mathbf{M}^\dagger \mathbf{b} = (\mathbf{M}^H \mathbf{M})^{-1} \mathbf{M}^H \mathbf{b}$$

(4.57)

Finally, the reflection coefficient is computed by means of Eq. 4.51.

4.4.4 Post-processing of recorded pressures

In both experiments and numerical simulations the pressure signal recorded at each sampling position is represented by a set of N time samples corresponding to the number of samples contained in the observation window T_0. In other words the pressure field at the generic sensor location x_i is

represented by a discrete signal:

$$\tilde{p}\,(x_i, kT) \qquad k = 1, 2, \ldots, N$$

The acoustic fluctuations are given by:

$$\tilde{p}'\,(x_i, kT) = \tilde{p}\,(x_i, kT) - p_0 \qquad k = 1, 2, \ldots, N$$

where p_0 is the reference pressure and N is the same for all the locations (it is assumed that the same number of time samples has been recorded at each location). In order to obtain the vector $\mathbf{b}$, we have to determine the n Fourier transforms $P_i(f)$ starting from the sampled pressures. A discrete approximation of the frequency spectrum can be found using the DFT but a procedure based on DFT is heavily influenced by the typical errors (in particular aliasing and leakage) that characterize this mathematical tool.

However, when the acoustic field is an harmonic perturbation and the frequency of acoustic fluctuations is known (e.g. sinusoidal forcing term) a more accurate method can be used: each component $P_i(f)$ of the vector $\mathbf{b}$ can be determined using a *sinusoidal least-squares fit*. This procedure can be applied when the acoustic field consists of a simple harmonic plane wave or a sum of harmonic plane waves with different frequencies. In practice a sinusoidal function is imposed at each sampling location:

$$p'(x_i, t) = \Phi_i \sin(\omega t + \varphi_i) = c_{s,i} \sin(\omega t) + c_{c,i} \cos(\omega t) \tag{4.58}$$

where

$$\Phi_i = \sqrt{c_{s,i}^2 + c_{c,i}^2},$$
$$\tag{4.59}$$
$$\varphi_i = \arctan(c_{c,i}, c_{s,i}).$$

The coefficients $c_{s,i}$ and $c_{c,i}$ are computed by minimizing the *distance* between the sinusoidal function and the time samples. In the particular case

of the least-squares method the distance is given by:

$$\mathscr{D}_i = \left\{ \sum_{k=1}^{N} \left[c_{s,i} \sin(\omega kT) + c_{c,i} \cos(\omega kT) - \tilde{p}'(x_i, kT) \right]^2 \right\}^{1/2} \tag{4.60}$$

$\mathscr{D}_i$ can also be expressed in a matrix form:

$$\mathscr{D}_i = \|\mathbf{A}_i \mathbf{c}_i - \mathbf{s}_i\| \tag{4.61}$$

where:

$$\mathbf{A}_i = \begin{bmatrix} \sin(\omega 1T) & \cos(\omega 1T) \\ \sin(\omega 2T) & \cos(\omega 2T) \\ \vdots & \vdots \\ \sin(\omega NT) & \cos(\omega NT) \end{bmatrix} \tag{4.62}$$

$$\mathbf{c}_i = \left\{ \begin{array}{c} c_{s,i} \\ c_{c,i} \end{array} \right\} \qquad \mathbf{s}_i = \left\{ \begin{array}{c} \tilde{p}'(x_i, 1T) \\ \tilde{p}'(x_i, 2T) \\ \vdots \\ \tilde{p}'(x_i, NT) \end{array} \right\}$$

If the following overdetermined system is considered:

$$\mathbf{A}_i \mathbf{c}_i = \mathbf{s}_i \tag{4.63}$$

the vector $\mathbf{c}_i$ that minimizes the distance $\|\mathbf{A}_i \mathbf{c}_i - \mathbf{s}_i\|$ can be directly computed using the pseudoinverse matrix[2] (see App. C):

$$\mathbf{c}_i = \mathbf{A}_i^{\dagger} \mathbf{s}_i = (\mathbf{A}_i^T \mathbf{A}_i)^{-1} \mathbf{A}_i^T \mathbf{s}_i \tag{4.64}$$

Once $\mathbf{c}_i$ is determined at each sensor location, the pressure signals are reconstructed by means of Eq. 4.58. An equivalent signal can be written in the

---

[2]Note that the elements of the systems are real numbers and so in definition C.2 the Hermitian transpose $\mathbf{A}^H$ can be replaced with the classical transpose matrix $\mathbf{A}^T$.

frequency domain exploiting the relationship:

$$P_i(f) = \Phi_i(f)e^{j\varphi_i(f)}. \tag{4.65}$$

Then, the vector $\mathbf{b}$ is assembled and $P^+(f)$ and $P^-(f)$ are calculated by means of Eq. 4.57 and so it is possible to compute the reflection coefficient as previously described. The entire procedure is schematically represented in Fig. 4.21.

Eq. 4.64 can be easily extended to the case of an acoustic perturbation given by a sum of M sinusoidal functions. The acoustic field at every sensor location is given by[3]:

$$p'(x_i, t) = \sum_{k=1}^{M} \Phi_i^{(k)} \sin(\omega_k t + \varphi_i^{(k)}) = \sum_{k=1}^{M} \left[c_{s,i}^{(k)} \sin(\omega_k t) + c_{c,i}^{(k)} \cos(\omega_k t) \right] \tag{4.66}$$

The matrix $\mathbf{A}_i$ and the vectors $\mathbf{c}_i$ and $\mathbf{s}_i$ of the system in Eq. 4.63 become:

$$
\mathbf{A}_i =
\begin{bmatrix}
\sin(\omega_1 1T) & \cos(\omega_1 1T) & \dots & \sin(\omega_M 1T) & \cos(\omega_M 1T) \\
\sin(\omega_1 2T) & \cos(\omega_1 2T) & \dots & \sin(\omega_M 2T) & \cos(\omega_M 2T) \\
\vdots & \vdots & \vdots & \vdots & \vdots \\
\sin(\omega_1 NT) & \cos(\omega_1 NT) & \dots & \sin(\omega_M NT) & \cos(\omega_M NT)
\end{bmatrix}
$$

$$
\mathbf{c}_i =
\begin{Bmatrix}
c_{s,i}^{(1)} \\
c_{c,i}^{(1)} \\
c_{s,i}^{(2)} \\
c_{c,i}^{(2)} \\
\vdots \\
c_{s,i}^{(M)} \\
c_{c,i}^{(M)}
\end{Bmatrix}
\qquad
\mathbf{s}_i =
\begin{Bmatrix}
\tilde{p}'(x_i, 1T) \\
\tilde{p}'(x_i, 2T) \\
\vdots \\
\tilde{p}'(x_i, NT)
\end{Bmatrix}
\tag{4.67}
$$

---

[3]The superscript (k) denotes the k-th harmonic component.
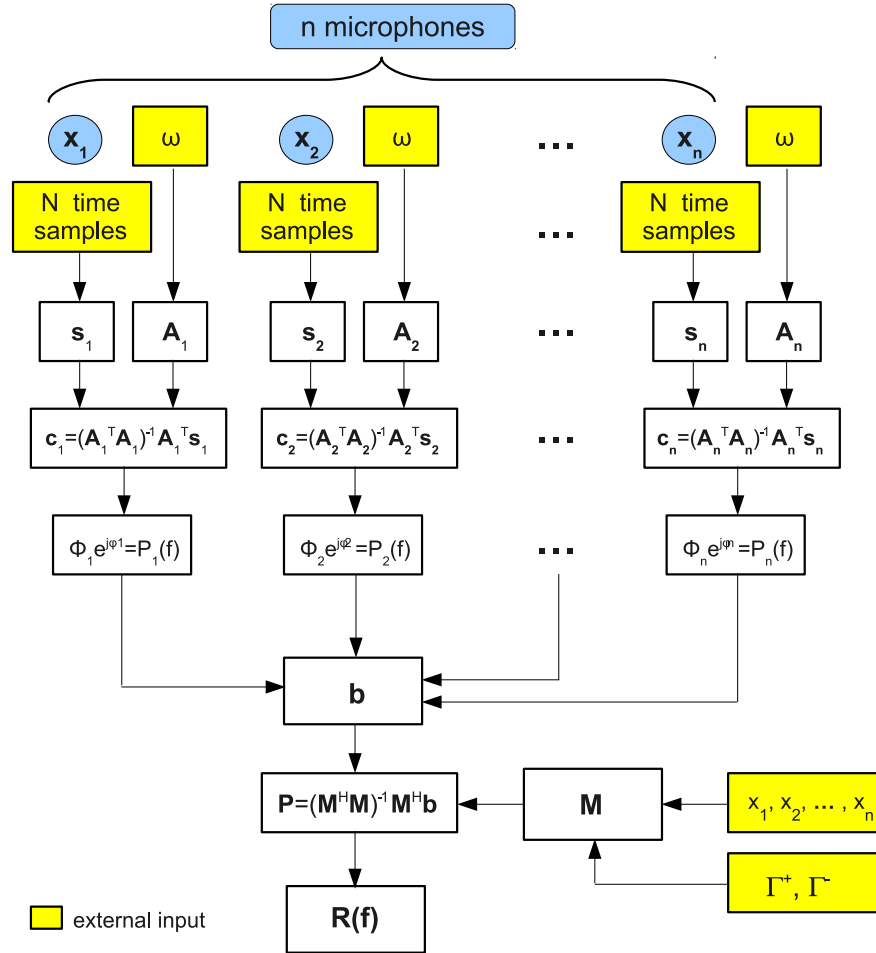
Figure 4.21: Multiple microphone method based on sinusoidal least-squares fit

Eq. 4.64 allows us to find the M pairs[4] $(c_{s,i}^{(k)}, c_{c,i}^{(k)})$ which can be converted in amplitude and phase of the respective sinusoidal functions by means of relations 4.59. The value of the reflection coefficient is computed by considering each frequency separately. More details on the implemented pressure signal post processing can be found in [55].

---

[4]From a mathematical point of view, it should be noted that Eq. 4.64 is applicable if and only if $2M \leq N$.

4.4.4.1   Wave propagation constants

The wave propagation constants Γ^+ and Γ^- can be defined, see [79] as:

$$\Gamma^+ = \frac{(\kappa - j\delta)}{1 + Ma}$$

$$(4.68)$$

$$\Gamma^- = \frac{(\kappa - j\delta)}{1 - Ma}$$

where κ is the wave number ($\kappa = \omega/c_0$) and Ma is the mean flow Mach number.

Finally δ is the attenuation constant which originates from viscothermal and turbulent effects that characterize the flow field (see references [75, 79, 98] for its computation).

If the Mach number and the attenuation constant are negligible, a simplified expression can be used:

$$\Gamma^+ = \Gamma^- = \kappa \qquad (4.69)$$

4.4.5   Bellucci Test Case

The numerical tools presented were validated against the experimental and numerical work of Bellucci [24]. The same set of experimental data was used by Mendez [94] to validate similar LES computations. Experimental data as well as finite element analysis computed with the Howe model assumption [120, 121] are reported for comparison.

The reference test case is composed of a thin multi-perforated screen with a bias flow and a normal to the screen acoustic wave. Amplitude of excitation is chosen as to remain in the linear regime for which no effect of amplitude of the forcing is detected. The assumption of flow periodicity around the holes is made to simplify the computational domain as depicted in Fig. 4.22 to simulate a single orifice.
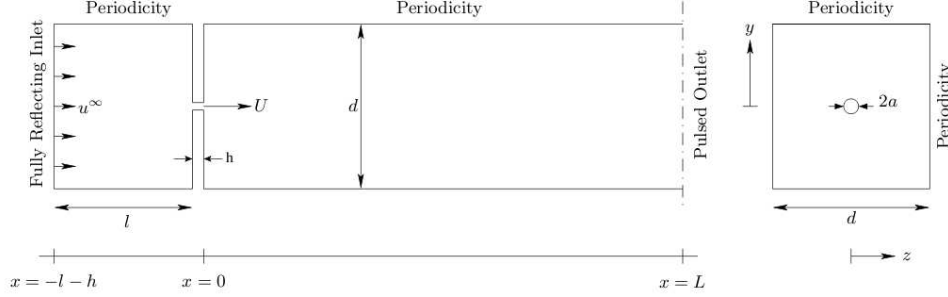
Figure 4.22: Computational domain (from Dassé et al. [44])

Inlet and outlet boundaries are treated with the NSCBC approach (see Sec. 4.1.3). The inlet boundary is modelled as a hard-inflow boundary condition in such a way as to reproduce the fully reflecting acoustic behaviour of the experimental back wall. To assess the acoustic response of the system, harmonic oscillations (the equivalent of experimental speakers) are imposed at the outlet. LRM has been adopted with a sinusoidal reference pressure given by:

$$p_{ref} = p_{out,mean} + \Phi \sin(2\pi f t) \tag{4.70}$$

where f is the frequency of the harmonic perturbation. Main geometrical parameters and flow conditions are reported in Table 4.8.

Results are presented in terms of absorption coefficient and phase of reflection coefficient as function of excitation frequency.

As shown in Fig. 4.23, the agreement between experiments and numerical predictions is substantially good for the absorption coefficient. All the investigations predict a very similar behaviour characterized by the presence of a maximum at which A is close to unity (the incident acoustic wave is almost completely absorbed by the system) around 400 Hz. Concerning peak frequency, the LES computation slightly over-predicts such value with respect to both FEM and experiments. Away from the absorption peak, the LES

Geometrical characteristics	
$S_x = S_y$	35 mm
D_h	6 mm
σ	0.0231
h	1.5 mm
Flow conditions	
U_b	5.0 m/s
T_∞	293.15 K
p_∞	100000 Pa
Φ	5 Pa

Table 4.8: Geometrical characteristics and flow conditions - Bellucci test case

computations underpredict experimental values much more than the original Howe model implemented in the FEM both at higher and lower frequencies.

Fig. 4.24 plots the phase of reflection coefficient. The first thing to note is the different behavior of LES predictions compared to both experiments and FEM analysis in the proximity of the maximum of the absorption co-efficient. The change in sign of the phase occurs at the frequency at which the maximum of the absorption coefficient is located. Even though the frequency is quite well captured by the three computations, the LES switch from a negative to a positive phase shift passing from $-\pi$ to π while the FEM computations and experiments progressively reduce the shift achieving zero corresponding to the maximum. When the absorption coefficient is almost unitary the regressive pressure wave amplitude is almost null and it is easier to mispredict the phase of such wave. These findings were also reported in [94] for equivalent LES computations. A more complete discussion
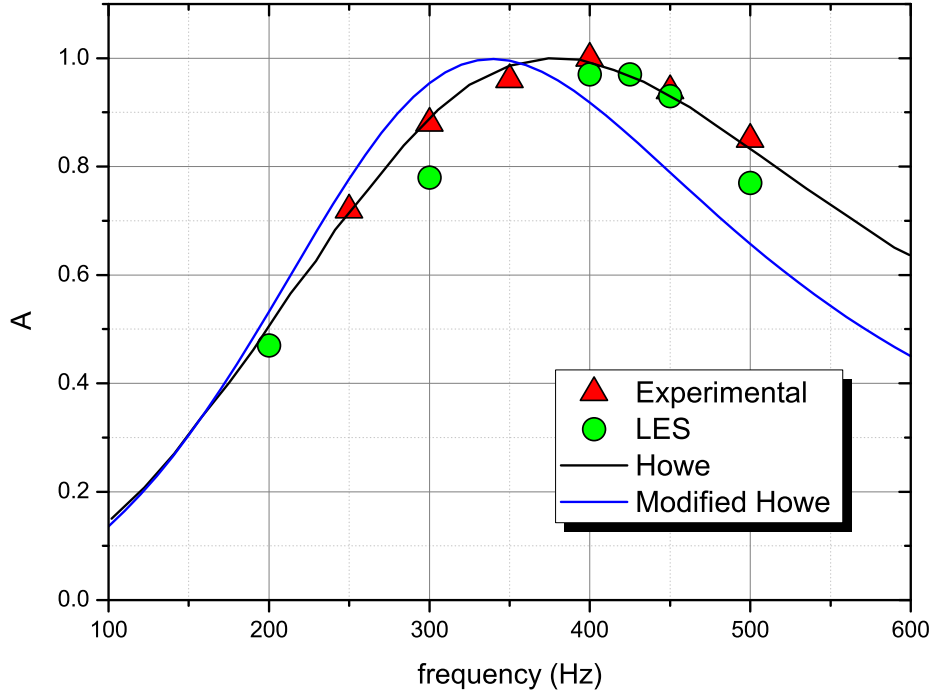
Figure 4.23: Absorption coefficient - Bellucci test case

of the obtained results is reported in [55].

4.4.6 KIAI Test Case

A similar computation as the case presented in the previous section,i.e. 90 deg angled in-line holes and no grazing flow, was performed at the reference conditions for the test matrix proposed for the ongoing experimental project inside the KIAI EU project [112, 120]. The same setup and boundary conditions apply also for this case with different geometrical details and flow conditions as summarized in Table 4.9.

The investigated range of frequencies is confined between 550 and 1300 Hz with steps of 150 Hz. Even though lower frequencies were of interest as well, the high computational cost of longer simulation periods limited the
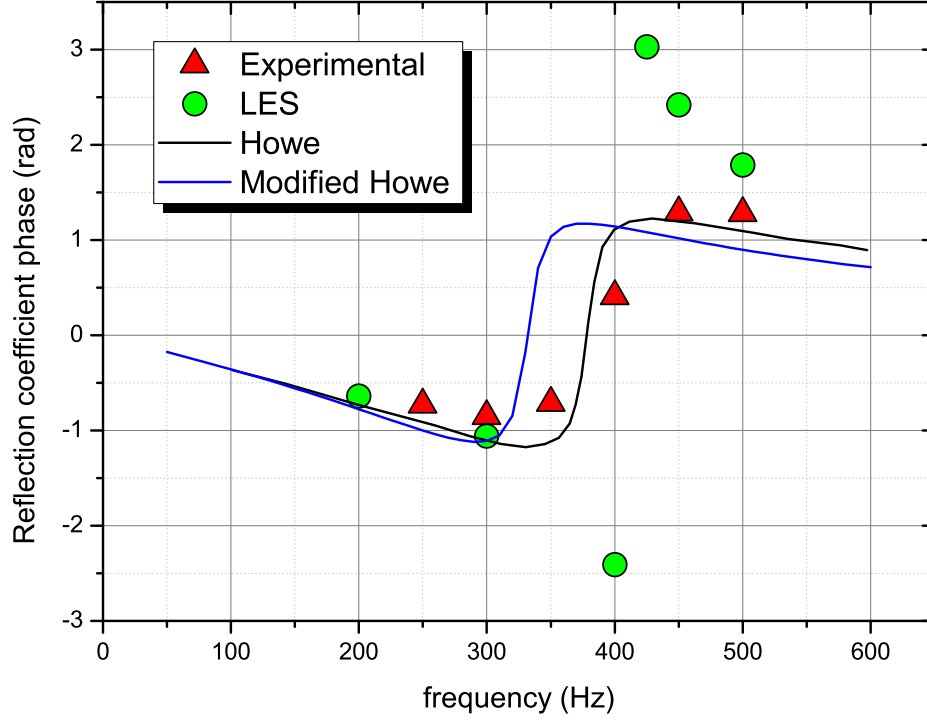
Figure 4.24: Reflection coefficient phase - Bellucci test case

evaluation of such values. Forcing terms at the outflow boundary included all frequencies involved at the same time:

$$p_{ref} = p_{out,mean} + \sum \Phi_i \sin(2\pi f_i t). \tag{4.71}$$

The amplitudes of excitation Phi_i were distinguished, maintaining linear regime, from 10 to 40 Pa corresponding to 114 and 126 dB, for the various frequencies in order to maximize the acoustic and aerodynamic decoupling of the multi-frequency excitation and reduce the total simulation time.

Concerning the computational costs in fact a total period of 30 cycles at 500 Hz corresponds to 0.06 s. The computational grid, composed of nearly $700 \cdot 10^3$ cells, imposes a fixed time step of $5 \cdot 10^{-7}$ s to guarantee $Co < 0.5$ resulting in a total number of iterations of 300000 iterations, completed in

Geometrical characteristics	
S_x	7.3 mm
S_y	5.9 mm
D_h	0.8 mm
h	2.5 mm
Flow conditions	
Ma	0.1
T_∞	293.15 K
p_∞	100000 Pa

Table 4.9: Geometrical characteristics and flow conditions - KIAI test case

280 CPU hours of parallel run circa on a 3.00GHz quad core Intel Xeon X5472.

The results obtained are reported in Fig.4.25 in terms of absorption coefficient and compared with FEM predictions with the Howe model. Neither prediction shows a strong dependency on frequency; the values lie between 0.2 and 0.25; with LES results resulting to be slightly higher than those for the acoustic finite element solver. The gap between the two is growing with frequency, however it is still confined around 10% and the trend is quite well reproduced.

An attempt to investigate the effect of staggering was performed changing the domain and the periodicity definition. Fig. 4.26 shows a comparison between the in-line arrangement in Fig. 4.26(c) and two different approaches to cope with hole staggering. The first one implements a diamond shaped domain with standard cyclic boundaries on the corresponding side of the rhomboid, as depicted in Fig. 4.26(a). In the second one, see Fig. 4.26(b) the staggered condition is achieved doubling the distance of the streamwise
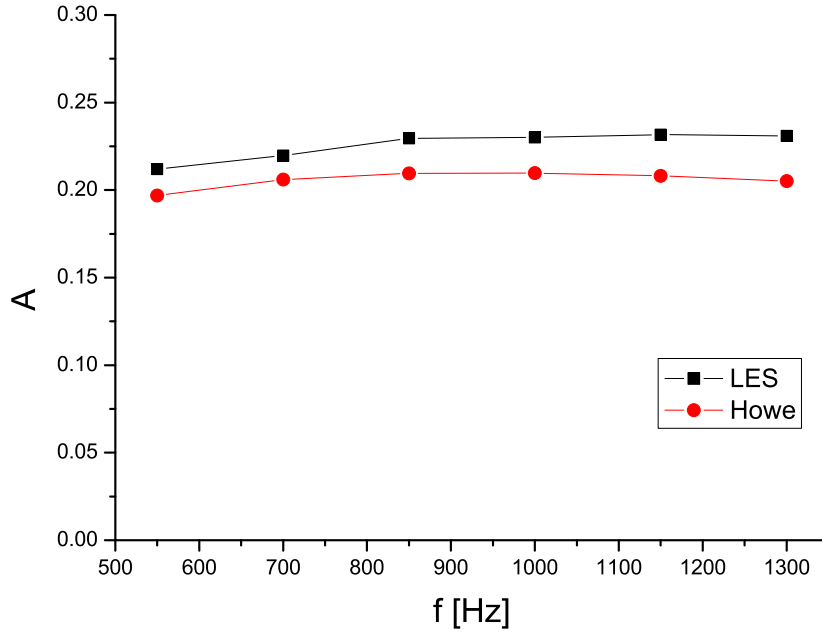
Figure 4.25: Absorption coefficient - KIAI test case

cyclics and halving the tangential one. Furthermore the tangentially periodic boundary is cut into two identical sectors and cross-paired.

Experiences with the rhomboidal domain are reported in several works [48, 87, 96], however due to the high axial to tangential pitch ratio of this test case a set up based on the diamond domain would have created too highly skewed elements with an hexahedral mesh. The second approach was thus chosen for this work to maintain highly orthogonal cells. Inclusion of a grid refinement close to the stream-wise boundary was necessary in order to maintain a element size approximately equal on the corresponding sides of the domain.

The acoustic simulation to assess the effect of staggering was conducted at 1300 Hz and compared with equivalent analysis performed with the FEM code. The staggered holes reduce the absorption coefficient as predicted by

(a) Staggered Rhomboidal domain   (b) Staggered Rectangular domain
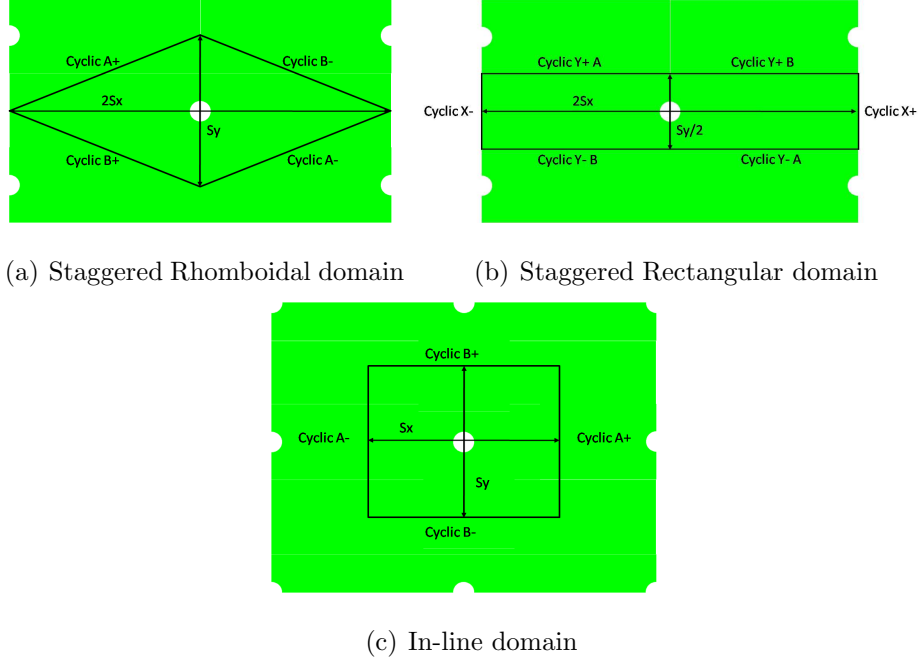
(c) In-line domain

Figure 4.26: Domain definitions

both codes even though the LES predictions reveal a much stronger dependency on the arrangement of the holes. The higher absorption for the in-line configuration in fact is inverted into an under-prediction for the staggered arrangement.

4.4.6.1 Flow field analysis

In order to better understand the fluid dynamic mechanism through which acoustic energy is dissipated across the hole, an analysis of the flow field of the naturally excited jet was performed taking advantage of the very high level of detail released by LES computations. This is relevant for the acoustic analysis, since the investigated range of forcing largely reside in the linear regime, as long as the selected frequencies are far from those associated with the natural modes of the jet.
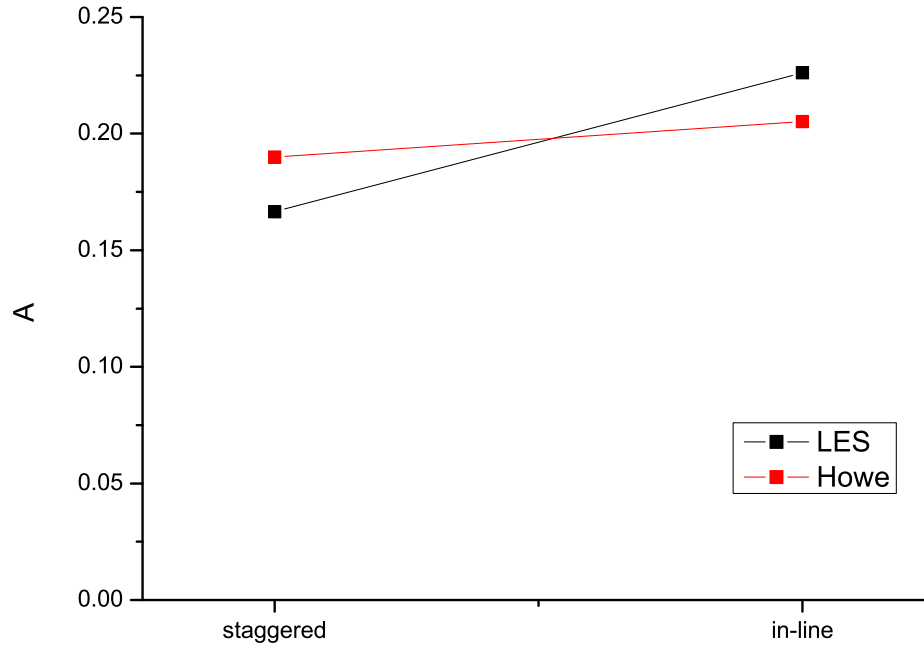
Figure 4.27: Absorption coefficient - Effect of staggering

An analysis of the flow field of the naturally excited jet was performed. An overview of the flow field on the symmetry plane is given in Fig. 4.28 reporting a contour plot of the instantaneous and the mean axial velocity.

Even though experimental data were not available to directly compare the numerical predictions, main flow structures of the free jet can be recognized in the instantaneous velocity field to validate the turbulent jet behaviour. Due to the long L/D ratio, no vena contracta can be appreciated in the potential core. Spatial resolution was not sufficient to directly resolve the Kelvin-Helmoltz instability structures developing on the margin of the potential core, anyhow turbulent transition and the progressive diffusion into a fully developed core is captured. The time averaged velocity plot is also shown in order to assess the mean extension of the jet inside the domain, small asymmetries in the profile are due to the shortness of the simulation period.
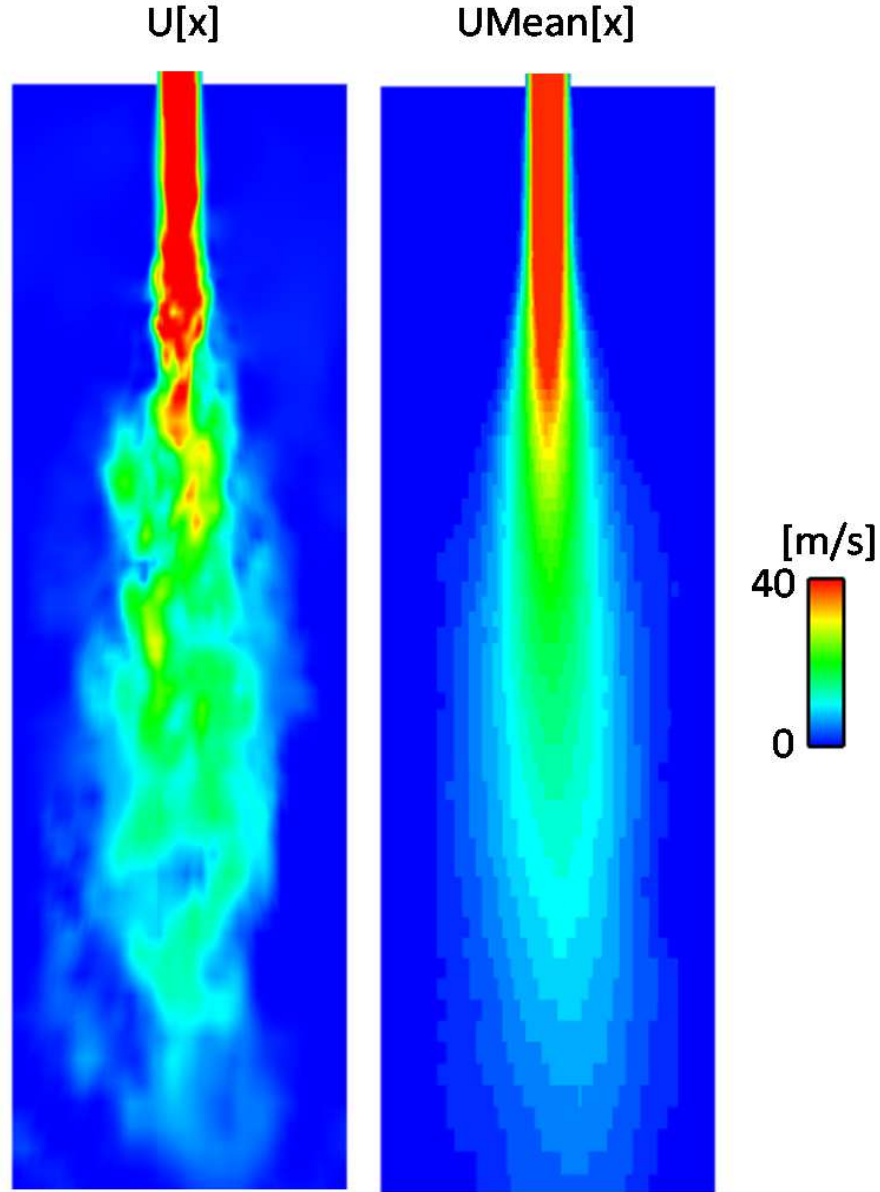
Figure 4.28: Instantanous and mean axial velocity

A Proper Orthogonal Decomposition (POD), see App. D, has been conducted to investigate the near hole flow more in detail. A region inside the box extending $2.5 \cdot D_h$ in the jet direction and $2 \cdot D_h$ in the span direction

was selected to compute such modal analysis. Both the velocity and pressure modes were investigated on 340 snapshots equally spaced in time over a period T=4.08 ms.

The velocity analysis results were shown to be less spatially defined compared to the pressure one due to the interaction of the different velocity component on the same mode. The first pressure modes are analysed here and corresponding velocity modes are just exploited to understand the flow field associated with the pressure mode themselves. Since the acoustic energy, corresponding to the pressure decomposition, and the kinetic energy, relative to the velocity analysis, are not equivalent, corresponding modes might be found at different positions in the mode energy ranking. Spectral analysis and compatibility of pressure and velocity fields allowed the establishment of a connection between the most energetic, in both senses, modes.

The first mode is equivalent to the mean pressure field thus it is not presented. The following modes usually present equivalent but symmetric counterparts, for example mode 2 and 4 have inverse pressure distributions respectively at mode 3 and 5, not reported for the sake of brevity. Fig. 4.29 shows the pressure distribution on the symmetry plane aligned with the axial pitch for modes 2 and 4. The corresponding velocity modes demonstrate that those structures correspond to co-rotating and counter rotating vortices respectively on the same symmetry plane. Three dimensional isosurfaces reveal that mode 2 corresponds to vortex rings aligned with the hole axis while mode 4 connects two misaligned co-rotating lobes on the two sides of the hole. The order of the corresponding velocity modes is inverted being respectively the 5th and the 3rd modes, meaning that the kinetic energy content is actually higher for the misaligned vortex rings.

The relative kinetic energy content is a fundamental parameter in order to
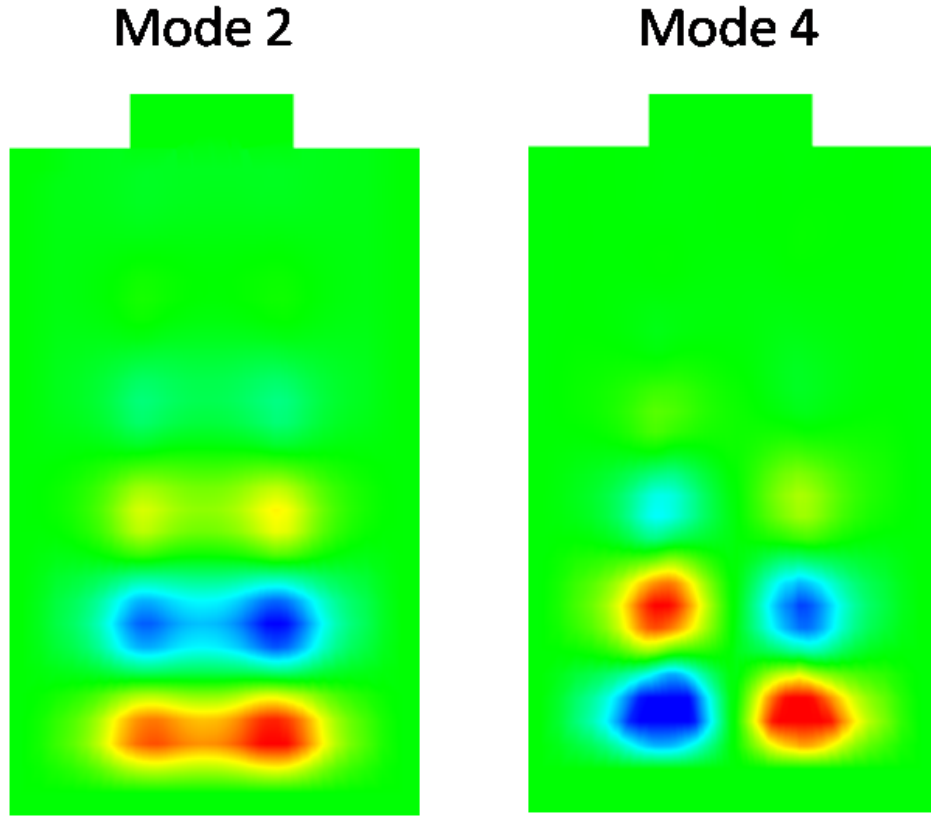
Figure 4.29: Pressure POD modes 2 and 4

estimate the weight of each mode in the global solution and how many modes are necessary to completely describe the flow. It was computed from the eigenvalue associated with the given velocity mode representing the energy contained in the mode itself. Fig. 4.30 shows the relative fluctuating energy content of the first 21 modes except the first, associated with the mean flow and thus excluded from the fluctuating energy computation. All these first 20 modes present an energy content above 1%, with first 6 modes ranging between 7 and 3.5%. These findings are in line with POD of experiments for a natural circular jet at Re = 6700 as reported in [132].

The temporal coefficients for pressure modes 2 to 5 were later analysed
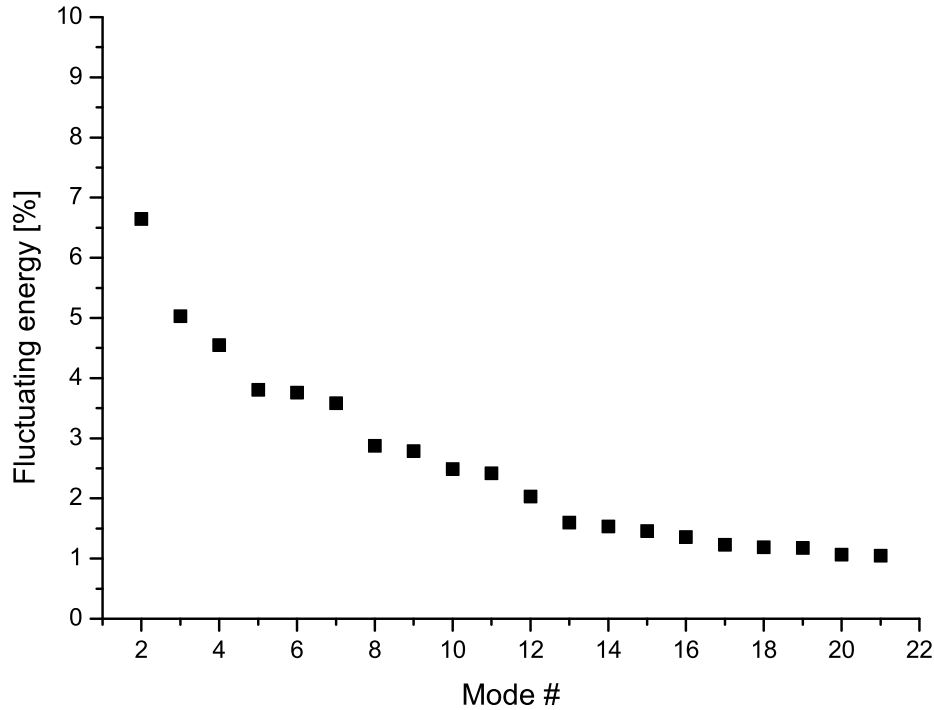
Figure 4.30: Fluctuating kinetic energy distribution of first 20 modes

in order to assess the dominating frequencies by means of a Discrete Fourier Transform. The investigated range of frequencies goes up to 41000 Hz with a resolution of 245 Hz. Modes 2 and 3 reveal an almost coincident spectrum showing a clear peak at 24800 Hz, as shown in Fig. 4.31. The same analysis conducted for modes 4 and 5 highlights the same parallel behaviour of the coupled modes and shows a more spread spectrum with excited frequencies ranging between 15000 and 28000 Hz.

Those values report that the characteristic frequencies of the jet and of the acoustic forcing are largely separated thus the hypothesis of flow field independence from the sinusoidal pressure waves is confirmed. As a matter of fact the flow field in the acoustic simulation is reproducing the same modes as in the natural jet and most of the unsteady effects at the investigated
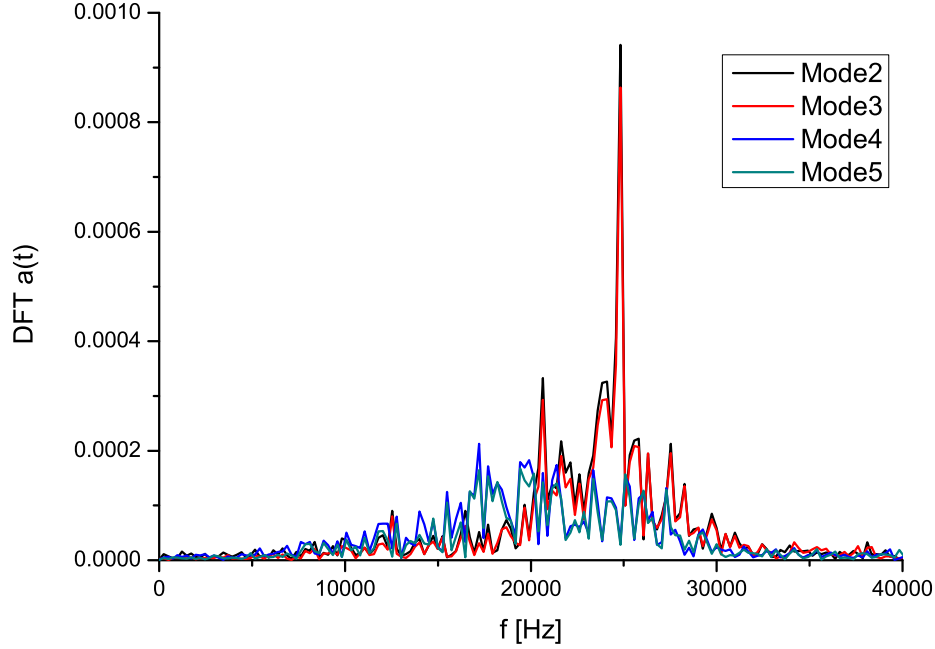
Figure 4.31: Discrete Fourier Transform of first 4 pressure modes time coefficients

frequencies are connected with the temporal coefficients of the first mode representing a waving mean velocity. The natural frequencies of these first modes are hence pretty far from the investigated frequency range allowing the assumption of independence of such modes from the acoustic forcing.

4.5 Concluding remarks

Large Eddy Simulation was successfully exploited to predict the global acoustic properties of multi-perforated plates. In order to achieve this, reflectivity of inflow and outflow boundary was minimized by means of the Navier-Stokes Characteristic Boundary Conditions. Linear Relaxation Method was employed to maintain desired mean flow inside the domain. Pure tone and multifrequency acoustic excitation was superposed to the mean outlet pres-

sure to verify the reflection coefficient of the plate.

Results showed good agreement with equivalent computations performed with research codes and other computational acoustic techniques both for simple literature test case and for engine-like conditions. A modal decomposition of the flow field permitted the investigation of the characteristic Strouhal number of the principal modes showing how the free jet frequencies are quite far from the excited frequency range.

Chapter 5

Summary and Conclusions

This chapter summarizes the entire work, starting from the context and the aims of the research and going through the main achievements obtained. Conclusions are then drawn with respect to the scopes of the thesis. Finally a road map for possible further improvements for the computational approaches to numerically study combustor cooling systems is presented.

5.1   Context and aims

With the recently introduced regulations on pollutant emissions for aeroengines, major manufacturers had to move towards the lean premixed combustion technology. This introduces a significant reduction of air available for cooling purposes which designers needs to face seeking for more and more efficient (and coolant saving) combustor cooling devices.

Furthermore the stability of the flame is deeply decreased and strong pressure fluctuations are generated within the combustor by an inhomogeneous heat release. The beneficial role of the perforated plates employed in cooling systems in the damping of such acoustic fluctuations can be taken

into account to avoid use of heavy and large additional acoustic dampers.

Accurate and reliable numerical simulations of the heat transfer and the acoustic properties of the cooling systems are hence fundamental to assist the design of such components. The success of advanced computational techniques in predicting these phenomena strongly relies on the provision of adequate boundary conditions. An assessment of "optimal" boundary conditions is therefore proposed to evaluate possible enhancements of the fidelity of such predictions.

5.2   Main achievements

A 3-dimensional numerical study of the heat transfer and acoustics of combustor cooling devices, such as impingement and effusion systems, was performed with an open-source CFD code exploiting conjugate heat transfer analysis and Large Eddy Simulations.

In order to align the OpenFOAM®code to the most advanced research codes for this kind of applications, three different boundary conditions were implemented in such a computational environment. The first one is an implicitly coupled non conformal interface to solve for conjugate heat transfer, the second is an auto-recycling turbulent inlet generator with feedback to maintain prescribed mean flow field while the third one is a non and partially reflecting boundary conditions with the possibility to include acoustic forcing known as the Navier-Stokes Characteristic Boundary Conditions (NSCBC).

The capabilities of those boundary conditions to improve the accuracy of predictions with respect to standard procedures were tested under conditions relevant for combustor cooling system design. A conjugate heat transfer analysis of a multiperforated plate with highly inclined conventional and

shaped holes for effusion cooling was performed at engine like flow conditions. Overall effectiveness was computed for both a cold and a hot simulation reproducing corresponding experimental test rig configurations.

An axisymmetric impingement jet with heat transfer, for which a detailed database of mean velocity and fluctuation measurements was available, was simulated exploiting LES turbulence treatment to test the potentiality of auto-recycling turbulent inlet for heat transfer analysis. The test chosen represents relevant conditions for combustor impingement cooling: Re=23000 and H/D =2.

Finally, the acoustic behavior of multiperforated plates with bias flow was studied, first following literature test cases and then at higher bias Ma to reproduce relevant geometrical and flow conditions compared to the perforated screens implemented in aeroengines combustors, to help the acoustic design of such passive dampers for the thermoacoustic instabilities.

5.3 Conclusions

The implemented conditions showed results aligned with the "state of the art" for these kind of computations. The open-source code OpenFOAM® chosen as a platform was found to be as effective as the most advanced research codes for the computation of the heat transfer and aeroacoustics of the gas turbine combustor cooling systems and proved to be accurate and fast enough for the purpose of this work.

In particular for the conjugate effusion simulations the key factors for correctly predicting the overall effectiveness are a proper modelling of the heat sink effect and the correct set up of the metal sheet conditions at the fluid inlet and outlet. Accurate predictions of the heat exchange between

coolant and metal can be achieved only by means of a fine discretization also far from the wall at the duct entrance. Of the two geometries considered, the conventional and the shaped holes one, only the latter showed a sufficient agreement with available experiments concerning the spanwise averaged overall effectiveness. For this configuration, even though maintaining the same porosity and the same slanted angle, all the above mentioned factors resulted less critical due to the larger hydraulic diameter of the hole and the relatively higher numbers of hole included in the computational domain.

Concerning the impingement jet, the auto mapped technique proved its capability in the generation of turbulent inflow conditions. The flow field, both mean velocities and radial fluctuations, proved to be quite well predicted up to two diameters from the jet axis where the tangential grid resolution was fine enough. More uncertainties were found monitoring axial and cross fluctuations that, although much smaller compared to the radial one, might have a relevant impact on heat transfer since they are responsible for the mixing between hot fluid grazing the plate and the fresh coolant above. Even though the secondary peak in Nusselt number (around r/D = 2) was not reproduced, possibly due to the too short averaging time and to the increasing coarsening of the mesh for r/D > 2, the primary peak in the stagnation region is well captured.

The NSCBC showed very good non reflecting behavior in simple cases where such properties could be quantitatively and qualitatively evaluated. The acoustic forcing implemented also exhibited good non reflecting capabilities as predictions obtained for the absorption coefficient of multiperforated plates are in-line with both experiments and other numerical techniques as demonstrated on a literature test case. Application to conditions more consistent with combustor cooling devices, higher bias Mach and lower porosity,

showed limited acoustic absorption also at 90°. Spectral analysis evidenced how the characteristic range of flame frequencies are largely below the proper St of the column jet mode thus reporting an almost total insensitivity to excitation frequency.

5.4 Proposal for future works

Further work on the proposed boundary conditions should be directed towards the enhancement of the parallel efficiency of the conjugate interface and the NSCBC. Some stability issues of the NSCBC in presence of adjacent walls need to be further investigated as well as techniques to shorten the transient development of the flow when subject to mapped inflow conditions. Moreover the NSCBC for solid wall should be implemented to make the pressure wave reflection more physical considering both adiabatic and given temperature wall thermal conditions.

Anyhow a fundamental step to help combustor cooling system designers would be the development of homogeneous models to deal with the thermal as well as with the aeroacoustic effects of the effusion plates. Such boundary condition would avoid the highly costly computing of the huge number of holes present on a real combustor, making feasible the simulation of the entire cooling and combustion systems.

On the other hand, these models result to be efficient only if they can reproduce a wide range of conditions thus needs to be tested and tuned on wide databases of geometries and conditions available from experiments and/or numerical computations. That is why single hole bi-periodic simulations, such as those presented in Ch. 4, should be expanded to include the effect of crossflow. In order to guarantee an adequate fluid flow also in

presence of a streamwise periodic pressure field, source terms should be included in the momentum equation to drive the main flow. The inclusion of this effect is indeed necessary when real effusion holes, i.e. tilt angle different from 90°, are employed.

Appendix A

Characteristic form of Navier-Stokes equations

Neglecting volume forces, equations 4.1:4.5 may be conveniently recast in vectorial form:

$$\frac{\partial \widetilde{U}}{\partial t} + \frac{\partial \widetilde{F^i}}{\partial x_i} + \frac{\partial \widetilde{D^i}}{\partial x_i} = 0 \tag{A.1}$$

$\widetilde{U}$ is the vector of conservative variables $|\rho \ \rho u_1 \ \rho u_2 \ \rho u_3 \ \rho E|$, $\widetilde{F^i}$ is the flux vector of conservative variables along x_i direction and $\widetilde{D^i}$ represents viscous and conductive terms. Here the expressions for $\widetilde{F^i}$ and $\widetilde{D^i}$ are reported:

$$\widetilde{F^i} = \begin{pmatrix} \rho u_i \\ \rho u_1 u_i + \delta_{1k} p \\ \rho u_2 u_i + \delta_{2k} p \\ \rho u_3 u_i + \delta_{3k} p \\ (\rho E + p) u_i \end{pmatrix} \quad , \quad \widetilde{D^i} = \begin{pmatrix} 0 \\ -\tau_{1i} \\ -\tau_{2i} \\ -\tau_{3i} \\ -u_j \tau_{ij} + q_i \end{pmatrix} \tag{A.2}$$

A vector of primitive variables $U = |\rho \ u_1 \ u_2 \ u_3 \ p|^T$ is defined; it is possible to recast Eq. A.2 in terms of primitive variables:

$$\frac{\partial U}{\partial t} + F^i \frac{\partial U}{\partial x_i} + D = 0 \tag{A.3}$$

F^i is the jacobian matrix relevant to the i-th direction and $D = P^{-1}\frac{\partial D^i}{\partial x_i}$ includes viscous and conductive terms. F^i reads:

$$F^i = \begin{pmatrix} u_i & \delta_{1i}\rho & \delta_{2i}\rho & \delta_{3i}\rho & 0 \\ 0 & u_i & 0 & 0 & \delta_{1i}/\rho \\ 0 & 0 & u_i & 0 & \delta_{2i}/\rho \\ 0 & 0 & 0 & u_i & \delta_{3i}/\rho \\ 0 & \delta_{1i}\gamma p & \delta_{2i}\gamma p & \delta_{3i}\gamma p & u_i \end{pmatrix} \tag{A.4}$$

$P = \partial \widetilde{U}/\partial U$, the jacobian matrix to switch between primitive and conservative variables:

$$P = \begin{pmatrix} 1 & 0 & 0 & 0 & 0 \\ u_1 & \rho & 0 & 0 & 0 \\ u_2 & 0 & \rho & 0 & 0 \\ u_3 & 0 & 0 & \rho & 0 \\ \frac{1}{2}u_k^2 & \rho u_1 & \rho u_2 & \rho u_3 & \frac{1}{\kappa} \end{pmatrix} \tag{A.5}$$

and its inverse P^{-1}:

$$P = \begin{pmatrix} 1 & 0 & 0 & 0 & 0 \\ -u_1/\rho & 1/\rho & 0 & 0 & 0 \\ -u_2/\rho & 0 & 1/\rho & 0 & 0 \\ -u_3/\rho & 0 & 0 & 1/\rho & 0 \\ \frac{\gamma-1}{2}u_k^2 & -(\gamma-1)u_1 & -(\gamma-1)u_2 & -(\gamma-1)u_3 & (\gamma-1) \end{pmatrix} . \tag{A.6}$$

F^i may be diagonalized giving:

$$S_i^{-1} F^i S_i = \Lambda^i \tag{A.7}$$

where the eigenvalues are the characteristic wave velocities:

$$\lambda_1^i = u_i - c \tag{A.8}$$

$$\lambda_2^i, \ \lambda_3^i, \ \lambda_4^i = u_i \tag{A.9}$$

$$\lambda_5^i = u_i + c \tag{A.10}$$

and S^i:

$$S_i = \begin{pmatrix} \frac{1}{2c^2} & \frac{\delta_{1i}}{c^2} & \frac{\delta_{2i}}{c^2} & \frac{\delta_{3i}}{c^2} & \frac{1}{c^2} \\ -\frac{\delta_{1i}}{2\rho c} & 1 - \delta_{1i} & 0 & 0 & \frac{\delta_{1i}}{2\rho c} \\ -\frac{\delta_{2i}}{2\rho c} & 0 & 1 - \delta_{2i} & 0 & \frac{\delta_{2i}}{2\rho c} \\ -\frac{\delta_{3i}}{2\rho c} & 0 & 0 & 1 - \delta_{3i} & \frac{\delta_{3i}}{2\rho c} \\ \frac{1}{2} & 0 & 0 & 0 & \frac{1}{2} \end{pmatrix} \tag{A.11}$$

If a boundary with normal x_1 is considered, the characteristic waves will be those traveling in the x_1 direction. Diagonalizing F^1 Eq.A.3 can be rewritten:

$$\frac{\partial U}{\partial t} + S_1 \Lambda^1 S_1^{-1} \frac{\partial U}{\partial x_1} + F^i \frac{\partial U}{\partial x_2} + F^i \frac{\partial U}{\partial x_3} + D = 0 \tag{A.12}$$

Λ^1 with eigen values:

$$\lambda_1 = u_1 - c, \ \lambda_2, \ \lambda_3, \ \lambda_4 = u_1, \ \lambda_5 = u_5 + c \tag{A.13}$$

It is now possible to define the characteristic wave amplitude variation vector $\mathcal{L} = \Lambda^1 S_1^{-1} \frac{\partial U}{\partial x_1}$:

$$\mathcal{L} = \begin{pmatrix} \lambda_1 \left(\frac{\partial p}{\partial x_1} - \rho c \frac{\partial u_1}{\partial x_1} \right) \\ \lambda_2 \left(c^2 \frac{\partial \rho}{\partial x_1} - \frac{\partial p}{\partial x_1} \right) \\ \lambda_3 \frac{\partial u_2}{\partial x_1} \\ \lambda_4 \frac{\partial u_3}{\partial x_1} \\ \lambda_5 \left(\frac{\partial p}{\partial x_1} + \rho c \frac{\partial u_1}{\partial x_1} \right) \end{pmatrix} \tag{A.14}$$

Eq.A.12 may be rewritten in terms of characteristic wave amplitude variations:

$$\frac{\partial U}{\partial t} + d + F^i \frac{\partial U}{\partial x_2} + F^i \frac{\partial U}{\partial x_3} + D = 0 \tag{A.15}$$

where

$$d = S_1 \mathcal{L} = \begin{pmatrix} \frac{1}{c^2} \left[\mathcal{L}_2 + \frac{1}{2} \left(\mathcal{L}_5 + \mathcal{L}_1 \right) \right] \\ \frac{1}{2\rho c} \left(\mathcal{L}_5 - \mathcal{L}_1 \right) \\ \mathcal{L}_3 \\ \mathcal{L}_4 \\ \frac{1}{2} \left(\mathcal{L}_5 + \mathcal{L}_1 \right) \end{pmatrix} \tag{A.16}$$

The conservative form of the diagonalized Navier-Stokes equations can be obtained by pre-multiplying the Eq. A.1 by P:

$$\frac{\partial \widetilde{U}}{\partial t} + Pd + \frac{\partial \widetilde{F^2}}{\partial x_2} + \frac{\partial \widetilde{F^3}}{\partial x_3} + \frac{\partial \widetilde{D^i}}{\partial x_i} = 0 \tag{A.17}$$

This equation is reported in its extensive form in Sec.4.1.1 when dealing with NSCBC. Neglecting viscous and conduction terms in Eq.A.15 the LODI relations are recovered.

Appendix B

Theoretical estimate of the relaxation coefficient for LRM

B.1 Non-reflecting inlet condition for normal velocity

An inlet boundary with normal x_1 and located at $x_1 = 0$ is considered. Following Strickwerda's [113] formulation for a non-reflecting outlet:

$$\frac{\partial p}{\partial t} - \overline{\rho c}\frac{\partial u}{\partial t} + K\left(p - \overline{p}\right) = 0 \tag{B.1}$$

a similar formulation for a non-reflecting inlet may be derived:

$$\frac{\partial p}{\partial t} + \overline{\rho c}\frac{\partial u}{\partial t} + \beta_5\left(u_1 - \overline{u_1^T}\right) = 0 \tag{B.2}$$

In Eqs. B.1 and B.2 the "$\overline{\bullet}$" operator represents time averaging; in the term $\beta_5\left(u_1 - \overline{u_1^T}\right)$ relaxation coefficient β_5 needs to be determinated in order to provide an appropriate amount of damping. Rudy and Strickwerda [113] derived the following one dimensional system of Euler equations:

$$\begin{pmatrix} \frac{\partial \widetilde{u}}{\partial t} \\ \frac{\partial \widetilde{p}}{\partial t} \end{pmatrix} + \begin{bmatrix} \overline{u_1} & \overline{\rho}^{-1} \\ \gamma\overline{p} & \overline{u} \end{bmatrix} \begin{pmatrix} \frac{\partial \widetilde{u_1}}{\partial x_1} \\ \frac{\partial \widetilde{u_1}}{\partial x_1} \end{pmatrix} = \begin{pmatrix} 0 \\ 0 \end{pmatrix} \tag{B.3}$$

The variables are perturbations $\widetilde{u_1}$ and $\widetilde{p}$. Considering a 1D flow with non-reflecting inlet condition at $x_1 = 0$ and fixed pressure at $x_1 = L$ the boundary

conditions for the above problem are:

$$\frac{\partial \widetilde{p}}{\partial t} + \overline{\rho c}\frac{\widetilde{u_1}}{\partial t} + \beta_5 \widetilde{u}_1 = 0 \quad \text{at} \quad x = 0$$
$$\widetilde{p}(x,t) = 0 \text{ at} \quad x = L$$

(B.4)

A solution to this problem with the highest value of β_5, appropriate for a non-reflecting inlet able to quickly relax u_1 towards u_1^T, has been found by Rudy and Strickwerda with the final result:

$$\beta_{5opt} = 0.278\overline{\rho}\frac{\overline{c}^2 - \overline{u_1}^2}{L}$$

(B.5)

The resulting entering acoustic wave $\mathcal{L}_5$ is determined:

$$\mathcal{L}_5 = (u_1 + c)\left(\frac{\partial p}{\partial x_1} + \rho c\frac{\partial u_1}{\partial x_1}\right) = \eta_{5opt}\overline{\rho}\frac{\overline{c}^2 - \overline{u_1}^2}{2L}\left(u_1 - \overline{u_1^T}\right)$$

(B.6)

Where $\eta_{5opt} = 0.278$; the relaxation coefficient adopted in our implementation is in the form $\sigma_{u1} = (u_1 - u_1^T)$. Thus

$$\sigma_{u1} = 0.278\rho c^2\frac{1 - Ma^2}{2L}$$

(B.7)

B.2 Non-reflecting inlet condition for temperature

Similarly to the procedure adopted in Sec. B.1 to find an optimum for σ_p, Yoo et al. [140] suggest a theoretical approach to find the best value for the relaxation coefficient σ_T to model a non-reflecting inlet. They derive an expression for $\mathcal{L}_2$ resulting from a fixed temperature inlet boundary condition. So a linearized 1D energy equation is written:

$$\frac{\partial}{\partial t}\left(\frac{\widetilde{p}}{\rho^\gamma}\right) + \widetilde{u}_1\frac{\partial}{\partial x_1}\left(\frac{p}{\rho^\gamma}\right) = 0$$

(B.8)

leading to the boundary condition for the perturbed pressure and temperature:

$$\frac{\partial}{\partial t}\left(\frac{p}{\rho^\gamma}\right) + \widetilde{u}_1\beta_2\widetilde{T} = 0 \quad \text{at} \quad x = 0$$

(B.9)

Assuming the flow is an ideal gas temperature perturbation can be expressed:

$$\widetilde{T} = e^{-z(t-g(x))} \tag{B.10}$$

with $g(x)$ an arbitrary funciton of x. z has the dimension of the inverse of time and is assumed proportional to c/L so that:

$$\beta_2 = \frac{R}{\rho^{\gamma-1}}z \equiv -\eta_2\frac{R}{\rho^{\gamma-1}}\frac{c}{L}z \tag{B.11}$$

Substituting Eq. B.10 and B.14 into B.8 an expression for $\mathcal{L}_2$ is obtained:

$$\mathcal{L}_2 = u_1\left(c^2\frac{\partial\rho}{\partial x_1} - \frac{\partial p}{\partial x_1}\right) = \frac{p^\gamma}{c^2}\frac{\partial}{\partial t}\left(\frac{p}{\rho^\gamma}\right) = \eta_2\frac{\rho R}{cL}\left(T - T^T\right) \tag{B.12}$$

β_2 is proportional to z and hence no optimum value for η_2 can be found. The same Yoo [140] suggests $\eta_2 = -\eta_5$. This choice is adopted in this thesis too.

B.3 Non-reflecting inlet condition for generic transported scalar

Using the same arguments of Sec. B.2 time dependent boundary condition for a generic scalar variable may be written in the linearized form:

$$\frac{\partial}{\partial t}\left(\frac{\widetilde{f}_k}{\rho^\gamma}\right) + \beta_k\widetilde{f}_k = 0 \quad \text{at} \quad x = 0 \tag{B.13}$$

The solution has the form $\widetilde{f}_k = e^{-z(t-h_k(x))}$, substituting into Eq.B.13 and assuming z again proportional to inverse of acoustic time it is found:

$$\beta_k = z \equiv \eta_k\frac{c}{L} \tag{B.14}$$

Thus the corresponding wave amplitude time variation can be found as:

$$\mathcal{L}_k = \eta_k\frac{c}{L}\left(f - f^T\right) \tag{B.15}$$

Again Eq. B.14 shows no optimal value for η_k can be found. In this thesis $\eta_k = \eta_5$ is adopted.

Appendix C

Pseudoinverse

As is well known, the inverse of a matrix can be defined only when the matrix is square and non-singular (i.e. its determinant is different from zero). However, the inverse operation can be extended to the case of full rank non-square matrices by means of the *pseudoinverse.*

Let us consider a generic $m \times n$ matrix $\mathbf{A}$ whose entries are complex numbers. In general, the pseudoinverse $\mathbf{A}^\dagger$ of a $m \times n$ matrix $\mathbf{A}$ with complex entries is the unique $n \times m$ matrix that satisfies all the following properties [104]:

1. $\mathbf{A}\mathbf{A}^\dagger\mathbf{A} = \mathbf{A}$

2. $\mathbf{A}^\dagger\mathbf{A}\mathbf{A}^\dagger = \mathbf{A}^\dagger$

3. $(\mathbf{A}\mathbf{A}^\dagger)^H = \mathbf{A}\mathbf{A}^\dagger$

4. $(\mathbf{A}^\dagger\mathbf{A})^H = \mathbf{A}^\dagger\mathbf{A}$

where $\mathbf{A}^H$ is the *Hermitian transpose* of $\mathbf{A}$. $\mathbf{A}^H$ is obtained from $\mathbf{A}$ by taking the transpose and then the complex conjugate of each entry; in a mathematical form, the generic element A_{ij}^H of the Hermitian transpose is defined by (the symbol $*$ denotes the complex conjugate number):

$$A_{ij}^H = A_{ji}^* \qquad 1 \le i \le n, \quad 1 \le j \le m \tag{C.1}$$

It must be noted that, when all the matrix elements are real numbers, the Hermitian transpose is equal to the classical transpose matrix $\mathbf{A}^T$.

If $\mathbf{A}$ is a full rank matrix and $m > n$, the pseudoinverse can be explicitly computed as:

$$\mathbf{A}^\dagger = (\mathbf{A}^H \mathbf{A})^{-1} \mathbf{A}^H \tag{C.2}$$

which is clearly a *left inverse* of $\mathbf{A}$, in fact:

$$\mathbf{A}^\dagger \mathbf{A} = (\mathbf{A}^H \mathbf{A})^{-1} \mathbf{A}^H \mathbf{A} = I^{n \times n}$$

On the other hand, if $\mathbf{A}$ is a full rank matrix and $m < n$, the pseudoinverse is given by:

$$\mathbf{A}^\dagger = \mathbf{A}^H (\mathbf{A} \mathbf{A}^H)^{-1} \tag{C.3}$$

In this case, the pseudoinverse represents a *right inverse* of $\mathbf{A}$:

$$\mathbf{A} \mathbf{A}^\dagger = \mathbf{A} \mathbf{A}^H (\mathbf{A} \mathbf{A}^H)^{-1} = I^{m \times m}$$

The pseudoinverse is very useful for solving a linear system $\mathbf{y} = \mathbf{A}\mathbf{x}$ with $\mathbf{A}$ a full rank matrix. If $\mathbf{A}$ has more columns than rows ($m < n$) the system is said to be *under-determined* and the solution is not unique; it can be shown that the expression[1]:

$$\mathbf{x} = \mathbf{A}^\dagger \mathbf{y} = \mathbf{A}^H (\mathbf{A} \mathbf{A}^H)^{-1} \mathbf{y}$$

gives the solution that has the smallest Euclidean norm.

In the case of an *over-determined* system (the number of equations is greater

---

[1]Since $m < n$ the pseudoinverse is given by equation C.3.

than the number of unknowns, i.e. $m > n$), an approximate solution is given by[2]:

$$\mathbf{x} = \mathbf{A}^\dagger \mathbf{y} = (\mathbf{A}^H \mathbf{A})^{-1} \mathbf{A}^H \mathbf{y}$$

It can be shown that this is the solution that minimizes the Euclidean norm $\|\mathbf{y} - \mathbf{A}\mathbf{x}\|$ that is, the *least squares* solution.

---

[2]Since $m > n$ definition C.2 is applied.

Appendix D

Proper Orthogonal Decomposition

The Proper Orthogonal Decomposition (POD) post processing technique can be viewed as a numerical technique to perform modal analysis of any kind of transient data without assuming any spatial eigenmode shape. Reviewed for the analysis of turbulent flows in [26] and applied to measurements of naturally and acoustically excited jets in [114, 132], it permits the isolation of the flow coherent structures reproduced in the simulation. Such a technique projects the instantaneous solution $q_i(x)$ onto a time independent set of orthonormal basis functions $\phi^k(x)$, chosen as optimal in terms of projection error minimization. Temporal coefficients a_t^k describe the relative influence of the different spatial modes at the various times at which solution is recorded. Once decomposed, the unsteady flow field can be reconstructed using Eq. D.1.

$$q_i(x) = \sum_{k=1}^{N_m} a_i^k \cdot \phi^k(x) \tag{D.1}$$

To reduce the computational costs of the procedure, the snapshot method [122] was selected to construct the basis functions and the temporal coefficients. From a given number of snapshots, the temporal coefficients are calculated as the eigenvectors of the correlation matrix C which is an $N_s \times N_s$

tensor constructed using a scalar product between the solution snapshots:

$$C_{ij} = q_i(x) \cdot q_j(x). \tag{D.2}$$

The basis functions can be finally computed as:

$$\phi^k(x) = \sum_{i=1}^{N_s} b_i^k \cdot q_i(x). \tag{D.3}$$

where the matrix b is the inverse of the time coefficient matrix a.

This technique can be applied to any flow variable, e.g. pressure, temperature or velocity, by just redefining the scalar product in Eq. D.2 to compute the correlation matrix.

Modes are usually arranged with decreasing corresponding eigenvalue, which represents the "energy" content of each mode. The type of energy associated with each mode depends on the scalar product definition in Eq. D.2.

Bibliography

[1] European Research Community On Flow Turbulence And Combustion (ERCOFTAC) Classic Collection Database. http://cfd.mace.manchester.ac.uk/ercoftac/. Case: C 25.

[2] http://openflower.sourceforge.net/index2.html.

[3] http://openfvm.sourceforge.net/.

[4] *Computer Graphics: Principle and Practice*. Addison-Wesley Publishing Company, 1987.

[5] S. Acharya. Steady and unsteady RANS film cooling predictions. In *Film Cooling Science and Technology for Gas Turbine: State-of-the-Art Experimental and Computational Knowledge*, number 06 in Von Karman Lecture Series. 2007.

[6] S. Acharya and M. Tyagi. Direct numerical simulation (DNS) and large eddy simulation (LES) for film cooling. In *Film Cooling Science and Technology for Gas Turbine: State-of-the-Art Experimental and Computational Knowledge*, number 06 in Von Karman Lecture Series. 2007.

[7] P. Adami, F. Montomoli, S. Della Gatta, and F. Martelli. Conjugate heat transfer modelling in film cooled blades. *Proceedings of ASME Turbo Expo 2004: Power for Land, Sea and Air*, (GT2004-53177), 2004.

[8] A. Andreini, C. Bianchini, A. Ceccherini, B. Facchini, and L. Mangani. Investigation of circular and shaped effusion cooling arrays for combustor liner application - Part 2: Numerical analysis. *Proceedings of ASME Turbo Expo 2009: Power for Land, Sea and Air*, (GT2009-60038), 2009.

[9] A. Andreini, A. Bonini, G. Caciolli, B. Facchini, and S. Taddei. Numerical study of aerodynamic losses of effusion cooling holes in aero-engine combustor liners. *Proceedings of ASME Turbo Expo 2010: Power for Land, Sea and Air*, (GT2010-22942), 2010.

[10] A. Andreini, A. Ceccherini, B. Facchini, and D. Coutandin. Combined effect of slot injection, effusion array and dilution hole on the heat transfer coefficient of a real combustor liner part 2: Numerical analysis. *Proceedings of ASME Turbo Expo 2010: Power for Land, Sea and Air*, (GT2010-22937), 2010.

[11] A. Andreini, J.L. Champion, B. Facchini, E. Mercier, and M. Surace. Advanced liner cooling numerical analysis for low emission combustors. *ICAS*, 2006.

[12] A. Andreini, E. Di Carmine, B. Facchini, and M. Surace. Combustor liner cooling: numerical analysis of impingement geometries. *EUROTHERM 82 Numerical Heat Transfer 2005*, September 13-16 2005.

[13] A. Andreini and L. Mangani. Application of a new object-oriented CFD code to heat transfer analysis. *Proceedings of ASME Turbo Expo 2008: Power for Land, Sea and Air*, (GT2008-51118), 2008.

[14] F. Archambeau, N. Mechitoua, and M. Sakiz. Code Saturne: a Finite Volume Code for the computation of turbulent incom-

pressible flows - industrial applications. *International Journal on Finite Volumes*, 1, 2004. http://research.edf.com/research-and-the-scientific-community/softwares/code-saturne/introduction-code-saturne-80058.html.

[15] A. Bacci. *Development of a Turbulence Model for the Numerical Simulation of Film and Effusion Cooling in Gas Turbine Cooling.* PhD thesis, Energy Engineering Department, Università degli Studi di Firenze, 2006.

[16] A. Bacci and B. Facchini. Turbulence modeling for the numerical simulation of film and effusion cooling flows. *Proceedings of ASME Turbo Expo 2007: Power for Land, Sea and Air*, (GT2007-27182), 2007.

[17] J.C. Bailey, J. Intile, T.F Fric, A.K. Tolpaldi, N.V. Nirmalan, and R.S. Bunker. Experimental and numerical study of heat transfer in a gas turbine combustor liner. *Journal of Engineering for Gas Turbines and Power*, 125:994–1002, 2003.

[18] J. W. Baughn, A. Hechanova, and X. Yan. An experimental study of entrainment effects on the heat transfer from a flat surface to a heated circular impinging jet. *ASME Journal of Heat Transfer*, 113:1023–1025, 1991.

[19] J. W. Baughn and S. Shimizu. Heat transfer measurement from a surface with uniform heat flux and an impinging jet. *ASME Journal of Heat Transfer*, 111:1096–1098, 1989.

[20] M. Baum, T. Poinsot, and D. Thévenin. Accurate boundary conditions for multicomponent reactive flows. *Journal of Computational Physics*, 116:247–261, 1995.

[21] M. Behnia, S. Parneix, and P. A. Durbin. Prediction of heat transfer in an axisymmetric turbulent jet impinging on a flat plate. *International Journal of Heat and Mass Transfer*, 41:1845–1855, 1998.

[22] M. Behnia, S. Parneix, Y. Shabany, and P. A. Durbin. Numerical study of turbulent heat transfer in confined and unconfined impinging jets. *Journal of Heat and Fluid Flow*, 20:1–9, 1999.

[23] T. Behrendt and C. Hassa. A test rig for investigations of gas turbine combustor cooling concepts under realistic operating conditions. *Journal of Aerospace Engineering*, (222):169–177, 2008.

[24] V. Bellucci, C. O. Paschereit, and P. Flohr. Numerical and experimental study of acoustic damping generated by perforated screens. *AIAA Journal*, 42(8):1543–1549, 2004.

[25] G. Bergeles, A. D. Gosman, and B. E. Launder. The turbulent jet in a cross stream at low injection rates: a three-dimensional numerical treatment. *Numerical Heat Transfer*, 1:217–242, 1978.

[26] G. Berkooz, P. Holmes, and L. J. Lumley. The proper orthogonal decomposition in the analysis of turbulent flows. *Annual Review of Fluid Mechanics*, 25:539–575, 1993.

[27] C. Bianchini. Implementation and validation of RANS turbulence models for heat transfer analysis in an object oriented CFD code. Master thesis, Energy Engineering Department, Università degli Studi di Firenze, 2007.

[28] C. Bianchini, B. Facchini, and L. Mangani. Conjugate heat transfer analysis of an internally cooled turbine blade with an object oriented CFD code. *European Turbomachinery Conference*, 2009.

[29] C. Bianchini, B. Facchini, L. Mangani, and M. Maritano. Heat transfer performances of fan-shaped film cooling holes. Part II - numerical analysis. *Proceedings of ASME Turbo Expo 2010: Power for Land, Sea and Air*, (GT2010-22809), 2010.

[30] C. Bianchini, B. Facchini, F. Simonetti, L. Tarchi, and S. Zecchi. Numerical and experimental investigation of turning flow effects on innovative pin fin arrangements for trailing edge cooling configurations. *Proceedings of ASME Turbo Expo 2010: Power for Land, Sea and Air*, (GT2010-23536), 2010.

[31] C. Bianchini and L. Mangani. OpenFOAM for heat transfer analysis in turbomachinery. *OpenFOAM International Conference*, 2007.

[32] D. Bohn, V.J. Becker, and J.T. Kortmann. Numerical conjugate flow and heat transfer investigation of a transonic convection cooled turbine guide vane with different thermal barrier coatings. *IGTC Kobe*, (TS-77), 1999.

[33] D. Bohn and R. Krewinkel. Conjugate calculation of effusion cooling with realistic cooling hole geometries. *Proceedings of ASME Turbo Expo 2009: Power for Land, Sea and Air*, (GT2009-48845), 2009.

[34] G. Boudier, L. Y. M. Gicquel, and T. Poinsot. Comparison of LES, RANS and experiments in an aeronautical gas turbine combustion chamber. *Proceeding of the Combustion Institute*, 31, 2007.

[35] B. Boust, G. Lalizel, C. Bianchini, A. Ceccherini, G. Cinque, and S. Colantuoni. Dual investigations on the improvement of effusion cooling by shaped holes. *7th World Conference on Experimental Heat Transfer, Fluid Mechanics and Thermodynamics*, 2009.

[36] R. S. Bunker. Gas turbine heat transfer: Ten remaining hot gas path challenges. *Journal of Turbomachinery*, 129:193–201, 2006.

[37] C. Carcasci, B. Facchini, and F. Grillo. Development of diagnostic tools for real time assessment of gas turbine hot gas path component temperatures: A preliminary study. *Proceedings of ASME Turbo Expo 2002: Power for Land, Sea and Air*, (GT2002-30249), 2002.

[38] A. Ceccherini. *Design of Innovative Cooling Systems for Aero-Engine Combustion Chambers*. PhD thesis, Energy Engineering Department, Università degli Studi di Firenze, 2009.

[39] A. Ceccherini, B. Facchini, L. Tarchi, L. Toni, and D. Coutandin. Combined effect of slot injection, effusion array and dilution hole on the cooling performance of a real combustor liner. *Proceedings of ASME Turbo Expo 2009: Power for Land, Sea and Air*, (GT2009-60047), 2009.

[40] Y. M. Chung, K. H. Luo, and N. D. Sandham. Numerical study of momentum and heat transfer in unsteady impinging jets. *International Journal of Heat and Fluid Flow*, 23:592–600, 2002.

[41] F. Coletti and T. Arts. Experimental study of conjugate heat transfer in a rib-roughened trailing edge cooling channel with crossing-jets. In *Internal cooling in turbomachinery*, number 05 in Von Karman Lecture Series. 2010.

[42] D. Cooper, D. C. Jackson, B. E. Launder, and G. X. Liao. Impinging jet studies for turbulence model assessment. Part I: Flow-field experiments. *International Journal of Heat and Mass Transfer*, 36:2675–2684, 1993.

[43] T. Cziesla, E. Tandogan, and N. K. Mitra. Large Eddy Simulation of heat transfer from impinging slot jets. *Numerical Heat Transfer*, 32:1–17, 1997.

[44] J. Dassé, S. Mendez, and F. Nicoud. Large-Eddy Simulation of the Acoustic Response of a Perforated Plate. *Proceedings of the 14th AIAA/CEAS Aeroacoustic Conference, AIAA Paper*, (2008-3007), 2008.

[45] E. de Villiers. *The Potential of Large Eddy Simulation for the Modelling of Wall Bounded Flows*. PhD thesis, Thermofluids Section - Department of Mechanical Engineering, Imperial College of Science, Technology and Medicine, London, 2006.

[46] P. Dutt. Stable boundary conditions and difference schemes for Navier-Stokes equations. *Journal of Numerical Analysis*, 25:245–267, 1988.

[47] C. Eichler, A. Jeromin, B. Noll, and M. Aigner. Full 3-dimensional conjugate heat transfer simulation and heat transfer coefficient prediction for the effusion-cooled wall of a gas turbine combustor. *Proceedings of ASME Turbo Expo 2008: Power for Land, Sea and Air*, (GT2008-50422), 2008.

[48] J. D. Eldredge, D. J. Bodony, and M. Shoeybi. Numerical investigation of the acoustic behavior of a multi-perforated liner. *Proceedings of the 13th AIAA/CEAS Aeroacustic Conference*, (3683), 2007.

[49] E. I. Esposito. Jet impingement cooling configurations for gas turbine combustion. Master's thesis, Louisiana State University, 2006.

[50] B. Facchini, A. Magi, and A. Scotti Del Greco. Conjugate heat transfer simulation of a radially cooled gas turbine vane. *Proceedings of ASME Turbo Expo 2004: Power for Land, Sea and Air*, (GT2004-54213), 2004.

[51] B. Facchini, L. Tarchi, and L. Toni. A post processing procedure for the evaluation of adiabatic and overall effectiveness of effusion cooling geometries. *Proceedings of the 19th Symposium on Measuring Techniques in Turbomachinery, Rhode-St-Genãˆ©se*, 2008.

[52] B. Facchini, L. Tarchi, and L. Toni. Investigation of circular and shaped effusion cooling arrays for combustor liner application - Part 1: Experimental analysis. *Proceedings of ASME Turbo Expo 2009: Power for Land, Sea and Air*, (GT2009-60037), 2009.

[53] C. Fureby. On subgrid scale modeling in large eddy simulations of compressible fluid flow. *Physics of Fluids*, 8(5):1300–1311, 1996.

[54] M. Germano, U. Piomelli, P. Moin, and W. H. Cabot. A dynamic subgrid-scale eddy viscosity model. *Physics of Fluids A: Fluid Dynamics*, 3(7):1760–1765, 1991.

[55] A. Giusti. Assessment of computational methods for aeroacoustic analysis. Master thesis, Energy Engineering Department, Università degli Studi di Firenze, 2010.

[56] E. Gonfiotti. Large Eddy Simulation of combustion aeroacoustic instabilities. Master thesis, Energy Engineering Department, Università degli Studi di Firenze, 2009.

[57] K. M. B. Gustafsson and T. G. Johansson. An experimental study of surface temperature distribution on effusion cooled plates. *ASME Journal of Engineering for Gas Turbine and Power*, 123:308–316, 2001.

[58] M. Habte and S. Yavuzkurt. Effect of computational grid on performance of two-equation models of turbulence for film cooling applications. *Proceedings of ASME Turbo Expo 2008: Power for Land, Sea and Air*, (GT2008-50153), 2008.

[59] M. Hadziabdic. *LES, RANS and Combined Simulation of Impinging Flows and Heat Transfer*. PhD thesis, Department of Multi-scale Physics, Delft University of Technology, 2005.

[60] M. Hadziabdic and K. Hanjalic. LES of flow and heat transfer in a round impinging jet. *Direct and Large-Eddy Simulation, Springer*, VI:477–486, 2006.

[61] M. Hadziabdic and K. Hanjalic. Vortical structures and heat transfer in a round impinging jet. *Journal of Fluid Mechanics*, 596:221–260, 2008.

[62] T. Hallqvist. *Large Eddy Simulation of Impinging Jets with Heat Transfer*. PhD thesis, Department of Mechanics - Royal Institute of Technology, Stockholm, 2006.

[63] T. Hallqvist and L. Fuchs. Numerical study of swirling impinging jets with heat transfer. *ASME Heat Transfer/Fluids Engineering Summer Conference*, (HT-FED 04-56478), 2004.

[64] T. Hallqvist and L. Fuchs. Numerical study of swirling and non-swirling annular impinging jets with heat transfer. *Proceedings of 35th Fluid Dynamics Conference and Exhibit, AIAA paper*, (2005-5153), 2005.

[65] J. C. Han, S. Dutta, and S. Ekkad. *Gas Turbine Heat Transfer and Cooling Technology*. Taylor and Francis, 2000.

[66] N. Hardy. Norman Hardy's website. *http://www.cap-lore.com/MathPhys/IP/*.

[67] L. K. Harrison and D. G. Bogard. Comparison of RANS turbulence models for prediction of film cooling performance. *Proceedings of ASME Turbo Expo 2008: Power for Land, Sea and Air*, (GT2008-51423), 2008.

[68] J. S. Hassan and S. Yavuzkurt. Comparison of four different two equation models of turbulence in predicting film cooling performance. *Proceedings of ASME Turbo Expo 2006: Power for Land, Sea and Air*, (GT2006-90860), 2006.

[69] R. T. Hebert. Innovative cooling configurations for low emission gas turbine combustors. Master's thesis, Louisiana State University, 2004.

[70] A. Hoda and S. Acharya. Predictions of a film coolant jet in cross-flow with different turbulence models. *Journal of Turbomachinery*, 122(GT2006-90860):558–569, 2000.

[71] M. S. Howe. On the theory of unsteady high Reynolds number flow through a circular aperture. *Proceedings of the Royal Society A*, 366:205–223, 1979.

[72] F. Q. Hu. A stable, perfectly matched layer for linearized Euler equations in unsplit physical variables. *AIAA Journal*, 96:1664, 2001.

[73] F. Q. Hu, X. D. Li, and D. K. Lin. Absorbing boundary conditions for non linear Euler and Navier-Stokes equations based on the perfectly matched layer technique. *Journal of Computational Physics*, 227:4398–4424, 2008.

[74] Y. Huang and V. Yang. Dynamics and stability of lean-premixed swirl stabilized combustion. *Progress in energy and combustion science*, (35), 2009.

[75] U. Ingard and V. K. Singhal. Sound attenuation in turbulent pipe flow. *Journal of Acoustical Society of America*, 55:535–538, 1974.

[76] M. Israeli and S. A. Orszag. Approximation of radiation boundary conditions. *Journal of Computational Physics*, 41:115–135, 1981.

[77] R. I. Issa. Solution of the implicitly discretised fluid flow equations by operator splitting. *Journal of Computational Physics*, 62:40–65, 1986.

[78] K. Jambunathan, E. Lai, M. Moss, and B. Button. A review of heat transfer data for single circular jet impingement. *International Journal of Heat and Fluid Flow*, 13:106–115, 1992.

[79] S. H. Jang and J. G. Ih. On the multiple microphone method for measuring in-duct acoustic properties in the presence of mean flow. *Journal of Acoustical Society of America*, 103(3):1520–1526, 1998.

[80] N. D. Joshi, H. C. Mongia, G. Leonard, J. W. Stegmaier, and E. C. Vickers. Dry low emissions combustors development. *Proceedings of ASME Turbo Expo 1998: Power for Land, Sea and Air*, (GT1998-0310), 1998.

[81] N. Kornev, H. Kroger, J. Turnow, and E. Hassel. Synthesis of artificial turbulent fields with prescribed second-order statistics using the random-spot method. *Proceedings in Applied Mathematics and Mechanics*, 7, 2007.

[82] D. Lakehal, G. S. Theodoris, and W. Rodi. Three-dimensional flow and heat transfer calculations of film cooling at the leading edge of a symmetrical turbine blade model. *International Journal of Heat and Fluid Flow*, 22:113–122, 2001.

[83] G. A. Ledezma, G. M. Laskowski, and A. K. Tolpadi. Turbulence model assessment for conjugate heat transfer in a high pressure turbine vane model. *Proceedings of ASME Turbo Expo 2008: Power for Land, Sea and Air*, (GT2008-50498), 2008.

[84] D. H. Leedom and S. Acharya. Large Eddy Simulations of film cooling flow fields from cylindrical and shaped holes. *Proceedings of ASME Turbo Expo 2008: Power for Land, Sea and Air*, (GT2008-51009), 2008.

[85] A. H. Lefebvre. *Gas Turbine Combustion*. Taylor and Francis, 1998.

[86] A. H. Lefebvre and E. R. Norster. The influence of fuel preparation and operating conditions on flame radiation in a gas turbine combustor. *ASME paper*, (72-WA HT-26):463–473, 1972.

[87] N. Liu, K. Hanjalic, D. Borello, and Z. Tao. Large-Eddy Simulation of periodic discrete-hole effusion without and with rotation. *8th European Turbomachinery Conference*, 2009.

[88] G. Lodato, P. Domingo, and L. Vervisch. Three dimensional boundary conditions for direct and Large-Eddy Simulation of compressible viscous flows. *Journal of Computational Physics*, 227:5015–5143, 2008.

[89] M. M. Lohasz and P. Rambaud. Conjugate heat transfer: CFD. In *Internal cooling in turbomachinery*, number 05 in Von Karman Lecture Series. 2010.

[90] J. Luo and E.H. Razinsky. Conjugate heat transfer analysis of a cooled turbine vane using the V2F turbulence model. *Journal of Turbomachinery*, 129:773–781, 2007.

[91] V. J. Lyons. Fuel-air nonuniformity-effect on nitric oxide emissions. *AIAA paper*, (81-0327), 1981.

[92] D. Lytle and B. Webb. Air jet impingement heat transfer at low nozzle-plate spacings. *International Journal of Heat and Mass Transfer*, 37:1687–1697, 1994.

[93] L. Mangani, C. Bianchini, A. Andreini, and B. Facchini. Development and validation of a C++ object oriented CFD code for heat transfer analysis. *ASME Summer Heat Transfer*, (AJ-1266), 2007.

[94] S. Mendez and J. D. Eldredge. Acoustic modeling of perforated plates with bias flow for Large-Eddy Simulations. *Journal of Computational Physics*, 228:4757–4772, 2009.

[95] S. Mendez and F. Nicoud. Adiabatic homogeneous model for flow around a multi-perforated plate. *AIAA Journal*, 46(10):2623–2633, 2008.

[96] S. Mendez and F. Nicoud. Large-Eddy Simulation of a bi-periodic turbulent flow with effusion. *Journal of Fluid Mechanics*, 598:27–65, 2008.

[97] S. Menon, P.K. Yeung, and W. W. Kim. Effect of subgrid models on the computed interscale energy transfer in isotropic turbulence. *AIAA paper*, 94-2387, 1994.

[98] M. L. Munjal and A. G. Doige. The two-microphone method incorporating the effects of mean flow and acoustic damping. *Journal of Sound and Vibrations*, 137:135–138, 1990.

[99] K. Nishino, M. Samada, K. Kasuya, and K. Torii. Turbulence statistics in the stagnation region of an axisymmetric impinging jet flow. *International Journal of Heat and Fluid Flow*, 17:193–201, 1996.

[100] OpenCFD. http://www.openfoam.com/.

[101] M. Orlansky. A simple boundary condition for unbounded flows. *Journal of Computational Physics*, 21:251–269, 1976.

[102] S. V. Patankar. *Numerical Heat Transfer and Fluid Flow*. Taylor and Francis, USA, 1980.

[103] Y. V. Peet and S. K. Lele. Near field of film cooling jet issued into a flat plate boundary layer: LES study. *Proceedings of ASME Turbo Expo 2008: Power for Land, Sea and Air*, (GT2008-50420), 2008.

[104] R. Penrose. A generalized inverse for matrices. *Proceedings of the Cambridge Philosophical Society*, 51:406–413, 1955.

[105] U. Piomelli. Large Eddy Simulation of turbulent flows - Part 1: introduction. In *Large Eddy Simulation and related techniques theory and applications*, number 04 in Von Karman Lecture Series. 2008.

[106] T. Poinsot and D. Veynante. *Theoretical and numerical combustion*. R. T. Edwards, Inc., 2001.

[107] T. J. Poinsot and S. K. Lele. Boundary conditions for direct simulations of compressible viscous flows. *Journal of Computational Physics*, 101:104–129, 1992.

[108] P. Renze, W. Schroder, and M. Meinke. Large-eddy simulation of film cooling flow ejected in a shallow cavity. *Proceedings of ASME Turbo Expo 2008: Power for Land, Sea and Air*, (GT2008-50120), 2008.

[109] S. W. Rienstra and A. Hirschberg. *An Introduction to Acoustics*. Eindhoven University of Technology, 2009.

[110] W. Rodi. Experience with two-layer models combining the $k - \epsilon$ model with a one-equation model near wall. 29th *Aerospace Sciences Meeting, AIAA paper*, (91-0216), 1991.

[111] Integrated Lean Low-Emission Combustor Design Methodology INTELLECT D.M. Contract No. 502961.

[112] Knowledge for Ignition, Acoustic, and Instabilities kiai. Contract No. 211843.

[113] D. H. Rudy and J. C. Strikwerda. A non-reflecting outflow boundary condition for subsonic Navier Stokes calculations. *Journal of Computational Physics*, 36:55–70, 1980.

[114] J. Rupp, J. Carrotte, and A. Spencer. Methodology to identify the unsteady flow field associated with the loss of acoustic energy in the vicinity of circular holes. *Proceedings of ASME Turbo Expo 2010: Power for Land, Sea and Air*, (GT2010-22178), 2010.

[115] A. Schulz. Infrared thermography as applied to film cooling of gas turbine components. *Measurement Science and Technology*, 11:948–956, 2000.

[116] A. Schulz. Combustor liner cooling technology in scope of reduced pollutant formation and rising thermal efficiencies. *Heat transfer in Gas Turbine Systems*, 934:135–146, 2001.

[117] J. J. Scrittore, K. A. Thole, and S. W. Burd. Experimental characterization of film-cooling effectiveness near combustor dilution holes. *Proceedings of ASME Turbo Expo 2005: Power for Land, Sea and Air*, (GT2005-68704), 2005.

[118] L. Selle, F. Nicoud, and T. Poinsot. The actual impedance of non-reflecting boundary conditions: implications for the computation of resonators. *AIAA Journal*, 42(5):958–964, June 2004.

[119] F. F. Simon. Jet model for slot film cooling with effect of freestream and coolant turbulence. *NASA Technical Report*, 2655, 1986.

[120] F. Simonetti. *Numerical and Experimental Investigation on Multi-perforated Liners in Aeroengine Combustors*. PhD thesis, Energy Engineering Department, Università degli Studi di Firenze, 2011.

[121] F. Simonetti, A. Andreini, C. Bianchini, B. Facchini, and A. Peschiulli. Assessment of numerical tools for the evaluation of the acoustic impedance of multiperforated plates. *Proceedings of ASME Turbo Expo 2011: Power for Land, Sea and Air*, (GT2011-46303), 2011.

[122] L. Sirovich. Turbulence and the dynamic of coherent structures, Part I: Coherent structures. *Quarterly of Applied Mathematics*, 45:561–571, 1987.

[123] E. Sozer. http://www.freecfd.com/.

[124] J. C. Strikwerda. Initial value boundary problem for incompletely parabolic systems. *Communication on Pure Applied Mathematics*, 89:30, 1977.

[125] M. K. Sung and I. Mudawar. Single-phase and two-phase hybrid cooling schemes for high-heat-flux thermal management of defense electronics. *Thermal and Thermomechanical Phenomena in Electronic Systems*, pages 121–131, 2008.

[126] M. Surace. *Investigation of impingement systems for gas turbine combustor cooling*. PhD thesis, Energy Engineering Department, Università degli Studi di Firenze, 2005.

[127] J. C. Sutherland and C. A. Kennedy. Improved boundary conditions for viscous, reacting, compressible flows. *Journal of Computational Physics*, 191:502–524, 2003.

[128] G. R. Tabor and M. H. Baba-Ahmadi. Inlet conditions for Large Eddy Simulation: A review. *Computers and Fluids*, 39:553:567, 2010.

[129] G. R. Tabor, M. H. Baba-Ahmadi, E. de Villiers, and H. G. Weller. Construction of inlet conditions for LES of turbulent channel flow. *European Congress on Computational Methods in Applied Sciences and Engineering ECCOMAS 2004*, 21:251–269, 2004.

[130] K. W. Thompson. Time-dependent boundary conditions for hyperbolic systems. *Journal of Computational Physics*, 68:1–24, 1987.

[131] K. W. Thompson. Time-dependent boundary conditions for hyperbolic systems II. *Journal of Computational Physics*, 89:439–461, 1990.

[132] B. S. Thurow and K. P. Lynch. 3D POD analysis of a naturally excited jet. *Proceedings of 38th Fluid Dynamics Conference and Exhibit, AIAA paper*, (2008-4067), 2008.

[133] L. Toni. *Gas Turbine Aero-Engines Effusion Cooling Systems*. PhD thesis, Energy Engineering Department, Università degli Studi di Firenze, 2009.

[134] N. Uddin. *Turbulence Modeling of Complex Flows in CFD*. PhD thesis, Institute of Aerospace Thermodynamics, Universitat Stuttgart, 2008.

[135] N. Uddin, S. O. Neumann, and B. Weigand. Investigation of the effect of inlet velocity field excitation of turbulent impinging jet on heat transfer using large eddy simulation. *International Conference on Jets, Wakes and Separated Flows, ICJWSF-2008*, 2008.

[136] N. Uddin, S. O. Neumann, and B. Weigand. Large Eddy Simulation of the heat transfer due to swirling and non-swirling jet impingement. *Proceedings of 2008 ASME Summer Heat Transfer Conference*, (HT2008-56422), 2008.

[137] S. Wang, V. Yang, G. Hsiao, S. Y. Hsieh, and H. C. Mongia. Large-eddy simulations of gas-turbine swirl injector flow dynamics. *Journal of Fluid Mechanics*, 583:99–122, 2007.

[138] Q. Xue. Development of conjugate heat transfer capability to an unstructured flow solver - U2NCLE. Master's thesis, Mississipi State University, 2005.

[139] C. Yang, T. Kung, and C. Gau. Heat transfer process under a film-cooled surface with presence of weak swirling flow in the mainstream. *Experimental Thermal and Fluid Science*, 32(2):632–640, 2007.

[140] C. Yoo and H. Im. Characteristic boundary conditions for simulations of compressible reacting flows with multi-dimensional, viscous, and reaction effects. *Combustion Theory and Modeling*, 11:259–286, 2007.

[141] C. Yoo, Y. Wang, A. Trouve, and H. Im. Characteristic boundary conditions for direct simulations of turbulent counterflow flames. *Combustion Theory and Modeling*, 9:617–646, 2005.

[142] A. Yoshizawa. Bridging between eddy-viscosity-type and second-order models using a two-scale DIA. *Ninth Symposium on Turbulent Shear Flows*, 1993.